STRUCTURAL GEOLOGY AND GEOCHEMISTRY OF SEDIMENTARY ROCK-HOSTED GOLD IN THE EASTERN NADALEEN TREND, YUKON TERRITORY, CANADA

By

Justin C. Palmer

A thesis submitted to the Faculty and the Board of Trustees of the Colorado School of Mines in partial fulfillment of the requirements for the degree of Master of Science (Geology).

Golden, Colorado

Date ____________

Signed: ______________________________

Justin C. Palmer

Signed: ______________________________

Dr. Yvette D. Kuiper

Thesis Advisor

Golden, Colorado

Date ____________

Signed: ______________________________

Dr. Paul M. Santi

Department Head and Professor

Department of Geology and Geological Engineering

ABSTRACT

Recently discovered gold (Au) in the eastern Nadaleen Trend of northeastern Yukon Territory is hosted in unmetamorphosed Neoproterozoic carbonate and siliciclastic rocks that were subject to intense deformation prior to Au mineralization. Intense deformation in the region resulted from mid-Cretaceous NNE-vergent, thin-skinned fold-thrust deformation. Structures within a 6 km^2 area at the eastern Nadaleen Trend are complex and are not recognized elsewhere in northeastern Yukon Territory. Field observations suggest these rocks are the product of NNE-SSW-directed shortening (D_1), NW-SE-oriented dextral simple shear (D_2), and N-S-directed shortening (D_3) followed later by minor dextral slip (D_4). The complicated geometry of the area may result from the presence of basement structures and/or competency contrasts between rock units within the sedimentary package.

The eastern Nadaleen Trend lies within an E-trending triangle zone bounded by S- and N-vergent reverse faults to the north and south, respectively. The triangle zone does not continue to the west or east. To the west, rocks consist of multiple NNE-verging structures in the south and only one map-scale fold in the north indicating that strain decreases northwards. Rocks in the east are consistently NNE-vergent. This change in structural style suggests that NNE-directed transport in the rocks to the west was obstructed at the latitude of the eastern Nadaleen Trend while transport in the east was unobstructed. Potential causes for the obstruction include rheological heterogeneity or a subsurface structure. The obstruction is nearly co-spatial with the steep southward transition from both Neoproterozoic and Paleozoic platform rocks to basin rocks. This abrupt platform-to-basin transition occurred in this location throughout much of geologic history, suggesting that the location of the transition may be pinned by a pre-existing basement feature. For this reason, we suggest that mid-Cretaceous deformation patterns were influenced by a subsurface basement fault that obstructed NNE-directed fold-thrust movement to the west of the eastern Nadaleen Trend. The structure's interpreted eastern edge below the eastern Nadaleen Trend may have presented a minor obstruction that resulted in the formation of a triangle zone. East of the eastern Nadaleen Trend, fold-thrust related movement was unobstructed. Between unobstructed rocks in the east and obstructed rocks in the west, a strike-slip interface is interpreted to occur that may have influenced the orientation of oblique folds that occur within the eastern Nadaleen Trend.

Major Au deposits within the eastern Nadaleen Trend occur within moderately to steeply S- to SSW-plunging anticlines and not within folds in other orientations or synclines. The orientation of the folds that host Au is oblique to the regional trend and they occur within the E-trending triangle zone. Reverse faults bounding the triangle zone are interpreted to have acted as an aquitard below which ore fluid migrated updip. Within the eastern Nadaleen Trend, ore fluid migration was concentrated into hinge zones of SSW-plunging anticlines, which may have acted as local fluid conduits.

One of the Au zones, the Conrad zone, is situated in the northeast part of the eastern Nadaleen Trend and within a steeply SSW-plunging anticline that folds fine-grained siliciclastic rocks overlying silty limestone. This anticline is cutoff to the north by a ~50 m wide NNE-dipping fault zone. Deep within the Conrad zone, Au dominantly occurs within the anticline hinge zone, suggesting that ore fluid indeed may have risen along the fold hinge zone. Relatively more Au occurs at shallower levels, perhaps because the (now eroded) juxtaposed anticlinal fine-grained siliciclastic rocks and fault zone presented a natural trap that slowed upward fluid migration. If fluid upwelling was restrained in this zone, it could have prolonged the interaction time between ore fluid and the host rock that may have led to increased Au deposition.

Fluid-rock interaction within the Conrad Au zone changed equilibrium conditions in both the ore fluid and the host rock. The change in conditions destabilized certain components of both the host rock and the ore fluid that resulted in an elemental flux between the two. This flux is preserved within the host rock where certain elements show enrichments or depletions in the presence of Au. Within the Conrad zone, Ca, Mg, and Na are depleted in Au-bearing samples suggesting that the fluid that brought in Au also facilitated a loss of carbonate minerals. Elements enriched in Au-bearing samples include S, Au, As, Sb, Hg, Tl, Te, Cu, Pb, Zn, Bi, Ni, Fe, Ba, Li, and Cd suggesting that they were brought in with the ore fluid. Au-bearing samples have an S/Fe value near 1.15, suggesting an association exists between Au and pyrite (FeS_2; 46.7 wt. % Fe). The geochemical features above show strong geochemical similarities to Carlin-type deposits in Nevada, USA.

TABLE OF CONTENTS

LIST OF FIGURES

LIST OF TABLES

ACKNOWLEDGEMENTS

I owe the utmost appreciation and respect to my thesis advisor, Dr. Yvette Kuiper. None of this would have been possible without your constant encouragement, inspiration, patience, and advice throughout the ups and downs of this thesis. Your guidance has given me an excellent grasp of the scientific method and an ability to write scientifically and apply creative thinking to geologic problems. I truly appreciate your friendship throughout it all. To the other members of my committee, Dr. Thomas Monecke, Dr. Murray Hitzman, and Dr. Poul Emsbo, I extend paramount appreciation and respect. Your advice substantially improved the quality of both my education and this thesis. To the four people above: I can't thank you enough for supporting me through my education, and converting me into the geologist I am today.

The opportunity to conduct this research and achieve a master's degree would not have been possible without the outstanding financial support offered by ATAC Resources Ltd. To Rob Carne, Joan Carne, and Julia Lane I extend my utmost gratitude for your geologic advice and friendship during the ten weeks I spent at beautiful Nadaleen camp and for your help and encouragement ever since. The Society of Economic Geologists is thanked for their financial support through grants and fellowships and for their educational opportunities through the SEG student field trip and various short courses that greatly improved my education.

To Dr. Venessa Bennett: Thank you for your guidance during my first few days at Nadaleen camp and for getting Yvette and I in contact with ATAC Resources. To Dr. Odin Christensen: Thank you for your good humor and insight during our few days of field work.

I appreciate the following people for their help with ^{40}Ar/^{39}Ar geochronology of illite from faults within the Conrad zone and Sm-Nd geochronology on fluorite from the Osiris zone. To Dr. Alex Blum and Dr. Douglas McCarty: Thank you for your help with XRD and XRD modeling. To Dr. Chris Hall: Thank you for conducting ^{40}Ar/^{39}Ar geochronology. To Alan Koenig: Thank you for your excitement and lightheartedness during and after LA-ICP-MS analysis. To Dr. Lang Farmer and Emily Verplanck: Thank you for your help and ingenuity during Sm-Nd geochronology of my fluorite grains.

To the people who have been with me throughout this roller coaster ride I owe the greatest appreciation. To my friends here in Golden, specifically Eric VanHouten and Nick Kerr: Thanks for being a part of by far the most memorable, exciting, and adventurous experiences of my life. You both have made closing this chapter of my life and moving on to newer things substantially more difficult.

To my family: Your love and support throughout my life, our experiences together, and your influence on me have made me into the person who finishes this degree today. I thank and love every one of you.

I save the best for last. For her positive influence on the person I’ve become, for her constant encouragement of my adventurous dreams, and for her unwavering love, I thank the person who has had the most profound influence on my life; thank you for everything Alexandra Morales.

CHAPTER 1
INTRODUCTION

Recently discovered sedimentary rock-hosted gold (Au) in the Nadaleen Trend of northeastern Yukon Territory (Fig. 1.1) occurs in intensely deformed, unmetamorphosed, Neoproterozoic shelf to off-shelf carbonate and siliciclastic rocks (Fig. 1.2, 1.3; Colpron et al., 2013a; Moynihan et al., 2014). Four major Au zones (Anubis, Conrad, Isis East, Osiris/Sunrise) have been discovered over a 50 km strike length within the Nadaleen Trend, the westerly trend of which generally follows the trend of large regional faults (Fig. 1.2). Regional folds and faults primarily resulted from mid-Cretaceous NNE-vergent fold-thrust deformation (Murphy, 1997; Mair et al., 2006; Evenchick et al., 2007; Gehrels et al., 2009; Nelson et al., 2013); however, structures within the eastern Nadaleen Trend (the dominant study area; Fig. 1.3), including local S- to SSW-plunging anticlines that host Au (the Conrad, Isis East, and Osiris anticlines; Fig. 1.3), are oriented oblique to this dominant trend. Other structures within the 6 km^2 area include moderately to steeply WSW-, SE-, and E-plunging folds, W- and N-trending dextral strike-slip faults, and the NNE-dipping Nadaleen Fault zone (Fig. 1.3). A structural history behind the geometry of the eastern Nadaleen Trend has yet to be unraveled in the context of regionally recognized deformation events. Kuiper (2012) provided three potential structural histories for the local structures within the eastern Nadaleen Trend, but did not place these in a regional context. Colpron et al. (2013b) developed a regional deformation model that does not explain the local geology of the Nadaleen Trend.

A mineralogical and petrographic study conducted on the Conrad Au zone (Fig. 1.3) in the eastern Nadaleen Trend showed that Au occurs as very fine-grained disseminated particles primarily in carbonate rocks but also in siliciclastic rocks (Tucker et al., 2013). Alteration signatures consist dominantly of decalcification with subsequent silicification and brecciation (Tucker et al., 2013). Abundant, late-ore stage minerals including realgar, orpiment, illite, fluorite, and calcite fill pore spaces in rocks as a result of porosity increase during decalcification (Tucker et al., 2013). These features, as well as the structural and stratigraphic position of the

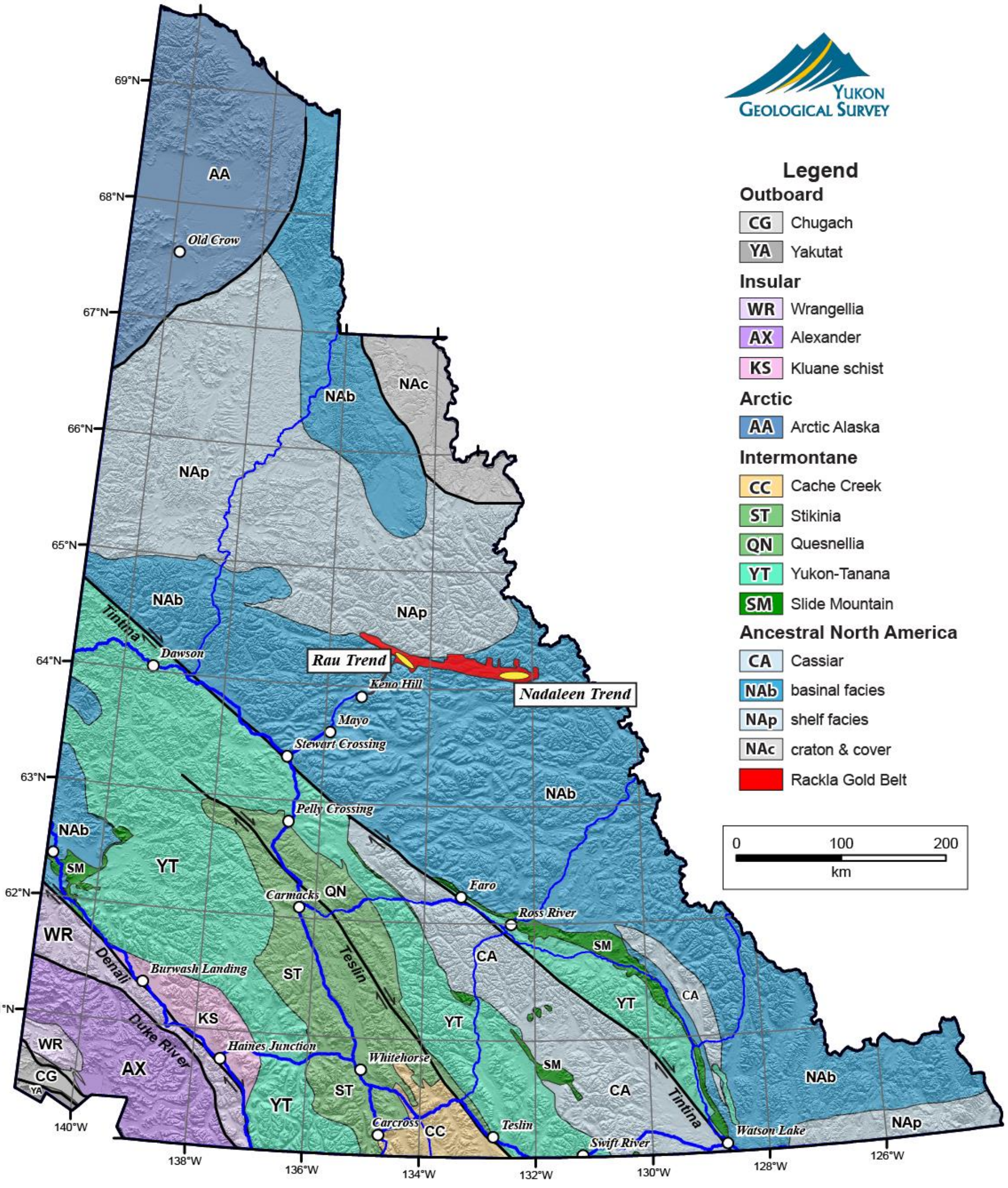

Figure 1.1: Geologic map of Yukon Territory. The Rackla Gold Belt, shown in red, is situated at the interface between the Mackenzie Platform (NAp) and the Selwyn Basin (NAb). The Rau and Nadaleen Trends are shown in yellow. Modified from Nelson et al. (2013).

Conrad zone within the region, led Tucker et al. (2013) to suggest that the Conrad zone is a Carlin-type deposit similar to other prolific sedimentary rock-hosted Au deposits that occur in Nevada, USA. Because Carlin-type deposits in Nevada collectively account for the second largest accumulation of Au known on Earth (Muntean et al., 2011), this distinction has important scientific and economic implications that warranted further research.

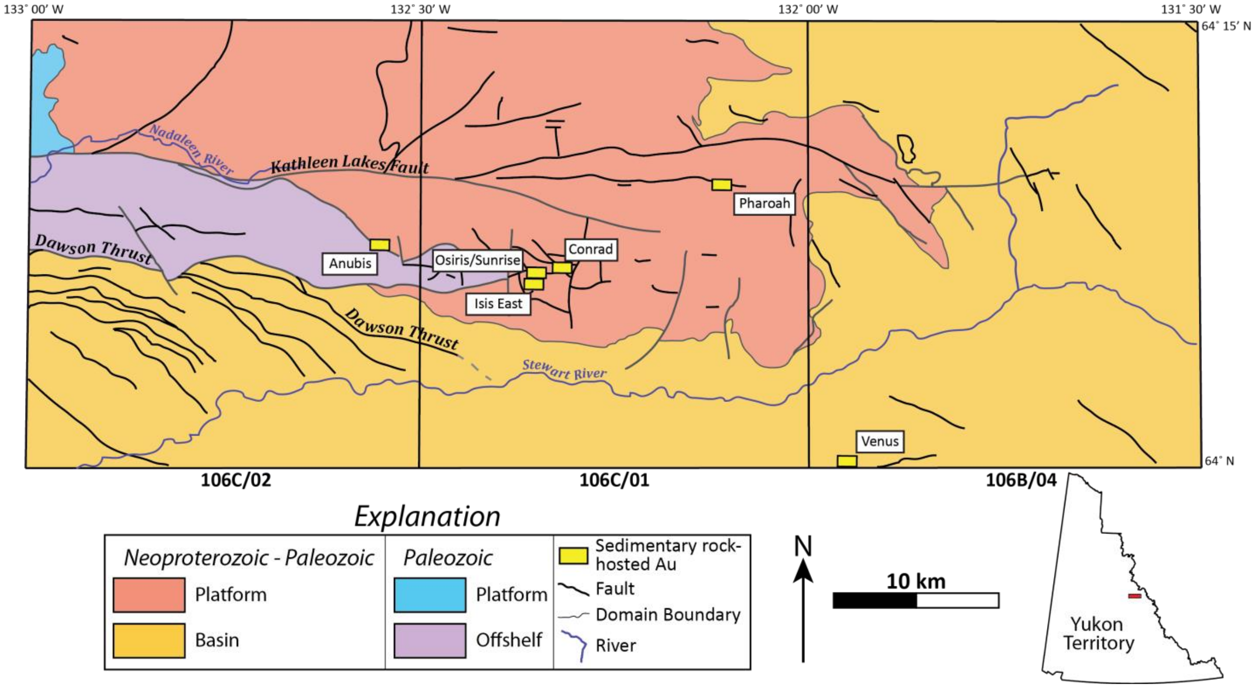

Figure 1.2: Summary geologic map of the region surrounding the Nadaleen Trend showing facies domains, major structures, and mineral occurrences. The Nadaleen Trend includes the Anubis, Conrad, Isis East, and Osiris/Sunrise zones. Modified after Colpron et al. (2013b).

The purpose of this study was to unravel the structural history responsible for the formation of (Au-controlling) structures in the eastern Nadaleen Trend in the context of the regional tectonic setting in order to understand the tectonic significance of the structures and evaluate their influence on later Au ore deposition and localization. In addition, geochemical characteristics of the Conrad zone were compared with those of Carlin-type deposits in Nevada to test for similarities that may suggest that the potential exists for another world-class endowment of Au within the Nadaleen Trend as it does in Nevada.

1.1 Thesis outline

This thesis is separated into four chapters. The first chapter (this chapter) provides a brief introduction of the problem and the purpose of the research. Chapter 2 is a manuscript to be submitted to *Mineralium Deposita*. It is focused on the local and regional deformation history, and the structural setting of the gold deposits. It includes a regional deformation model that has

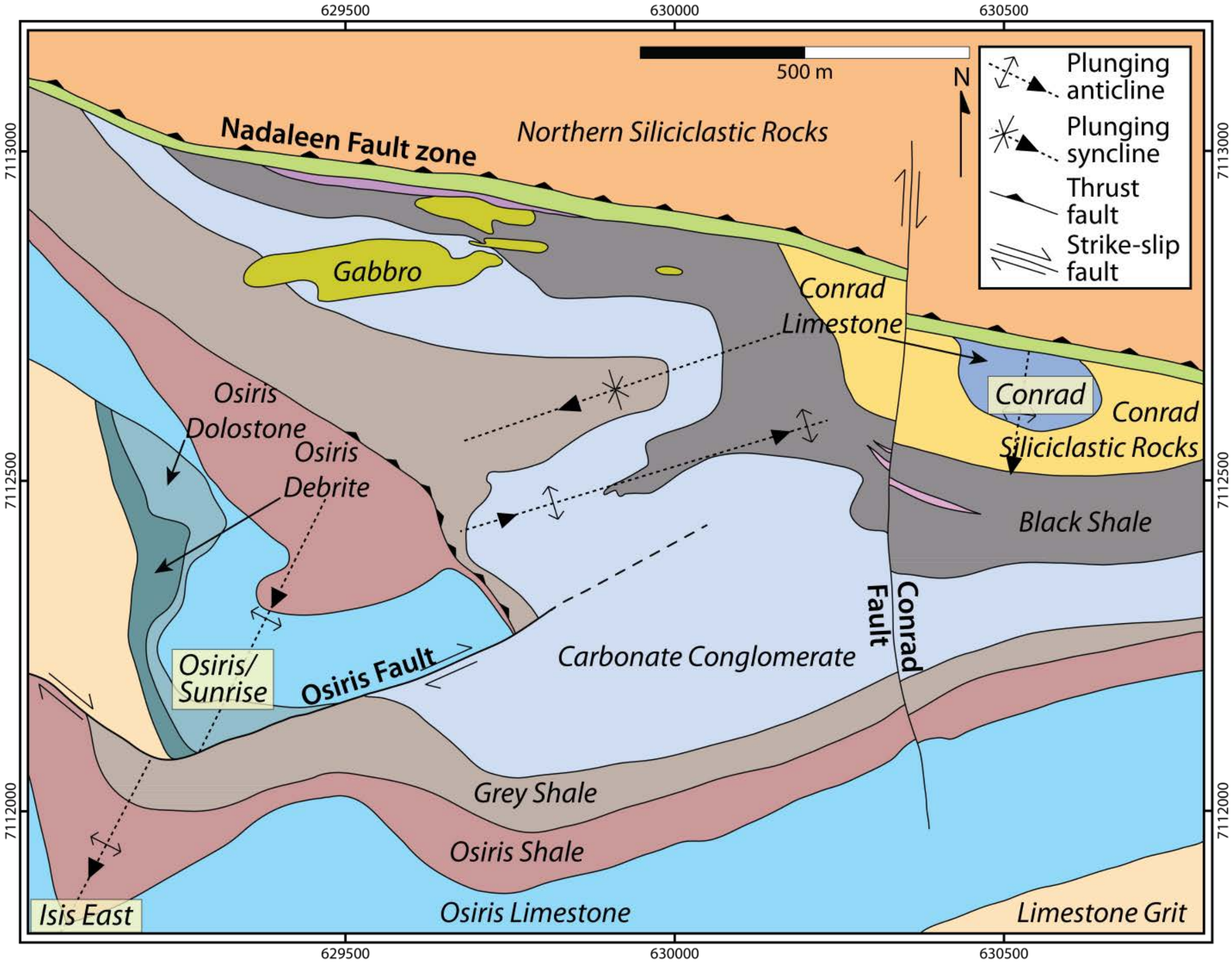

Figure 1.3: Geologic map of the eastern Nadaleen Trend. Au zones and names in yellow boxes, the names of faults are shown in bold, and descriptive rock names are italicized.

implications for the localization of Au within the eastern Nadaleen Trend. Chapter 3 presents the zone-scale geochemistry of the Conrad zone and emphasizes the relationship between Au and certain element enrichments and depletions as well as Au's relationship to pyrite that suggest similarities with Carlin-type deposits in Nevada. Chapter 4 provides an overview of the conclusions.

1.2 References

Colpron, M., Moynihan, D., Israel, S. and Abbott, G., 2013a, Geological map of the Rackla belt, east-central Yukon (NTS106C/1-4, 106D/1): Yukon Geological Survey, Open File 2013-13, 1:50,000 scale, 5 maps and legend.

Colpron, M., Moynihan, D., Israel, S., and Abbott, G., 2013b, Bedrock geology of the Rackla belt (106C/1-4 and 106D/1), southern Nadaleen map area, Yukon Geological Survey: Poster presented at 2013 AME BC Mineral Exploration Roundup Conference, Vancouver, BC, January 28-31, 2013.

Evenchick, C.A., McMechan, M.E., McNicoll, V.J. and Carr, S.D., 2007, A synthesis of the Jurassic-Cretaceous tectonic evolution of the central and southeastern Canadian Cordillera: Exploring links across the orogen: Geological Society of America, Special Paper 433, p. 117-145.

Gehrels, G., Rusmore, M., Woodsworth, G., Crawford, M., Andronicos, C., Hollister, L., Patchett, J., Ducea, M., Butler, R., Klepeis, K., Davidson, C., Friedman, R., Haggart, J., Mahoney, B., Crawford, W., Pearson, D. and Girardi, J., 2009, U-Th-Pb geochronology of the Coast Mountains batholith in north-coastal British Columbia: Constraints on age and tectonic evolution: Geological Society of America Bulletin, v. 121, p. 1341-1361.

Kuiper, Y.D., 2012, Structural setting of the Osiris, Isis and Isis East zones of the Rackla Gold Belt, east-central Yukon: Prepared for ATAC Resources, Internal Report, 17 p.

Mair, J.L., Hart, C.J.R. and Stephens, J.R., 2006, Deformation history of the northwestern Selwyn basin, Yukon, Canada: Implications for orogen evolution and mid-Cretaceous magmatism: Geological Society of America Bulletin, v. 118, p. 304-323.

Moynihan, D., Colpron, M., Israel, S. and Abbott, G, 2014, Geology of the eastern Rackla Belt, east-central Yukon: Poster presented at 2014 Mineral Exploration Roundup, January 27, 2014.

Muntean, J.L., Cline, J.S., Simon, A.C. and Longo, A.A., 2011, Magmatic-hydrothermal origin of Nevada's Carlin-type gold deposits: Nature Geoscience, v. 4, p. 122-127.

Murphy, D.C., 1997, Geology of the McQuesten River region, northern McQuesten and Mayo map areas, Yukon Territory: Yukon Geological Survey, Bulletin 6, 95 p.

Nelson, J.L., Colpron, M. and Israel, S., 2013, The cordillera of British Columbia, Yukon and Alaska: Tectonics and metallogeny, In: Colpron, M., Bissig, T., Rusk, B.G. and Thompson, J.F.H. (Eds.), Tectonics, metallogeny and discovery: The North American cordillera and similar accretionary settings: Society of Economic Geologists, Special Publication 17, p. 53-109.

Tucker, M.J., Hart, C.J.R. and Carne, R.C., 2013, Geology, alteration, and mineralization of the Carlin-type Conrad zone, Yukon, In: MacFarlane, K.E., Nordling, M.G. and Sack, P.J. (Eds.), Yukon Exploration and Geology 2012, Yukon Geological Survey, p. 163-178.

CHAPTER 2

STRUCTURAL GEOLOGY OF THE EASTERN NADALEEN TREND, YUKON TERRITORY, CANADA: IMPLICATIONS FOR RECENTLY DISCOVERED SEDIMENTARY ROCK-HOSTED GOLD

A paper to be submitted to *Mineralium Deposita*

Justin C. Palmer[1], Yvette D. Kuiper[1], Robert C. Carne[2]

2.1 Introduction

Sedimentary rock-hosted gold (Au) in ATAC Resources Ltd.'s (ATAC) recently discovered Nadaleen Trend occurs in intensely deformed, unmetamorphosed shelf to off-shelf carbonate and siliciclastic rocks that lie at the interface between the Neoproterozoic Mackenzie Platform and Selwyn Basin and at the eastern edges of the multi-hundred km-scale S-dipping Dawson Thrust and the Kathleen Lakes fault (Fig. 2.1) (Colpron et al., 2013a; Moynihan et al., 2014). The area is located in northeastern Yukon Territory 185 km ENE of Mayo, the nearest village, and at the eastern edge of the emerging Rackla Gold Belt (Figs. 2.1A, B). Four major Au zones (Anubis, Conrad, Isis East, and Osiris/Sunrise; Fig. 2.1C) were discovered within the trend between 2010 and 2013, and no official resource estimates have been disclosed for any of the zones at the time of writing; however, high-grade Au has been intersected in drill core (42.93 m of 18.44 g/t Au) and collected from surface trenches (www.atacresources.com).

The structural setting of the Au in the eastern Nadaleen Trend is complex and not fully understood. The trend is dominated by complex folds that are not recognized regionally. Au in the Osiris/Sunrise and Isis East zones is concentrated in the hinge zones of SSW-plunging anticlines (Kuiper, 2012; Tucker et al., 2013). Au in the Conrad zone has been interpreted as occurring within an E-trending, brittle-ductile shear zone, primarily based on a regional

---

[1] Department of Geology and Geological Engineering, Colorado School of Mines, Golden, CO
[2] ATAC Resources Limited, Vancouver, Canada

Figure 2.1: A. Map of western Canada. B. Generalized geologic map of northeastern Yukon Territory showing the outline of the Rackla Gold Belt and the Nadaleen Trend. C Regional map showing sediment hosted Au zones, reverse and normal faults and regional stratigraphic domains. Red box outlines the study area (D). Modified from Colpron et al. (2013a) and Moynihan et al. (2014). D. Geologic map of the eastern Nadaleen Trend showing local stratigraphy, structures, and Au discoveries. Colors as in Figure 2.2.

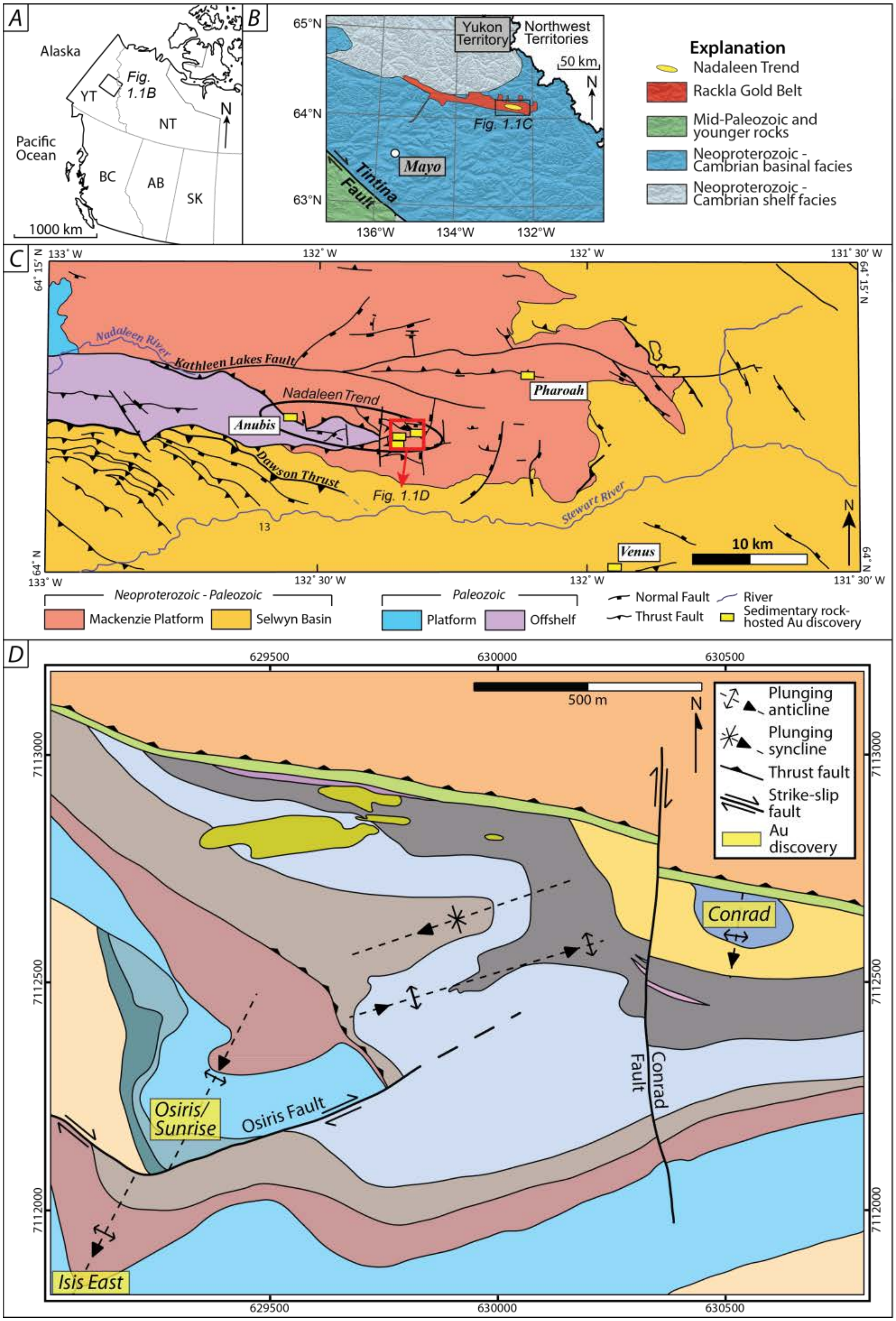
A
Alaska
Fig. 1.1B
YT
NT
Pacific Ocean
BC
AB
SK
N
1000 km
B
65°N
64°N
63°N
Yukon Territory
Northwest Territories
50 km
N
Fig. 1.1C
Mayo
Tintina Fault
136°W
134°W
132°W
Explanation
Nadaleen Trend
Rackla Gold Belt
Mid-Paleozoic and younger rocks
Neoproterozoic - Cambrian basinal facies
Neoproterozoic - Cambrian shelf facies
C
133° W
132° W
132° W
131° 30' W
64° 15' N
Nadaleen River
Kathleen Lakes Fault
Nadaleen Trend
Anubis
Pharoah
Dawson Thrust
Fig. 1.1D
Stewart River
13
Venus
10 km
N
64° N
133° W
132° 30' W
132° W
131° 30' W
Neoproterozoic - Paleozoic
Mackenzie Platform
Selwyn Basin
Paleozoic
Platform
Offshelf
Normal Fault
Thrust Fault
River
Sedimentary rock-hosted Au discovery
D
629500
630000
630500
500 m
N
Plunging anticline
Plunging syncline
Thrust fault
Strike-slip fault
Au discovery
7113000
7112500
7112000
Conrad
Conrad Fault
Osiris/Sunrise
Osiris Fault
Isis East
629500
630000
630500

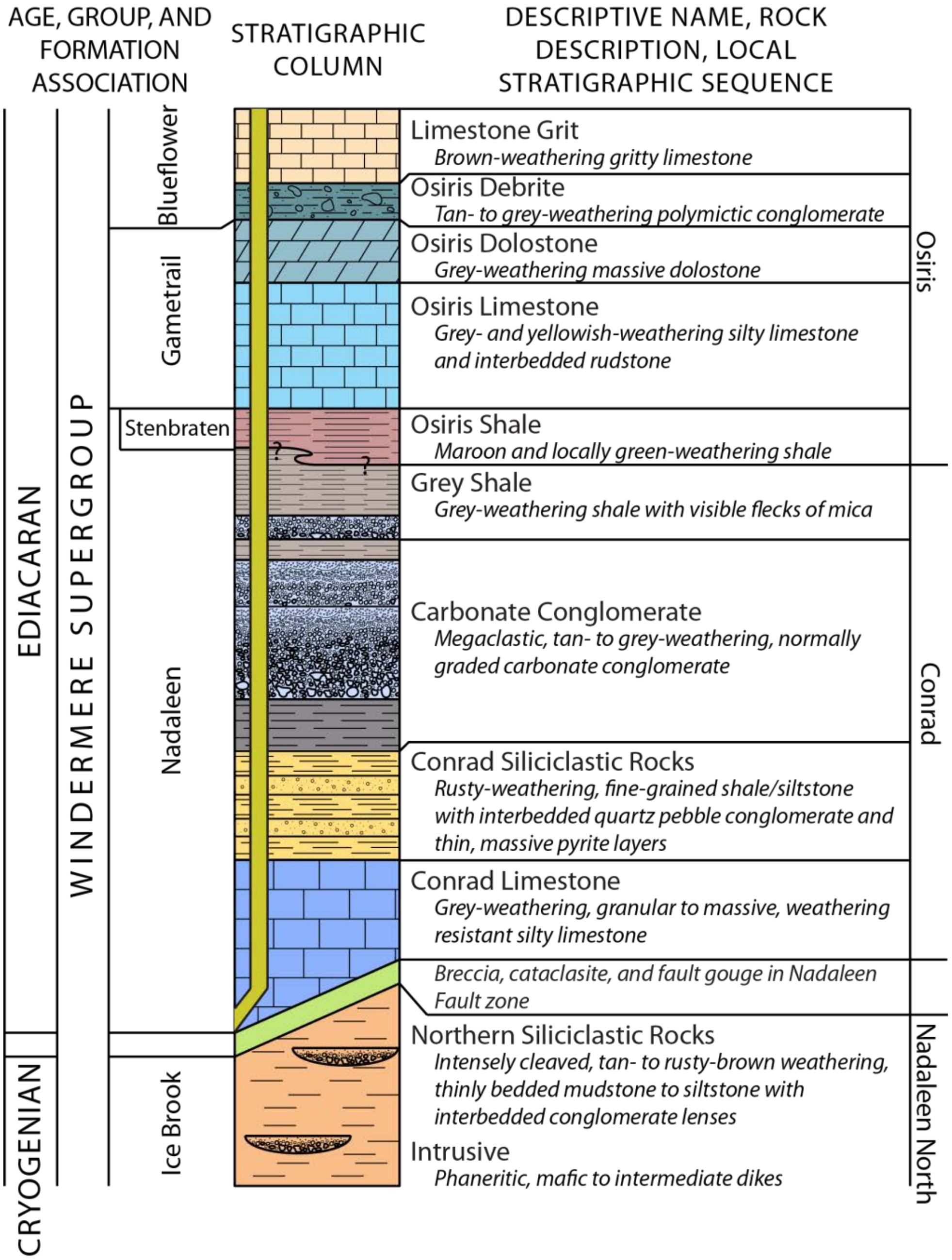

Figure 2.2: Eastern Nadaleen Trend stratigraphic column. Rock ages, group and formation associations are as interpreted by Colpron et al. (2013a) and Moynihan et al. (2014). Relative thicknesses as preserved today are indicated in the stratigraphic column. The green unit above the Northern siliciclastic rocks represents rocks of the Nadaleen Fault zone.

lineament analysis (Bennett, 2011), as well as within a WNW-trending doubly plunging anticline, based on the apparent subsurface geometry of the Conrad limestone as indicated in drill core (www.atacresources.com; Tucker et al., 2013).

Based on regional mapping, Colpron et al. (2013b) interpret the complexity of the eastern Nadaleen Trend as having resulted from the presence of an underlying W-trending basement high that separated two time-equivalent Neoproterozoic basins: the Nadaleen basin to the north and the Hyland basin to the south (Fig. 2.3). Extension and basinal sedimentation continued in the Hyland basin while platform sedimentation without further extension occurred above the Nadaleen basin (Fig. 2.3) (Colpron et al., 2013b). Later N-directed fold-thrust deformation reactivated early extensional structures in both the Hyland and Nadaleen basins in the mid-Cretaceous that ultimately resulted in reverse faults with opposing vergence across the eastern Nadaleen Trend, perhaps as a result of the basement high (Colpron et al., 2013b). While this model explains the structural geology along a north-trending section across the eastern Nadaleen Trend, it does not explain why oppositely verging reverse faults do not occur to the west or east of the eastern Nadaleen Trend nor does it explain the local structural complexities that occur within the eastern Nadaleen Trend.

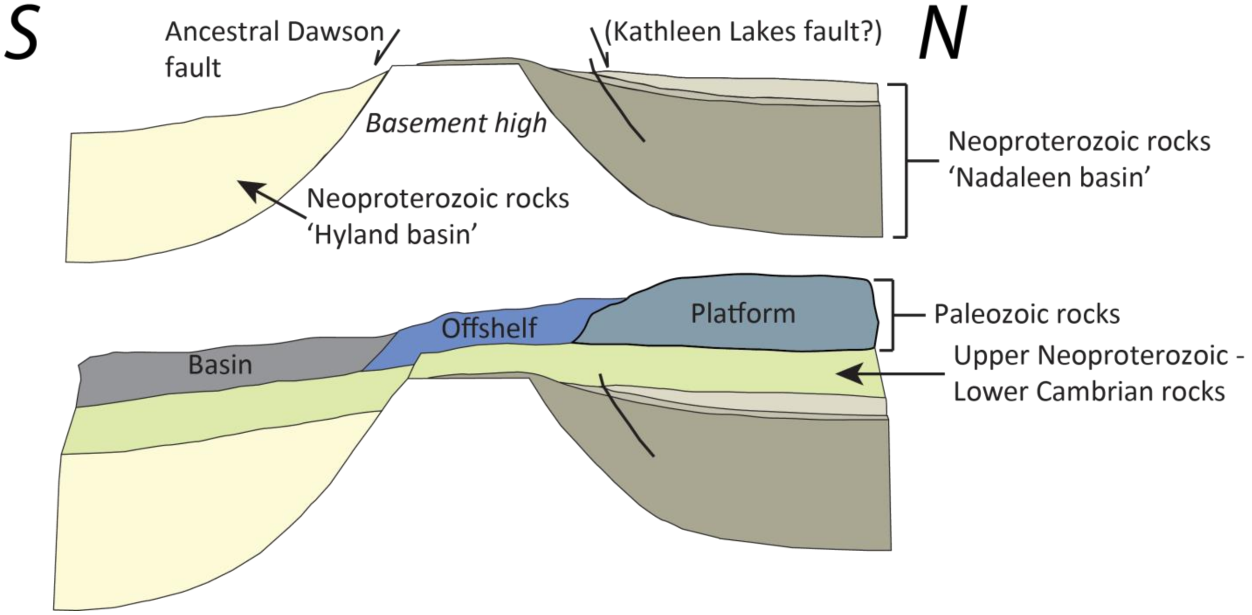

Figure 2.3: Interpretation of the late Neoproterozoic and Paleozoic basin architecture (Colpron et al., 2013b). The basement high and thicknesses of the rock packages are exaggerated. Modified from Colpron et al. (2013b).

The aim of this study was to reveal the structural setting of the better explored eastern Nadaleen Trend (Fig. 2.1C), using a multi-scale approach. We investigated the structural architecture of the Conrad zone through detailed surface mapping of the few existing, poorly exposed outcrops and by structural analysis of oriented drill core data. Surface structural mapping included the other Au zones within the eastern Nadaleen Trend in order to determine the structural history of the area and expose the structural setting of each Au zone. Finally, fold and fault trends from regional quadrangle maps (Colpron et al., 2013a; Moynihan et al., 2014) were analyzed in order to interpret our results in a regional context, and to investigate the potential controls of regional structures on Au mineralization.

2.2 Geological background

2.2.1 Stratigraphy

Rocks in the eastern Nadaleen Trend have been interpreted as part of the Windermere Supergroup and were deposited above Paleo- to Neoproterozoic basement (Colpron et al., 2013a; Moynihan et al., 2014). Rocks of the Windermere Supergroup are generally characterized by coarse, immature siliciclastic deposits and are interpreted to have been deposited during the first (723 – 716 Ma) of two rift phases that broke up the supercontinent Rodinia (Lund et al., 2003; Turner, 2011; MacDonald et al., 2010, 2012). Windermere Supergroup rocks occur only north of the Dawson Thrust (Fig. 2.1C), a long-lived fault that originated as a basin-bounding normal fault formed during the second phase of rifting (570 – 540 Ma) (Abbott, 1997; Colpron et al., 2002). This phase of rifting is interpreted to have opened the paleo-Pacific Ocean and initiated sedimentation in the Selwyn Basin and the Mackenzie Platform (Abbott, 1997; Colpron et al., 2002; Nelson et al., 2013). Rapid facies changes have been recognized in the Neoproterozoic strata west of the eastern Nadaleen Trend across the Dawson Thrust that suggest the fault is a long-lived structure that originated as a normal fault and controlled the abrupt Neoproterozoic transition from the Mackenzie Platform to Selwyn Basin on the western margin of North America (Abbott, 1997; Mair et al., 2006; Macdonald et al., 2012). A gentler platform-basin transition is interpreted east of the eastern Nadaleen Trend (Abbott, 1997; Norris, 1997). After the second phase of rifting, passive margin sedimentation and tectonic quiescence characterized the region through the mid-Mesozoic (Hansen, 1990; Creaser et al., 1999; Nelson et al., 2013).

Windermere Supergroup rocks observed within the eastern Nadaleen Trend have been divided into three distinct stratigraphic packages named Nadaleen North, Conrad, and Osiris.

The oldest rocks are siliciclastic rocks in the Nadaleen North package that belong to the Mesoproterozoic Ice Brook Formation (Fig. 2.2) (Colpron et al., 2013a; Moynihan et al., 2014). These rocks are juxtaposed against the south-younging Conrad and Osiris packages to the south by the NNE-dipping reverse Nadaleen Fault zone (Figs. 2.1D, 2.2). All rocks in the Conrad succession correlate with the undivided Nadaleen formation of latest Neoproterozoic age and Osiris sequence rocks belong to the Stenbraten member of the Nadaleen formation, and the late Neoproterozoic Gametrail and Blueflower formations (Fig. 2.2) (Colpron et al., 2013a; Moynihan et al., 2014). The boundary between the Conrad and Osiris stratigraphic packages is defined by a color difference between the grey shale of the Conrad succession and the overlying red Osiris shale. The contact relationship is unclear as it is unexposed, but may be conformable. The Conrad succession is primarily composed of fine-grained siliciclastic rocks and lesser carbonate rocks and carbonate conglomerate units. The overlying Osiris package is dominated by carbonate rocks with lesser siliciclastic rocks. Gabbroic dikes (ca. 74 – 65 Ma; Bennett, 2013; M. Tucker, personal communication) occur adjacent to the Nadaleen Fault zone (Fig. 2.1D). Detailed rock descriptions and photos are given in Appendix A.

2.2.2 Deformation

Disruption of the passive margin occurred during the Late Triassic to Early Jurassic as a result of eastward subduction and island arc collision along the western margin of the continent that marked the onset of Cordilleran deformation (Nelson et al., 2013). As a result, NNE-vergent, thin-skinned thrust faults and folds formed throughout the Selwyn Basin and Mackenzie Platform (Murphy, 1997; Mair et al., 2006; Evenchick et al., 2007; Gehrels et al., 2009; Nelson et al., 2013). Some earlier normal faults, such as the Dawson Thrust (Fig. 2.1C), were inverted such that older basinal rocks of the Selwyn Basin are now juxtaposed against younger rocks of the Mackenzie Platform (Murphy, 1997; Mair et al., 2006, Evenchick et al., 2007; Gehrels et al., 2009; Nelson et al., 2013). The movement sense and dip direction of the Kathleen Lakes fault (Fig. 2.1C) is unclear in the immediate Nadaleen Trend area (Colpron et al., 2013a). Cordilleran deformation also resulted in igneous activity near the plate margin (Coast Belt) and within the Selwyn Basin (Monger et al., 1982; Gordey and Anderson, 1993; Monger and McNicoll, 1993; Murphy, 1997; Nelson et al., 2013). Igneous rocks within the Selwyn Basin generally belong to the Tombstone (94 – 90 Ma) and McQuesten (67 – 61 Ma) plutonic suites (Murphy, 1997). Granitic aplite and pegmatite in the Rau Trend in the western Rackla Gold Belt are considered to be related to the McQuesten plutonic suite and have yielded 62 – 59 Ma $^{40}Ar/^{39}Ar$ muscovite ages (Kingston et al., 2009).

2.2.3 Mineralization

Au at the eastern Nadaleen Trend occurs as very fine-grained disseminated particles primarily in carbonate rocks although some Au occurs in siliciclastic rocks. Au in the Conrad zone occurs within the *Conrad limestone* and the overlying *Conrad siliciclastic rocks* in the Conrad sequence and Au in the Isis East, and Osiris/Sunrise zones occurs in the *Osiris limestone* and overlying *Osiris dolostone* within the Osiris sequence (Fig. 2.2). Alteration signatures at the Conrad zone consist of decalcification with subsequent silicification and brecciation (Tucker et al., 2013). The Conrad zone features abundant late-ore stage, open-space filling minerals including realgar, orpiment, illite, fluorite, and calcite (Tucker et al., 2013). The alteration signatures and open space filling minerals as well as the structural and stratigraphic position of the Conrad zone within the region led Tucker et al. (2013) to suggest that the Conrad zone is a ‘Carlin-type deposit’ similar to prolific sedimentary rock-hosted Au deposits that occur in Nevada.

2.3 Results

2.3.1 Oriented drill core

Bedding measurements collected from oriented drill core in the Conrad zone (see Appendix B for detailed methods) were plotted and analyzed on stereographic projections using the software OSXStereonet (Cardozo and Allmendinger, 2011). Rock types and structural measurements were plotted on plan view maps at six different levels below the surface (Fig. 2.4). The original elevation datum used for the depths was 1503.2 m, defining the drill collar with the highest elevation. The 100 – 200 m plan view map (Fig. 2.4), for example, displays measurements derived from elevations between 1403.2 – 1303.2 m. Geologic contacts were

Figure 2.4: Plan view map stack showing rock type and basic (black dots) and oriented drill core sites (circles, colored for purposes explained in Fig. 2.4). Equal-angle lower-hemisphere projections show bedding measurements from all oriented drill core data per section. Great circles are indicated where measurements show fold geometry rather than clusters.

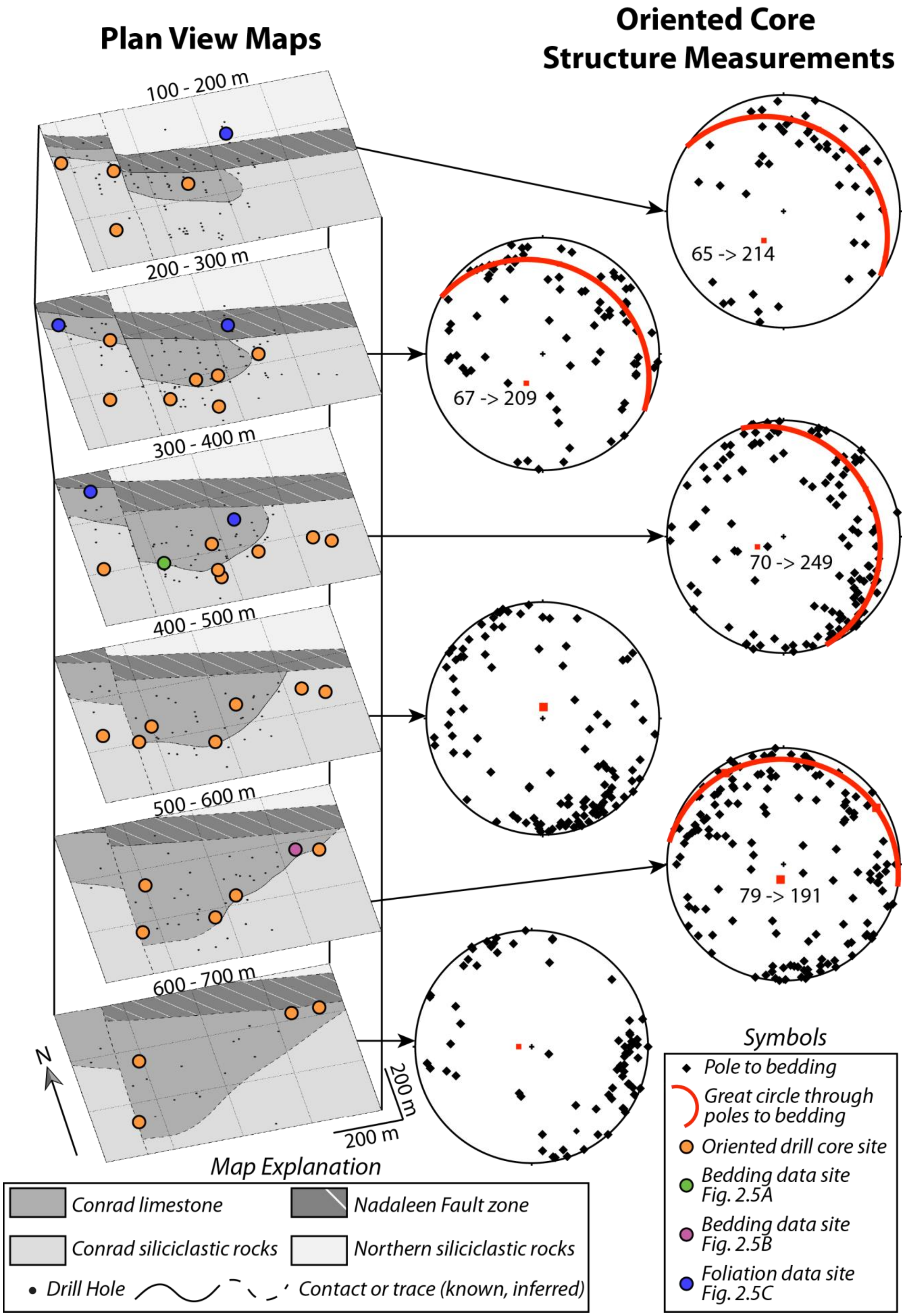
Plan View Maps
Oriented Core Structure Measurements
100 - 200 m
200 - 300 m
300 - 400 m
400 - 500 m
500 - 600 m
600 - 700 m
65 -> 214
67 -> 209
70 -> 249
79 -> 191
N
200 m
200 m
Map Explanation
Conrad limestone
Nadaleen Fault zone
Conrad siliciclastic rocks
Northern siliciclastic rocks
Drill Hole
Contact or trace (known, inferred)
Symbols
Pole to bedding
Great circle through poles to bedding
Oriented drill core site
Bedding data site Fig. 2.5A
Bedding data site Fig. 2.5B
Foliation data site Fig. 2.5C

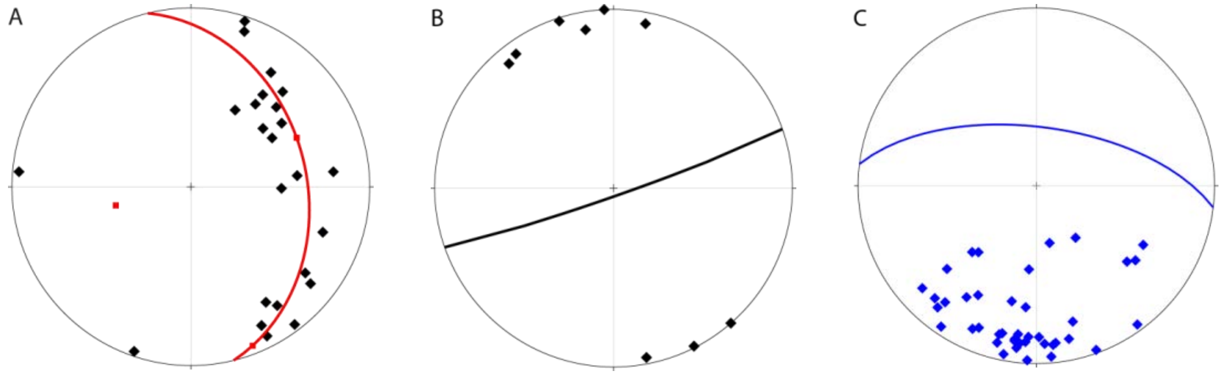

Figure 2.5: Equal-area lower-hemisphere projections of structural data from oriented drill core within the Conrad Au zone. A. Poles to bedding from drill hole 157 in the 300 – 400 m map (green circle; Fig. 2.4) suggest a W-plunging fold. The red great circle defines the fold geometry among the bedding poles. B. Poles to bedding from drill hole 193 in the 500 – 600 m map (purple circle; Fig. 2.4) suggest sub-vertical, ENE-striking, generally planar bedding. Great circle shows the average orientation of planar bedding C. Poles to foliation measurements collected from all oriented drill holes intersecting the Nadaleen Fault zone (blue circles; Fig. 2.4) show an average orientation of 277°/67° (blue great circle).

interpreted from all 99 drill holes. All oriented drill core structural measurements are given in Appendix C. Planar measurements are given in strike and dip using right-hand-rule and linear measurements are in trend and plunge.

Individual oriented drill holes indicate that bedding in some areas is strongly folded (Fig. 2.5A) while in other areas it is generally planar (Fig. 2.5B). Individual folds typically plunge steeply between north, west, or south. The NNE-dipping Nadaleen Fault zone cuts off the Conrad zone to the N (Fig. 2.4) and foliation within it has an average orientation of 277°/67° (Fig. 2.5C). The N-trending, right-lateral Conrad Fault offsets all rock types (Fig. 2.4). Geologic contacts in the top two maps (100 – 300 m) appear to outline an ESE-trending fold, while all sections below this (300 – 700 m) suggest a SSW-trending fold. Insufficient oriented drill core measurements were collected to define a fold in the hinge area of the apparently ESE-plunging fold. Structural measurements show that most levels are characterized by steeply SSW- to WSW-plunging folds that steepen with increasing depth (Fig. 2.4), and no evidence exists for an ESE-plunging fold from the structural data. Individual folds in a SSW- to WSW- orientation generally occur adjacent to and within 150 m east of the Conrad Fault.

2.3.2 Surface mapping

The geology of the eastern Nadaleen Trend is dominated by moderately to steeply S- to SSW-plunging anticlines that host the Osiris, Isis East, and Conrad Au zones (Figs. 2.1D, 2.6). The E-trending, right-lateral Osiris Fault offsets the Isis East and Osiris anticlines and juxtaposes the carbonate conglomerate unit against itself, resulting in a large apparent thickening of the unit between the Conrad and Osiris zones (Figs. 2.1D, 2.6, 2.7). The Osiris and Conrad stratigraphic packages are cut off to the N by the NNE-dipping Nadaleen Fault zone (Figs. 2.1D, 2.6, 2.7). Gabbroic dikes occur throughout the area adjacent to the Nadaleen Fault zone (Figs. 2.1D; 2.6, 2.7). Surface structural geology is described for the Nadaleen North, Conrad, and Osiris stratigraphic packages below. Structural measurements displayed in Figure 2.6 are included in Appendix D.

The most characteristic structural feature within *North of Nadaleen* rocks is intense cleavage that occurs at an orientation that is variable (Fig. 2.6) but most commonly sub-parallel to foliation in the Nadaleen Fault zone (277°) (Fig. 2.5C). Poles to bedding define a folded geometry in the *North of Nadaleen* domain (Fig. 2.6). The average strike of bedding (294°) is similar to the average strike of foliation in the Nadaleen Fault zone.

Conrad stratigraphic package rocks are characterized by map- to hand sample-scale, open to tight chevron folds in a variety of orientations. Cm- to m-scale folds exist in the *N-Limb*, *N-Limb on Ridge*, and the *Fe-oxide Ridge* domains (Fig. 2.8C). Steeply SSW-plunging folds occur throughout the *Conrad Anticline* domain (Fig. 2.8E). The *N-Fold in Carbonate Conglomerate* and *S-Fold in Carbonate Conglomerate* domains show a map-scale anticline-syncline pair with fold axes plunging in opposite directions (Figs. 2.6; 2.8A).

Rocks in the Osiris domain are deformed by map- to hand sample-scale, open to tight chevron folds in several orientations. Bedding in the *Go Home Creek* zone is overturned (Kuiper, 2012). The axial traces of the *Osiris Anticline* and the *Isis East Anticline* occur in similar orientations and are nearly in line. The right-lateral Osiris Fault offsets the two anticlines and is characterized by fault gouge and breccia. The ESE limb of the *Osiris Anticline* dips moderately to the south and the WNW limb is generally sub-vertical and SSW-trending (Kuiper, 2012). The WNW limb of the *Isis East Anticline* dips steeply to the WSW and the E limb dips steeply SSW

Figure 2.6: Map of the eastern Nadaleen Trend showing structural domains, domains names, cross-section lines, and equal-area lower-hemisphere projections showing structural measurements and average orientations, superimposed on the geology of Fig. 2.1D. Colors of structural domains and associated projections reflect general fold orientations.

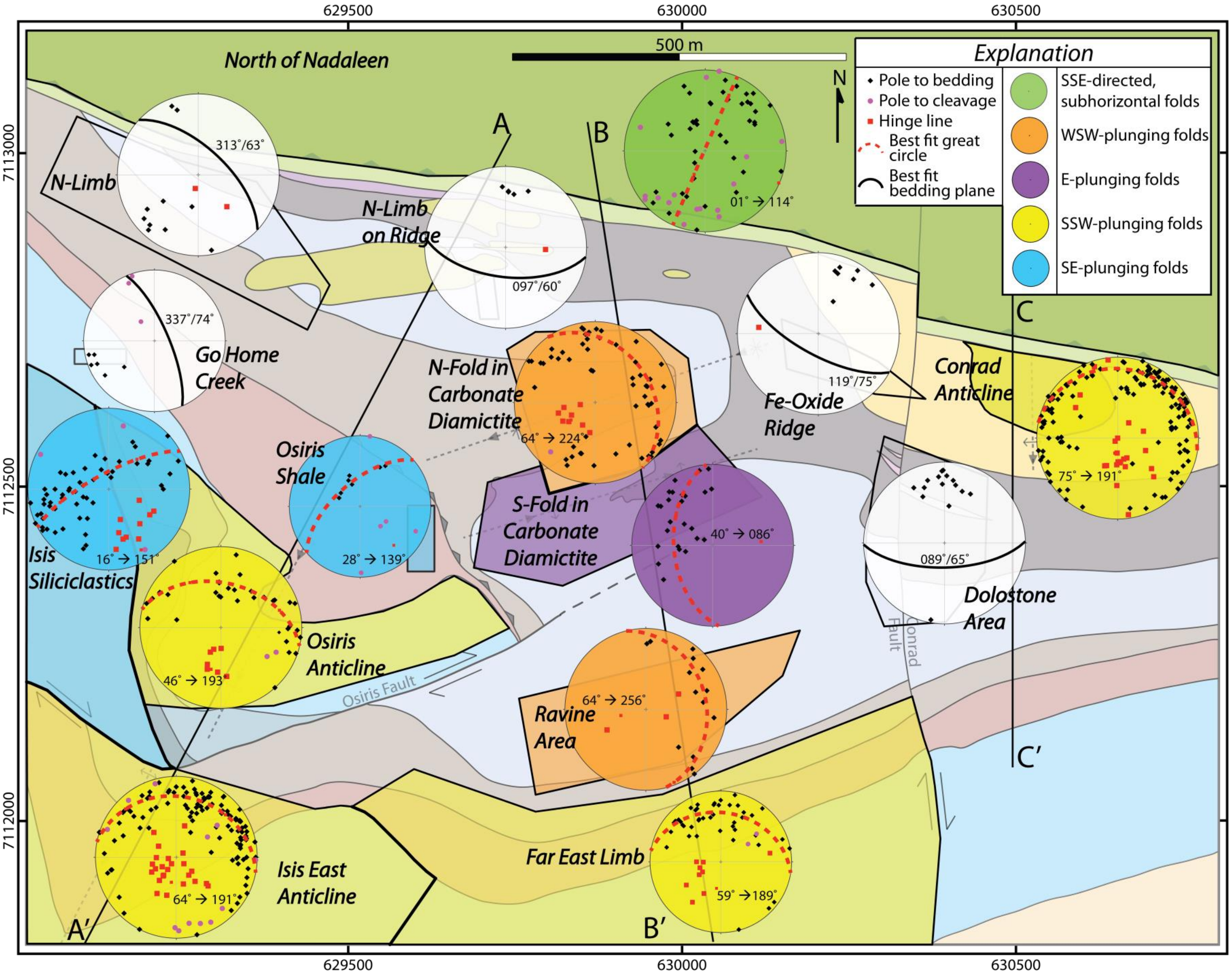

629500
630000
630500
7113000
7112500
7112000
500 m
N
Explanation
Pole to bedding
Pole to cleavage
Hinge line
Best fit great circle
Best fit bedding plane
SSE-directed, subhorizontal folds
WSW-plunging folds
E-plunging folds
SSW-plunging folds
SE-plunging folds
North of Nadaleen
N-Limb
313°/63°
N-Limb on Ridge
097°/60°
01° → 114°
A
B
C
Go Home Creek
337°/74°
119°/75°
Fe-Oxide Ridge
Conrad Anticline
N-Fold in Carbonate Diamictite
64° → 224°
Osiris Shale
28° → 139°
Isis Siliciclastics
16° → 151°
S-Fold in Carbonate Diamictite
40° → 086°
089°/65°
Dolostone Area
75° → 191°
Osiris Anticline
46° → 193°
Osiris Fault
Conrad Fault
Ravine Area
64° → 256°
C′
Isis East Anticline
64° → 191°
Far East Limb
59° → 189°
A′
B′

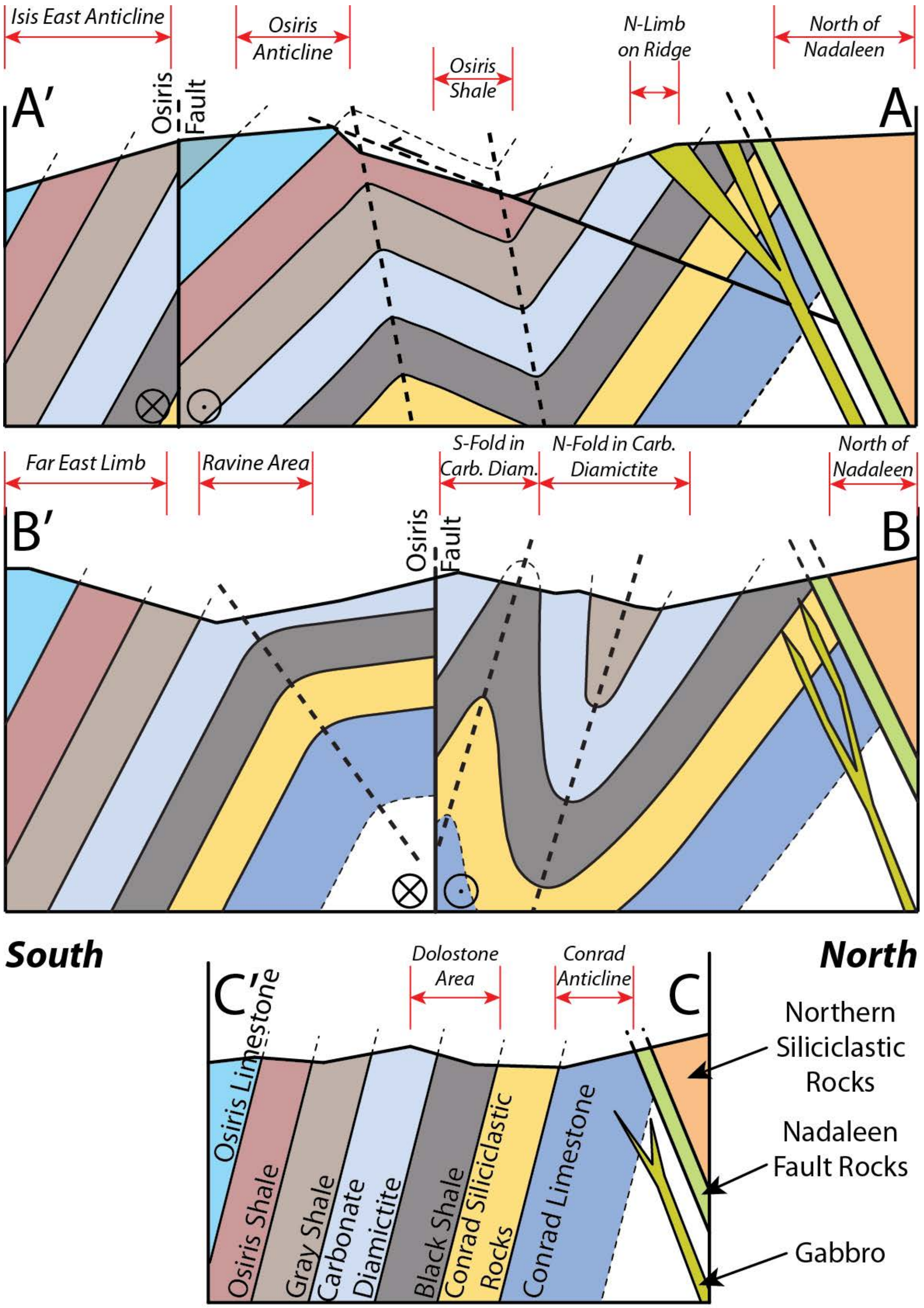

Figure 2.7: Geologic cross sections. See Fig. 2.6 for location. Structural domain names indicated above the sections. Colors as in Fig. 2.2.

Figure 2.8: Outcrop photos within the eastern Nadaleen Trend. A. Rock units, exposed and inferred contacts, and fault and fold traces within the eastern Nadaleen Trend. Photo taken from the eastern *North of Nadaleen* domain, looking southwest (see Fig. 2.6). B. Foliation and elongate clasts in fault rock of the Nadaleen Fault zone. C. Close chevron folds in Conrad siliciclastic rocks on *Fe-Oxide Ridge* (see Fig. 2.6). D. Parasitic fold in the Osiris limestone on the SE limb of the *Osiris Anticline*, looking south (see Fig. 2.6). E. Detailed structure map of a well-exposed and representative outcrop of Conrad limestone in the *Conrad Anticline* domain, looking north (see Fig. 2.6).

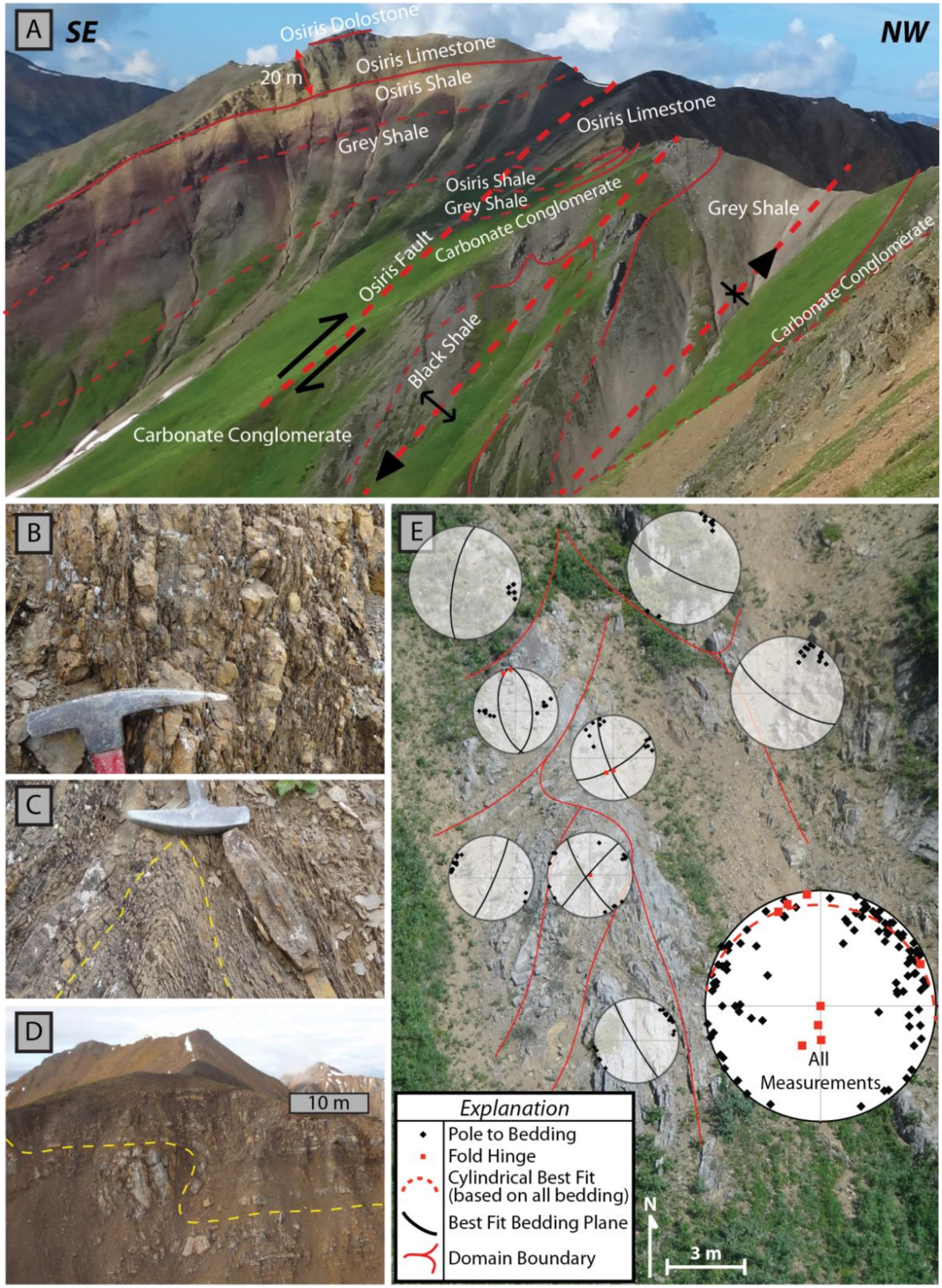
A
SE
NW
Osiris Dolostone
Osiris Limestone
20 m
Osiris Shale
Grey Shale
Osiris Limestone
Osiris Shale
Grey Shale
Carbonate Conglomerate
Grey Shale
Osiris Fault
Carbonate Conglomerate
Black Shale
Carbonate Conglomerate
B
C
D
10 m
E
All Measurements
Explanation
Pole to Bedding
Fold Hinge
Cylindrical Best Fit (based on all bedding)
Best Fit Bedding Plane
Domain Boundary
N
3 m

(Kuiper, 2012).The *Osiris Anticline* and the *Isis East Anticline* both contain cm- to m-scale parasitic folds (Fig. 2.8D) in an orientation similar to the map-scale fold.

2.3.3 Quadrangle map analysis

The trends of reverse faults and fold axial traces throughout the Nadaleen region were compiled from regional maps (Fig. 2.9) and all measurements are given in Appendix E. Reverse faults in the *Osiris Assemblage*, the *Upper Plate Dawson Thrust*, and the *Eastern Nadaleen* domains generally reflect N- to NW-vergence, while S-vergent reverse faults occur in the *Nadaleen Area*, *North of Nadaleen*, and *Northeast of Nadaleen* domains. No map-scale reverse faults occur in the *Northwest* domain.

Fold trends throughout the Nadaleen region show variations near the eastern Nadaleen Trend. Folds in the *Northwest*, *Overlap Assemblage*, *Upper Plate Dawson Thrust*, and *Northeast Nadaleen* domains generally trend ESE, in the *Eastern Nadaleen* domain they trend SE, in the *North of Nadaleen* domain they trend NE to ENE and in the *Nadaleen Area* they trend NE to E (Fig. 2.9).

2.4 Deformation history

Map-scale structures at the eastern Nadaleen Trend include: (1) four moderately to steeply S- to SSW-plunging anticlines, (2) WSW-, SE-, and E-plunging folds, (3) the E-trending dextral strike-slip Osiris Fault, (4) the NNE-dipping Nadaleen fault zone, and (5) the N-trending dextral strike-slip Conrad Fault (Figs. 2.1D, 2.6). The pre-Nadaleen Fault zone structures may have formed in various ways: (1) W-vergent folding and (contemporaneous or subsequent) top-to-the-W thrust faulting along the Osiris Fault, followed by tilting to the south; (2) W-vergent folding, then tilting to the south, then right-lateral strike- slip faulting along the Osiris Fault; (3) tilting to the south, followed by dextral simple shear motion resulting in folding and (contemporaneous or subsequent) strike-slip faulting. The first two models require top-to-the-W transport to form the SSW-plunging folds; however, such a transport direction is not recognized regionally. Furthermore, the first model uses the Osiris Fault as a thrust detachment surface. If true, it would be expected that it continues to the east as a sole thrust; however, it ends locally.

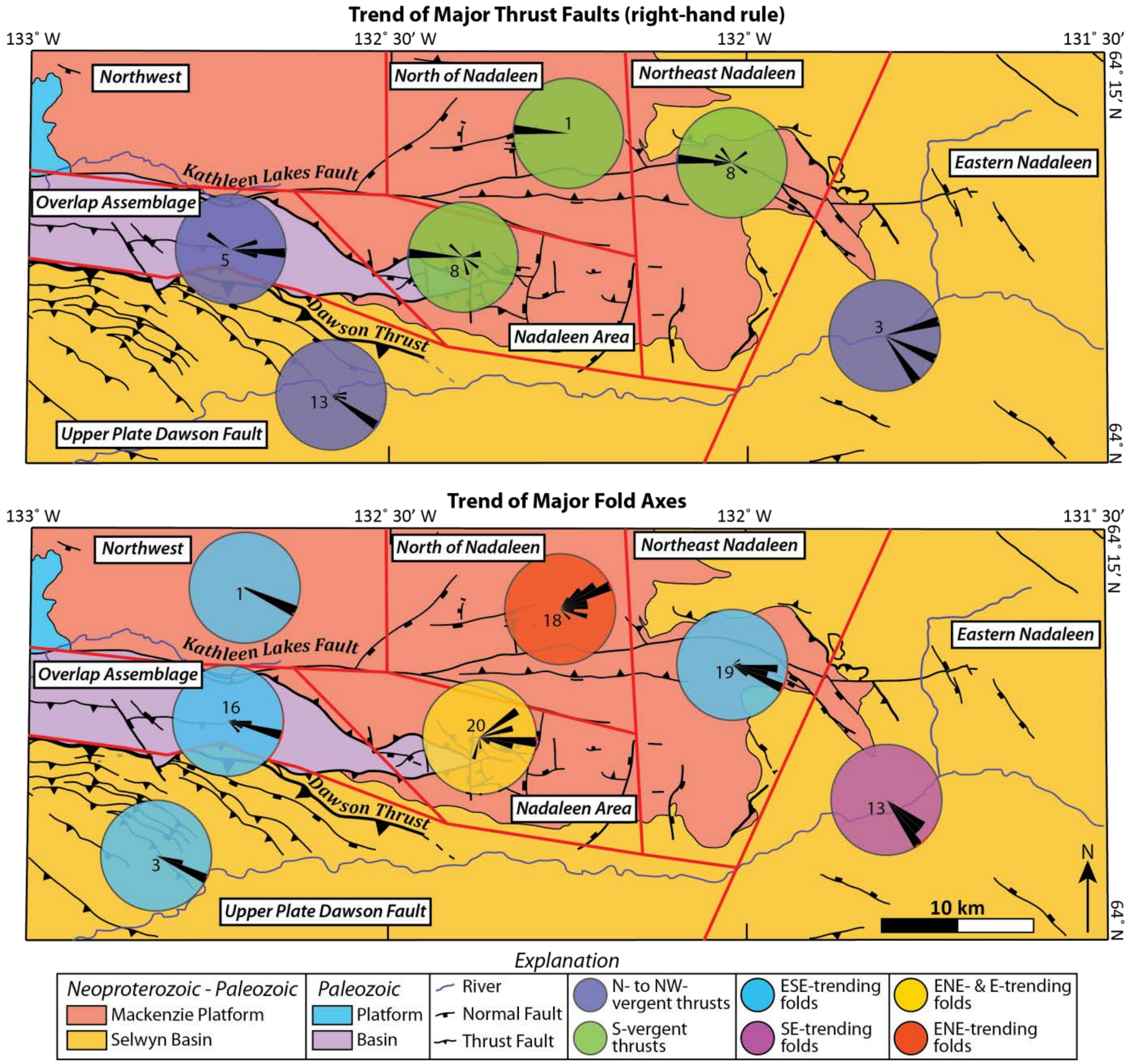

Figure 2.9: Reverse fault trend (right-hand rule) and fold axial trace orientation analysis of regional quadrangle maps near the Nadaleen Trend. Dips and plunges were not published on the maps and therefore not recorded here. Map location defined in Figure 2.1B. Modified from Colpron et al. (2013a) and Moynihan et al. (2014).

The third model is consistent with regionally recognized structures and deformation events, and is therefore our preferred model. It is described in detail below.

The first deformation event most likely involved tilting of the rocks towards a steep SSW dip as a result of NNE-SSW directed shortening (Fig. 2.10: D_1). Subsequent E-directed dextral simple shear resulted in generally SSW-plunging Z-folds, such as the Osiris and Isis East anticlines (Figs. 2.7, 2.10: *Early* D_2). Continued NW-SE-directed shortening further folded the

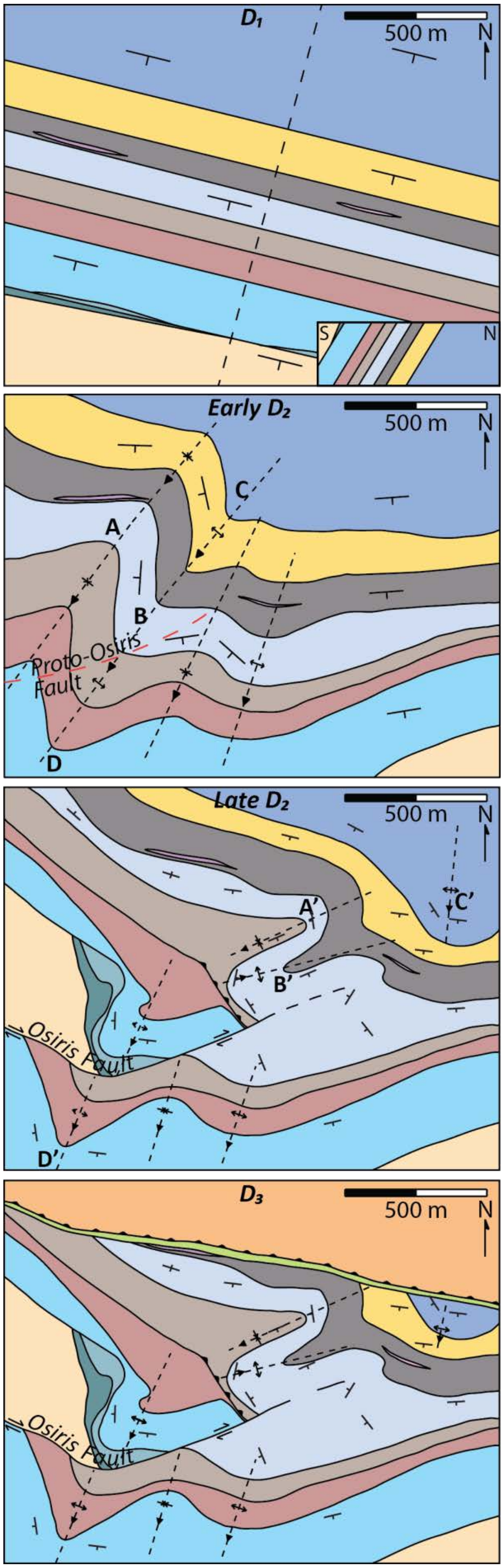

Figure 2.10: Interpreted structural evolution of the eastern Nadaleen Trend. See text for discussion.

rocks to a breaking point that resulted in the formation of the Osiris Fault (Fig. 2.10: *Late D_2*). Offset along the Osiris Fault placed the axial traces of the Osiris and Isis East anticlines nearly in line (Fig. 2.10: Late D_2). Rheological contrasts between competent limestone units and weak shale units resulted in local thickening of the Osiris and grey shale units in the hinge zone of the Osiris anticline that is interpreted to have also caused: (1) rotation of previously folded northern carbonate conglomerate rocks from SW-trending (A; Fig. 2.10: Early D_2) to more westward trending (A'; Fig. 2.10: Late D_2) and (2) tilting of the southern fold in the carbonate conglomerate from SW-plunging (B; Fig. 2.10: Early D_2) to E-plunging (B'; Fig. 2.10: Late D_2). Local N-S thickening of the Osiris and Grey Shale units also likely translated the Conrad Anticline eastward (C-C'; Fig. 2.10). N-S directed shortening (D_3) then resulted in the activation of the Nadaleen Fault zone. Intrusion of gabbroic dikes (ca. 74 – 65 Ma) is interpreted to have been controlled by the Nadaleen Fault zone because the rocks occur only in the immediate footwall of the fault. If true, this sets a minimum age constraint for the end of D_3. Dextral offset along the north-trending Conrad Fault (D_4) represents the final phase of deformation in the trend. This particularly unique sequence of deformation events is not known to be duplicated anywhere else in the immediate region; however, several structurally complex zones have been observed throughout Mackenzie Platform and Selwyn Basin and are interpreted to have resulted from deformation imposed on rheologically heterogeneous sedimentary rocks (Gabrielse, 1967; Stockwell, 1969; Norris, 1974; Gordey and Thompson, 1991; McMechan et al., 1991; Cecile, 2000; Mair et al., 2006).

Certain events within the deformation sequence outlined above have been recognized regionally. NNE-SSW directed shortening and tilting (D_1) is consistent with numerous regional large thrust faults and associated imbricate thrust packages and folds that are interpreted to result from mid-Cretaceous NNE-directed fold-thrust transport (Mortensen, 1982; Murphy, 1997; Roots, 1997; Stephens et al., 2004; Evenchick et al., 2007; Nelson and Colpron, 2007; Gehrels et al., 2009; Nelson et al., 2013). SW-directed folds and S-vergent reverse faults (D_2 and D_3, respectively) have not been documented anywhere in the region; however, similar structures occur north of the eastern Nadaleen Trend (Colpron et al., 2013a; Moynihan et al., 2014). Minor dextral offset along north-trending faults (Conrad fault; D_4) has not been observed regionally and may just be a local feature as the offset is only ~50 m.

Below, we integrate our local structural observations in the eastern Nadaleen Trend with regionally observed structures in order to understand why the observed sequence of deformation events has not been observed anywhere else regionally, and to potentially explain why Au occurs in the area. Opposite reverse fault vergence north and south of the eastern Nadaleen Trend indicates that a triangle zone exists across the eastern Nadaleen Trend. Triangle zones are known to occur in a variety of locations, such as the frontal toes of fold thrust belts (Gordy et al., 1977; Jones, 1996; Couzens and Wiltschko, 1996) or above basement structures such as normal faults (Woodward, 1985; Çemen et al., 2002) and have been studied in great detail because of the role they play in the formation of large hydrocarbon traps (MacKay, 1996; Zapata and Allmendinger, 1996; Couzens-Schultz et al., 2003). An interpreted analog to the triangle zone across the eastern Nadaleen Trend occurs in the Wilburton gas field of southeastern Oklahoma, USA (Fig. 2.11). Similar to the eastern Nadaleen Trend, the Wilburton triangle zone is characterized by oppositely verging thrust faults, the stratigraphic section is composed of rocks of widely variable competency, and imbricate thrust faults stack up against the primary foreland-directed detachment fault (Woodward, 1985; Çemen et al., 2002). The Wilburton triangle is interpreted to lie above a basement normal fault (Woodward, 1985; Çemen et al., 2002), which may also be true for the eastern Nadaleen Trend (discussed below). The N-vergent Dawson Thrust at the

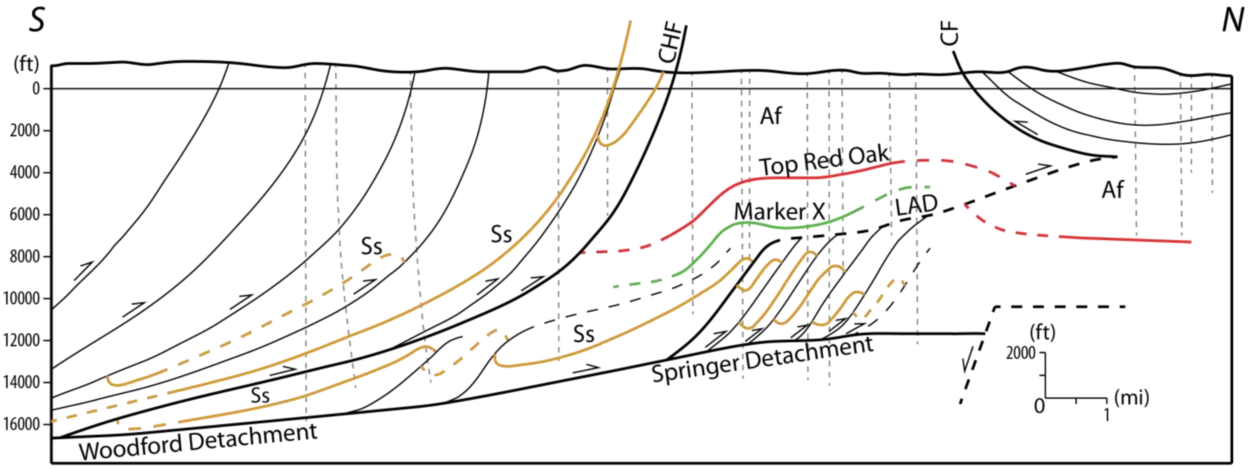

Figure 2.11: Cross-section of a triangle zone in the Wilburton gas field of the Arkoma Basin in southeastern Oklahoma derived from surface structural mapping, wire-line well logs, and 2D seismic data (Çemen et al., 2002). Dashed lines indicate drill holes. Abbreviations: CF – Carbon fault, CHF – Choctaw fault, LAD – Lower Atokan Detachment, Ss – Spiro Sandstone, Af – Atoka Formation. Modified from Çemen et al. (2002).

eastern Nadaleen Trend may be analogous to the Choctaw Fault (CHF), south vergent reverse faults north of the eastern Nadaleen Trend may be analogous to the Carbon Fault (CF), and the eastern Nadaleen Trend resides in the middle, equivalent to the area where much of the gas accumulated in the Wilburton field (Fig. 2.11).

The eastern Nadaleen Trend triangle zone occurs in a zone marked by a number of other regional-scale geologic transitions. It is situated near the southeastern margin of the Mackenzie Platform and at the eastern margin of the Paleozoic offshelf rocks (Figs. 2.1C; 2.9). West of the area, Proterozoic basin architecture from Mackenzie Platform to Selwyn Basin has been interpreted as steep across the proto-Dawson Thrust, whereas to the east it is interpreted as gentler where the Dawson Thrust does not exist (Abbott, 1997; Norris, 1997; Mair et al., 2006; Macdonald et al., 2012). The triangle zone lies near the eastern edges of the Dawson Thrust and Kathleen Lakes fault (Figs. 2.1C; 2.9). Also, fold axis orientations change from SSE- to SE-trending west, south, and east of the eastern Nadaleen Trend, to NE- and E- trending at and north of the area (Fig. 2.9). Finally, the eastern Nadaleen Trend triangle zone is a discrete feature and is generally confined to within ~10 km west and east of the eastern Nadaleen Trend.

West of the eastern Nadaleen Trend, numerous reverse faults and fold axial traces in the *Upper Plate Dawson Thrust* and *Overlap Assemblage* domains (Fig. 2.9) are parallel to structures elsewhere in the Selwyn Basin that formed during Mesozoic fold-thrust deformation (Mortensen, 1982; Murphy, 1997; Roots, 1997; Stephens et al., 2004; Evenchick et al., 2007; Nelson and Colpron, 2007; Gehrels et al., 2009; Nelson et al., 2013). In the *Northwest* domain, there are no map-scale reverse faults and only one mapped fold that trends ESE (Fig. 2.9) (Colpron et al., 2013a; Moynihan et al., 2014).Thus, the number of folds, and therefore the amount of strain, decreases significantly towards the north, with little strain north of the *Overlap Assemblage*. East of the eastern Nadaleen Trend, fold orientations in the *Eastern Nadaleen* and *Northeast Nadaleen* domain dominantly reflect NNE-vergent deformation throughout the domain and S-vergent structures have not been mapped.

The regional structural geology to the west, east, and at the eastern Nadaleen Trend are each unique and are collectively interpreted to suggest the influence of an obstruction that may end at or just east of the eastern Nadaleen Trend. It is interpreted to have presented a barrier to NNE-directed fold thrust movement west of the eastern Nadaleen Trend that likely shielded the *Northwest* domain from deformation. Across the eastern Nadaleen Trend, the edge of the obstruction presented only a minor barrier to NNE-directed fold-thrust movement, permitting transported rocks to override the barrier and detach rocks in the foreland to form a triangle zone similar to the Wilburton gas field example (Fig. 2.11). East of the eastern Nadaleen Trend, the obstruction does not exist and fold-thrust movement occurs throughout the *Eastern Nadaleen* domain (Fig. 2.9). The reasons for the interpreted obstruction may include: (1) rheological heterogeneity between more competent platform rocks of the Mackenzie Platform and less competent basin rocks of the Selwyn Basin or (2) a subsurface structure, such as a basement normal fault similar to the Wilburton gas field, or the basement high of Colpron et al. (2013). We believe that the location and abrupt nature of both the Neoproterozoic and Paleozoic platform-to-basin transitions (Abbott, 1997; Norris, 1997; Mair et al., 2006; Macdonald et al., 2012) were controlled by a pre-existing or syn-sedimentary structure. It is therefore likely that the same structure may also have been the reason for the later obstruction, and that the obstruction was not caused by rheological heterogeneity alone. Colpron et al.'s (2013b) basement high model could be that structure and account of the regional deformation patterns; however, based on structural similarities between the eastern Nadaleen Trend region and the Wilburton gas field (Fig. 2.11), we present a new model that involves a single subsurface basement normal fault herein called the Rackla Fault (Fig. 2.12).

If it exists, the Rackla Fault influenced deformation similar to how the normal fault in the basement influenced the structural geometry in the Wilburton gas field (Fig. 2.11). Offset along the Rackla Fault may have obstructed NNE-directed fold-thrust movement that shielded the *Northwest* domain from deformation and presented a minor barrier across the eastern Nadaleen Trend that was overridden during fold-thrust movement leading to the formation of a triangle zone. Because it potentially controls both Neoproterozoic and Paleozoic basin architecture as well as mid-Cretaceous deformation patterns, it likely formed early in the geologic history of the region (early Neoproterozoic?).

Regardless of the reason for the obstruction, there exists an interface between obstructed and unobstructed material that can be thought of as a sinistral strike-slip zone, with a boundary parallel to the fold-thrust transport direction in the unobstructed domain (Fig. 2.12). The general orientation of the transport direction is interpreted to be perpendicular to the average strike of reverse faults and fold axes in the unobstructed *Eastern Nadaleen* and *Northeast Nadaleen* domains because those structures were presumably not rotated during deformation or overprinted

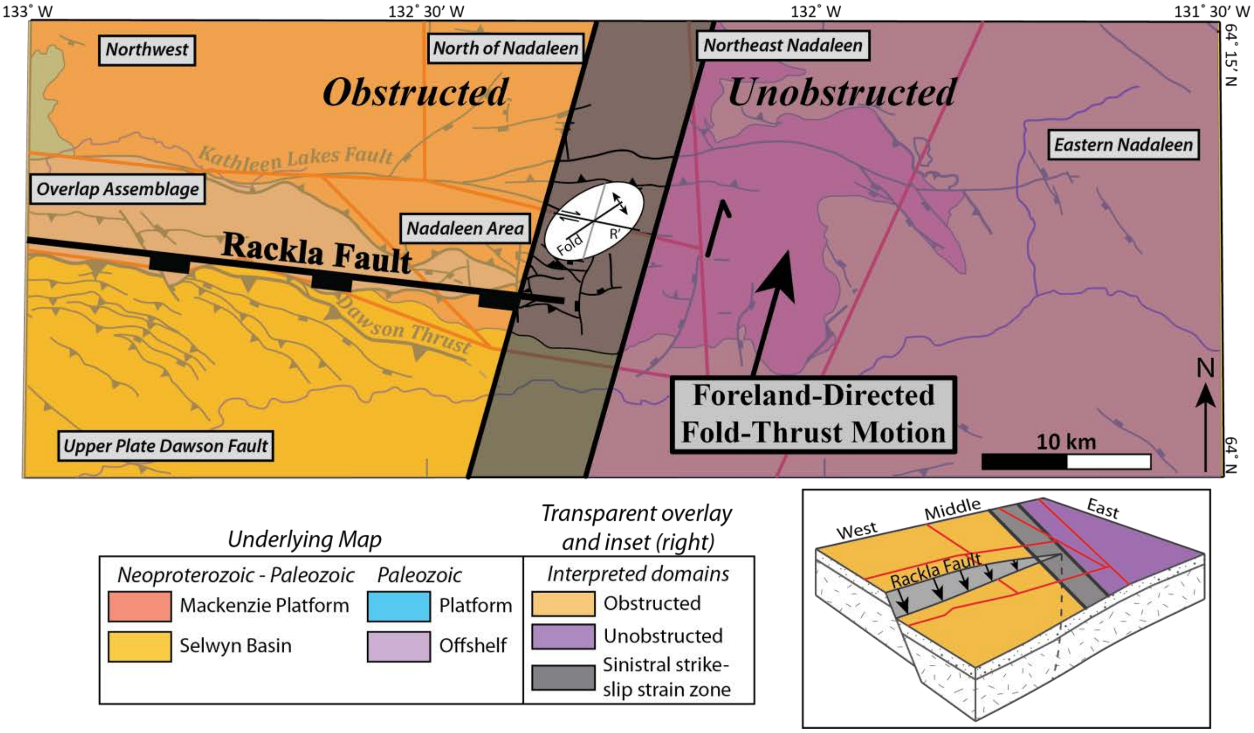

Figure 2.12: Schematic structural domain map showing a western domain where foreland-directed fold-thrust motion is obstructed towards the north, an eastern domain, where deformation is unobstructed, and a zone of sinistral shear in between. Inset shows interpreted basement surface and the corresponding interpreted domains. See text for discussion. Underlying map modified from Colpron et al. (2013a) and Moynihan et al. (2014).

by later deformation. Folds resulting from strain during shear are likely to form in a SW-trending orientation (Fig. 2.12) similar to folds that occur throughout and north of the eastern Nadaleen Trend (Fig. 2.9). The easterly trend of the antithetic (dextral) Riedel shear orientation (Fig. 2.12) is consistent with that of the Osiris Fault, suggesting a connection with interpreted dextral shear during D_2 within the eastern Nadaleen Trend (Figs. 2.6; 2.10). The SSW-vergent Nadaleen Fault zone within the eastern Nadaleen Trend is probably related to the triangle zone across the eastern Nadaleen Trend and may be the primary detachment fault or a subsidiary splay off an undetermined main detachment fault (Kathleen Lakes Fault?).

2.5 Ore fluid migration and potential controls

Our work in the eastern Nadaleen Trend indicates that the major Au discoveries (Conrad, Isis East, Osiris/Sunrise) are hosted within hinge zones of moderately to steeply S- to SSW-plunging anticlines and not within the hinge zones of synclines and/or folds in other orientations. This suggests that within the eastern Nadaleen Trend, the hinge lines of anticlines may have served as conduits for ore fluid and locations of increased ore fluid-rock interaction. At a regional scale, such anticlines are not recognized and other larger structures may have (partially) controlled the ore fluid flow path.

The triangle zone across the eastern Nadaleen Trend may have behaved as a structural funnel, channeling ore fluid upwards into traps within the zone. This model is similar to those for hydrocarbon migration and accumulation, e.g. the Wilburton gas field (Fig. 2.11) and many other triangle zones throughout the world (MacKay, 1996; Zapata and Allmendinger, 1996; Couzens-Schultz et al., 2003). The Wilburton triangle zone channeled hydrocarbons upwards into structural culminations formed as a result of triangle zone deformation (Çemen et al., 2002). In a similar sense, Au-rich ore fluid may have migrated updip along the base of the Dawson thrust, using the thrust sheet as a regional aquitard. The eastern Nadaleen Trend is located along a major fluid migration pathway, and the distribution of Au zones within the eastern Nadaleen Trend suggests that S- to SSW-plunging antiforms were effective fluid conduits.

2.6 Structural differences with Carlin-type deposits in Nevada

Carlin-type deposits in Nevada are generally understood to have formed between ~42 and 36 Ma, coeval with the beginning of NW- to W-directed extension, during which favorably oriented older contractional structures were reactivated (Cline et al., 2005). Reactivation enhanced the permeability of the structural network and allowed for more pervasive passive ore fluid circulation through the crust (Cline et al., 2005). Most Carlin-type deposits in Nevada are located within 250 m of multi-hundred km-scale thrust faults that are interpreted as regional aquitards (Cline et al., 2005). The deposits are also typically associated with extensional faults that cross-cut earlier anticlines (Cline et al., 2005).

The eastern Nadaleen Trend Au zones are associated with anticlines and generally occur near faults such as the Osiris Fault or the Nadaleen Fault zone. Widespread extensional deformation as in Nevada has not been recognized locally or regionally; however, east and west of the eastern Nadaleen Trend, N- to NNE-trending normal faults exist (Fig. 2.9) that form large valleys in between mountain ranges. Au has not been discovered near or in any spatial association with these faults and they are not believed to have played a role in ore fluid circulation. From a regional perspective, the zones occur more than 6 km from the Dawson Thrust, a thrust fault comparable in scale to the primary controlling thrusts in Nevada. The Nadaleen Fault zone may represent the controlling structure; however, this fault is not as regional in extent (~6-7 km) as the controlling thrust faults at Nevada. The lack of extensional structures near the Au zones and of immediate spatial associations with large regional thrust faults present significant differences with Carlin-type deposits in Nevada.

2.7 Conclusion

The local structural complexity of the 6 km^2 area within the eastern Nadaleen Trend is characterized by: (1) generally southerly-dipping bedding, (2) several hundred-meter scale, open to tight chevron folds that plunge moderately to steeply to the SSW, WSW, SE, and E, (3) the E-trending dextral Osiris Fault, (4) the steeply NNE-dipping Nadaleen Fault zone and (5) the late N-trending dextral Conrad Fault. These are interpreted to have resulted from: NNE-SSW directed shortening (D_1), NW-SE directed shortening and dextral simple shear, (D_2), N-S directed shortening (D_3) and minor N-trending dextral strike-slip (D_4). Similar combinations of structures have not been recognized anywhere else regionally, and they may have been a result of regional structures and/or competency contrasts between rock units.

Oppositely verging reverse faults indicate that an east-trending triangle zone exists across the eastern Nadaleen Trend that does not exist to the west or east. Rocks to the west show multiple NNE-verging structures in the south and only one fold in the north while rocks to the east consistently show NNE-vergence. The structural architecture of the region may be influenced by a subsurface structure such as the interpreted Rackla Fault at and west of the eastern Nadaleen Trend. Such a subsurface structure may have obstructed fold-thrust movement to the west, and presented a minor obstruction at the eastern Nadaleen Trend resulting in the formation of a triangle zone. NNE-directed transport was unobstructed to the east, and a NNE-trending, sinistral strike-slip shear zone interface exists between the unobstructed and obstructed zones. NE-trending folds within and north of the eastern Nadaleen Trend are oblique to the regional ESE- and SE-trending structures and may have been affected by this shear zone.

The eastern Nadaleen Trend triangle zone is believed to have behaved as a structural funnel that channeled Au-rich ore fluid upward into favorable structures in the eastern Nadaleen Trend. The primary detachment faults may have acted as regional aquitards for ascending ore fluid. Au-bearing rocks in the center of the triangle zone are concentrated in moderately to steeply SSW-plunging anticlines that may have been effective ore fluid conduits.

2.8 References

Abbott, G., 1997, Geology of the upper Hart River area, eastern Ogilvie Mountains, Yukon Territory (116A/10, 116A/11): Yukon Geological Survey, Bulletin, v. 9, 92 p.

Bennett, V., 2011, Synthesis report, Internal report, ATAC Resources Ltd., 57 p.

Bennett, V., 2013, U-Pb geochronology report, Internal report, ATAC Resources Ltd., 44 p.

Cardozo, N. and Allmendinger, R., 2011, OSXStereonet 1.9.

Cecile, M.P., 2000, The geology of the northeastern Niddery Lake map area, east central Yukon and adjacent Northwest Territories: Geological Survey of Canada, Bulletin, v. 553, 122 p.

Çemen, I., Sagnak, A. and Akthar, S., 2002, Geometry of the triangle zone and duplex structure in the Wilburton gas field area of the Arkoma Basin, southeastern Oklahoma: Oklahoma Geological Survey, Circular, v. 104, p. 87-98.

Cline, J.S., Hofstra, A.H., Muntean, J.L., Tosdal, R.M. and Hickey, K.A., 2005, Carlin-type gold deposits in Nevada: Critical geologic characteristics and viable models: Economic Geology 100th Anniversary Volume, v. 100, p. 451-484.

Creaser, R.A., Goodwin-Bell, J.A.S. and Erdmer, P., 1999, Geochemical and Nd isotopic constraints for the origin of eclogite protoliths, northern Cordillera: Implications for the Paleozoic tectonic evolution of the Yukon-Tanana terrane: Canadian Journal of Earth Sciences, v. 36, p. 1697-1709.

Colpron, M., Logan, J. and Mortensen, J.K., 2002, U-Pb age constraint for late Neoproterozoic rifting and initiation of the lower Paleozoic passive margin of western Laurentia: Canadian Journal of Earth Sciences, v. 39, p. 133-143.

Colpron, M., Moynihan, D., Israel, S. and Abbott, G., 2013a, Geological map of the Rackla belt, east-central Yukon (NTS106C/1-4, 106D/1): Yukon Geological Survey, Open File 2013-13, 1:50,000 scale, 5 maps and legend.

Colpron, M., Moynihan, D., Israel, S., and Abbott, G., 2013b, Bedrock geology of the Rackla belt (106C/1-4 and 106D/1), southern Nadaleen map area, Yukon Geological Survey: Poster presented at 2013 AME BC Mineral Exploration Roundup Conference, Vancouver, BC, January 28-31, 2013.

Couzens, B.A. and Wiltschko, D.V., 1996, The control of mechanical stratigraphy on the formation of triangle zones: Bulletin of Canadian Petroleum Geology, v. 44, p. 165-179.

Couzens-Schultz, B.A., Vendeville, B.C. and Wiltschko, D.C., 2003, Duplex style and triangle zone formation: Insights from physical modeling: Journal of Structural Geology, v. 25, p. 1623-1644.

Evenchick, C.A., McMechan, M.E., McNicoll, V.J. and Carr, S.D., 2007, A synthesis of the Jurassic-Cretaceous tectonic evolution of the central and southeastern Canadian Cordillera: Exploring links across the orogen: Geological Society of America, Special Paper, v. 433, p. 117-145.

Gabrielse, H., 1967, Tectonic evolution of the northern Canadian Cordillera: Canadian Journal of Earth Sciences, v. 4, p. 271-298.

Gehrels, G., Rusmore, M., Woodsworth, G., Crawford, M., Andronicos, C., Hollister, L., Patchett, J., Ducea, M., Butler, R., Klepeis, K., Davidson, C., Friedman, R., Haggart, J., Mahoney, B., Crawford, W., Pearson, D. and Girardi, J., 2009, U-Th-Pb geochronology of the Coast Mountains batholith in north-coastal British Columbia: Constraints on age and tectonic evolution: Geological Society of America Bulletin, v. 121, p. 1341-1361.

Gordey, S.P. and Thompson, R.I., 1991, Structural styles, Chapter 17, In: Gabrielse, H. and Yorath, C.J. (Eds.), Geology of the Cordilleran Orogen in Canada: Geological Survey of Canada, Geology of Canada, n. 4, p. 625-630.

Gordey, S.P. and Anderson, R.G., 1993, Evolution of the northern Cordilleran miogeocline, Nahanni map area (105I), Yukon and Northwest Territories: Geological Survey of Canada, Memoir, v. 428, 214 p.

Gordy, P.L., Frey, F.R. and Norris, D.K., 1977, Geological guide for the Canadian Society of Petroleum Geologists 1977 Waterton-Glacier Park Field Conference: Canadian Society of Petroleum Geologists, Calgary, AB, 93 p.

Hansen, V.L, 1990, Yukon-Tanana terrane: A partial acquittal: Geology, v. 18, p. 365-369.

Jones, P.B., 1996, Triangle zone geometry, terminology and kinematics: Bulletin of Canadian Petroleum Geology, v. 44, p. 139-152.

Kingston, S., Mortensen, J., Dumala, M., and Gabites, J., 2009, Ar-Ar geochronology and Pb isotopic constraints on the origin of the Rau gold-rich carbonate replacement deposit, central Yukon, In: MacFarlane, K.E., Weston, L.H. and Blackburn, L.R. (Eds.), Yukon Exploration and Geology 2009, Yukon Geological Survey, p. 213-222.

Kuiper, Y.D., 2012, Structural setting of the Osiris, Isis and Isis East zones of the Rackla Gold Belt, east-central Yukon: Prepared for ATAC Resources, Internal Report, 17 p.

Lund, K., Aleinikoff, J.N., Evans, K.V. and Fanning, C.M., 2003, SHRIMP U-Pb geochronology of Neoproterozoic Windermere Supergroup, central Idaho: Implications for rifting of western Laurentia and synchroneity of Sturtian glacial deposits: Geological Society of America Bulletin, v. 115, p. 349-372.

MacDonald, F.A., Schmitz, M.D., Crowley, J.L., Roots, C.F., Jones, D.S., Maloof, A.C., Strauss, J.V., Cohen, P.A., Johnston, D.T. and Schrag, D.P., 2010, Calibrating the Cryogenian: Science, v. 327, p. 1241-1243.

MacDonald, F.A., Halverson, G.P., Strauss, J.V., Smith, E.F., Cox, G., Sperling, E.A. and Roots, C.F., 2012, Early Neoproterozoic basin formation in Yukon, Canada: Implications for the make-up and break-up of Rodinia: Geoscience Canada, v. 39, p. 77-99.

MacKay, P.A., 1996, The Highwood Structure: A tectonic wedge at the foreland edge of the southern Canadian Cordillera: Bulletin of Canadian Petroleum Geology, v. 44, p. 215-232.

Mair, J.L., Hart, C.J.R. and Stephens, J.R., 2006, Deformation history of the northwestern Selwyn basin, Yukon, Canada: Implications for orogen evolution and mid-Cretaceous magmatism: Geological Society of America Bulletin, v. 118, p. 304-323.

McMechan, M.E., Thompson, R.I., Cook, D.G., Gabrielse, H. and Yorath, C.J., 1991, Part E. Foreland Belt, In: Gabrielse, H. and Yorath, C.J. (Eds.), 1991, Geology of the Cordilleran Orogen in Canada: Geological Society of America, Geology of North America Series, v. G-2, p. 571-678.

Monger, J.W.H., Price, R.A. and Tempelman-Kluit, D.J., 1982, Tectonic accretion and the origin of the two major metamorphic and tectonic welts in the Canadian Cordillera: Geology, v. 10, p. 70-75.

Monger, J.W.H. and McNicoll, V.J., 1993, New U-Pb dates from southwestern Coast belt, British Columbia, In: Radiogenic Age and Isotopic Studies, Report 7, Geological Survey of Canada, paper 93-2, p. 119-126.

Mortensen, J.K., 1982, Geological setting and tectonic significance of Mississippian felsiv metavolcanic rocks in the Pelly Mountains, southeastern Yukon Territory: Canadian Journal of Earth Sciences, v. 19, p. 8-22.

Moynihan, D., Colpron, M., Israel, S. and Abbott, G, 2014, Geology of the eastern Rackla Belt, east-central Yukon: Poster presented at 2014 Mineral Exploration Roundup, January 27, 2014.

Murphy, D.C., 1997, Geology of the McQuesten River region, northern McQuesten and Mayo map areas, Yukon Territory: Yukon Geological Survey, Bulletin, v. 6, 95 p.

Nelson, J.L. and Colpron, M., 2007, Tectonics and metallogeny of the Canadian and Alaskan Cordillera, 1.8 Ga to present, In: Goodfellow, W.D. (Ed.), Mineral Deposits of Canada: A Synthesis of Major Deposit Types, District Metallogeny, the Evolution of Geological Provinces, and Exploration Methods: Mineral Deposit Division, Geological Association of Canada, Special Publications, v. 5, p. 755-791.

Nelson, J.L., Colpron, M. and Israel, S., 2013, The cordillera of British Columbia, Yukon and Alaska: Tectonics and metallogeny, In: Colpron, M., Bissig, T., Rusk, B.G. and Thompson, J.F.H. (Eds.), Tectonics, metallogeny and discovery: The North American cordillera and similar accretionary settings: Society of Economic Geologists, Special Publication, v. 17, p. 53-109.

Norris, D.K., 1974, Structural geometry and geological history of the northern Canadian Cordillera: Proceedings of the First National Convention, Canadian Society of Exploration Geophysicists, Calgary, AB, p. 18-45.

Norris, D.K., 1997, Geology and mineral and hydrocarbon potential of northern Yukon Territory and northwestern District of Mackenzie: Geological Survey of Canada, Ottawa, ON, 401 p.

Roots, C.F., 1997, Geology of the Mayo map area, Yukon Territory, 105M: Exploration and Geological Services Division, INAC, Geoscience Bulletin, v. 7, 81 p.

Stephens, J.R., Mair, J.L., Oliver, N.H.S., Hart, C.J.R. and Baker, T., 2004, Structural and mechanical controls on intrusion-related deposits of the Tombstone Gold Belt, Yukon, Canada, with comparisons to other vein-hosted ore-deposit types: Journal of Structural Geology, v. 26, p. 1025-1041.

Stockwell, C.H., 1969, Tectonic map of Canada, prepared by Tectonic Map of Canada Committee (scale 1:5,000,000): Geological Survey of Canada.

Thorkelson, D.J., Mortensen, J.K., Davidson, G.J., Creaser, R.A., Perez, W.A., and Abbott, J.G., 2001, Mesoproterozoic intrusive breccias in Yukon, Canada: The role of hydrothermal systems in reconstructions of North America and Australia; In: The Mesoproterozoic earth–ocean system of Rodinia. Edited by J.K. Bartley and L.C. Kah. Precambrian Research Special Vol. 111, p. 31-56.

Thorkelson, D.J., Abbott, G.J., Mortensen, J.K., Creaser, R.A., Villeneuve, M.E., McNicoll, V.J. and Layer, P.W., 2005, Early and Middle Proterozoic evolution of Yukon, Canada: Canadian Journal of Earth Sciences, v. 42, p. 1045-1071.

Tucker, M.J., Hart, C.J.R. and Carne, R.C., 2013, Geology, alteration, and mineralization of the Carlin-type Conrad zone, Yukon, In: MacFarlane, K.E., Nordling, M.G. and Sack, P.J. (Eds.), Yukon Exploration and Geology 2012, Yukon Geological Survey, p. 163-178.

Turner, E.C., 2011, Stratigraphy of the Mackenzie Mountains supergroup in the Wernecke Mountains, Yukon, In: MacFarlane, K.E., Weston, L.H. and Relf, C. (Eds.), Yukon Exploration and Geology 2010, Yukon Geological Survey, p. 207-231.

Woodward, N.B., 1985, Valley and ridge thrust belt: Balanced cross-sections, Pennsylvania to Alabama, Appalachian Basin Industrial Associates: University of Tennessee, Studies in Geology, v. 12, 64 p.

Zapata, T.R. and Allmendinger, R.W., 1996, Thrust-front zone of the Precordillera, Argentina: A thick-skinned triangle zone: American Association of Petroleum Geologists Bulletin, v. 80, p. 359-381.

CHAPTER 3
CONRAD ZONE GEOCHEMISTRY

3.1 Introduction

The purpose for conducting a geochemical study of the Conrad zone was to test whether the overall geochemistry of the zone is consistent with Tucker et al.'s (2013) assertion that the zone is a 'Carlin-type deposit' similar to other prolific sedimentary rock-hosted Au deposits in Nevada, USA. The most common ore fluid alteration signature in Carlin-type deposits is decalcification (Cline et al., 2005). If the Conrad zone was indeed a Carlin-type deposit, areas enriched in Au should be Ca-depleted. In some Carlin-type deposits, ferroan dolomite, an Mg-bearing carbonate mineral that often contains appreciable amounts of Fe, was an important constituent of the host rocks that facilitated sulfidation of Au (Twin Creeks, Stenger et al., 1998; Meikle, Emsbo, 1999; Deep Star, Heitt et al., 2003). For these reasons, the average geochemical concentrations of Au, Ca, and Mg were plotted on plan view maps at six different depths within the Conrad zone with the intention of highlighting differences in the spatial distribution of each element's concentration relative to one another.

The presence and availability of Fe has been shown to be fundamental to the deposition of Au in Carlin-type deposits in Nevada (Cline et al., 2005). Through sulfidation, S present in the ore fluid bonds with pre-ore Fe present in the host rocks to form new pyrite (FeS_2) grains or overgrowths on pre-ore stage pyrite. Because Au is bonded with S in the ore fluid, the sulfidation process destabilizes Au, facilitating submicron Au mineralization on pyrite rims. Therefore, the amount of available Fe is often thought to control the degree of sulfidation, and therefore the amount of potential Au. For this reason, correlations between Au and Fe were evaluated to determine if a trend existed that may suggest an association between Au and pyrite.

Several lithogeochemical studies have been conducted on Carlin-type districts in Nevada (Jerritt Canyon, Hofstra, 1994; Twin Creeks, Stenger et al., 1998; Getchell, Cail and Cline, 2001; Gold Bar, Yigit et al., 2003; Meikle, Emsbo et al., 2003; Screamer, Kesler et al., 2003). These studies show a fairly common flux of elements where certain elements are added to the rock and others are removed. The districts in Nevada consistently show enrichments in S, As, Au, Sb, Hg, and Tl, and can display enrichments in Te, Cu, Pb, Mo, Zn, Mn, Bi, Ni, W, Ag, Se, Fe, Ag, Si, Ba, Cs, Zn and Co (Emsbo et al., 2003; Cline et al., 2005). Elements that are consistently depleted include C, Ca, Mg, Sr, Mn, Na, and Sc (Cline et al., 2005). To test whether similar trends occur in the eastern Nadaleen Trend, concentrations of each element were evaluated against Au.

3.2 Methods

Geochemical concentrations of Ag, Al, As, Au, Ba, Be, Bi, Ca, Cd, Ce, Co, Cr, Cs, Cu, Fe, Ga, Ge, Hf, Hg, In, K, La, Li, Mg, Mn, Mo, Na, Nb, Ni, P, Pb, Rb, Re, S, Sb, Sc, Se, Sn, Sr, Ta, Te, Th, Ti, Tl, U, V, Zn, and Zr were measured in one- to six-meter sample intervals in 99 drill holes totaling 38.7 km of drill core in the Conrad Au zone. Assays were conducted by ALS Minerals in Whitehorse, YT or North Vancouver, BC or by SGS Mineral Services in Burnaby, BC. Each sample was crushed and pulverized to a 75 micron grain size, dissolved in aqua regia, and analyzed for the 48 elements listed above using Inductively Coupled Plasma Mass Spectrometry or Atomic Emission Spectroscopy.

Assay results were averaged over 100 m true vertical depth intervals through the deposit and plotted as contours (Ca, Mg) and grade shells (Au) on plan view maps in the same manner as the stratigraphy/structure maps (Fig. 2.4). The interval's length and corresponding averaged Au, Ca, and Mg concentrations are presented in Appendix F. Plan view maps were created and stacked in Adobe Illustrator CS5.

All elemental concentrations measured, over 13,000 samples, were plotted against Au in Excel. The data includes all rock types, altered or mineralized rocks as well as barren host rocks. Correlations were considered statistically meaningful if their R^2 value was greater than 0.1 while other correlations were determined by visually recognizing a correlative pattern. Au vs S/Fe was plotted to attempt to identify a correlation between pyrite and Au.

3.3 Results

Au is generally concentrated near the stratigraphic contact between the Conrad limestone and the Conrad siliciclastic rocks (Fig. 3.1; 200 – 700 m) as well as in a lineament oriented sub-parallel and adjacent to the Nadaleen Fault zone (Fig. 3.1; 200 – 400 m). Au occurs throughout the limestone at 100 – 200 m, where high-grade pods form linear trends oriented sub-parallel to the Nadaleen Fault zone and to geologic contacts. At the lowest levels (Fig. 3.1; 500 – 700 m), Au is concentrated in the southernmost point in the Conrad limestone. The right-lateral Conrad Fault offsets all geochemical concentrations.

Ca depletions show weak and variable trends throughout the Conrad limestone (Fig. 3.1). Intermediate to very low Ca concentrations occur nearly throughout the highest level (Fig. 3.1; 100 – 200 m); below this, intermediate to very low Ca is generally confined to the southernmost point in the Conrad limestone (Fig. 3.1; 200 – 500 m). Low Ca in the 500 – 600 m level (Fig. 4.1) occurs adjacent to the Nadaleen Fault zone. At the 600 – 700 m level (Fig. 3.1), low and intermediate Ca is confined to an N-trending zone that stretches from the Nadaleen Fault zone to the Conrad siliciclastic rocks.

Similar to Ca, Mg shows an uneven distribution throughout the Conrad limestone (Fig. 3.1B: right). Higher Mg more commonly occurs in the northwest. At the lowest level, a north-trending lineament of high and high-intermediate Mg occurs in a similar location to very low and low Ca.

Because the plan view maps average the geology and geochemical concentrations over 100 m vertical intervals, it is difficult to draw a clear spatial correlation between low Ca and/or high Mg and Au concentrations; however, plots show negative correlations between Au-bearing samples and Ca and Mg (Fig. 3.2). Na concentrations also show negative correlations (Fig. 3.2). Au statistically shows positive correlations with Tl, Hg, and Sb while S, As, Pb, Li, Cd, Cu, Zn, Te, Bi, Ni, and Ba show visually recognizable positive correlations (Figs. 3.3, 3.4). No visible correlation existed between Au and the other measured elements mentioned in the methods section above. The Au against S/Fe plot (Fig. 3.5) shows Au concentration relative to the weight percent of S divided by the weight percent of Fe for all samples. The plot suggests that the majority of Au-bearing samples are associated with an S/Fe concentration near 1.15. For reference, the S/Fe value of pure pyrite is 1.14.

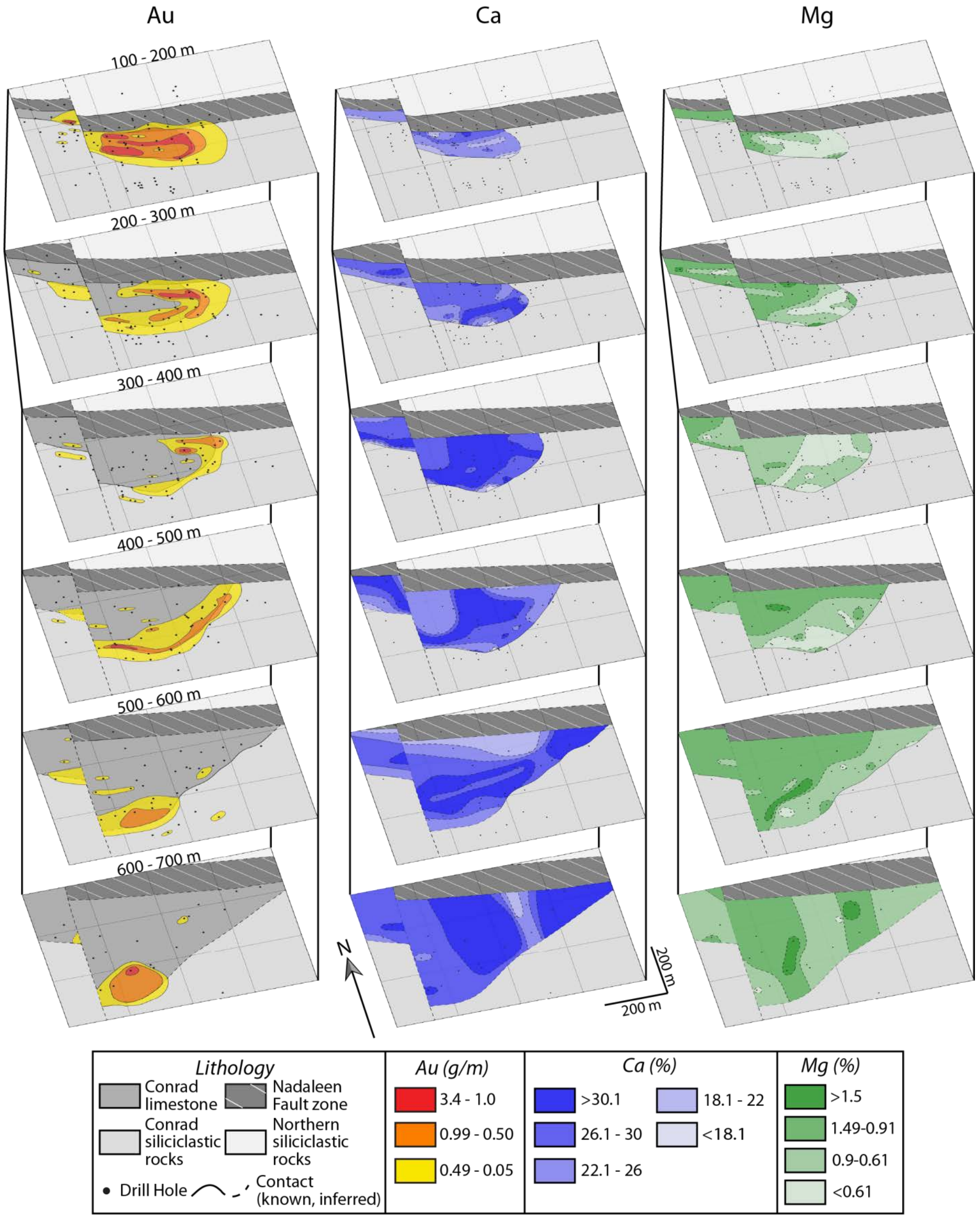

Figure 3.1: Map stacks showing contour intervals for Au, Ca, and Mg. Drill hole pierce points plot on each map as dots. Rocks with less than 0.05 g/m Au were considered barren and are not colored. For reference, pure calcium carbonate is composed of ~40% Ca. The top two maps are larger to show the westernmost drill hole (OS-12-192).

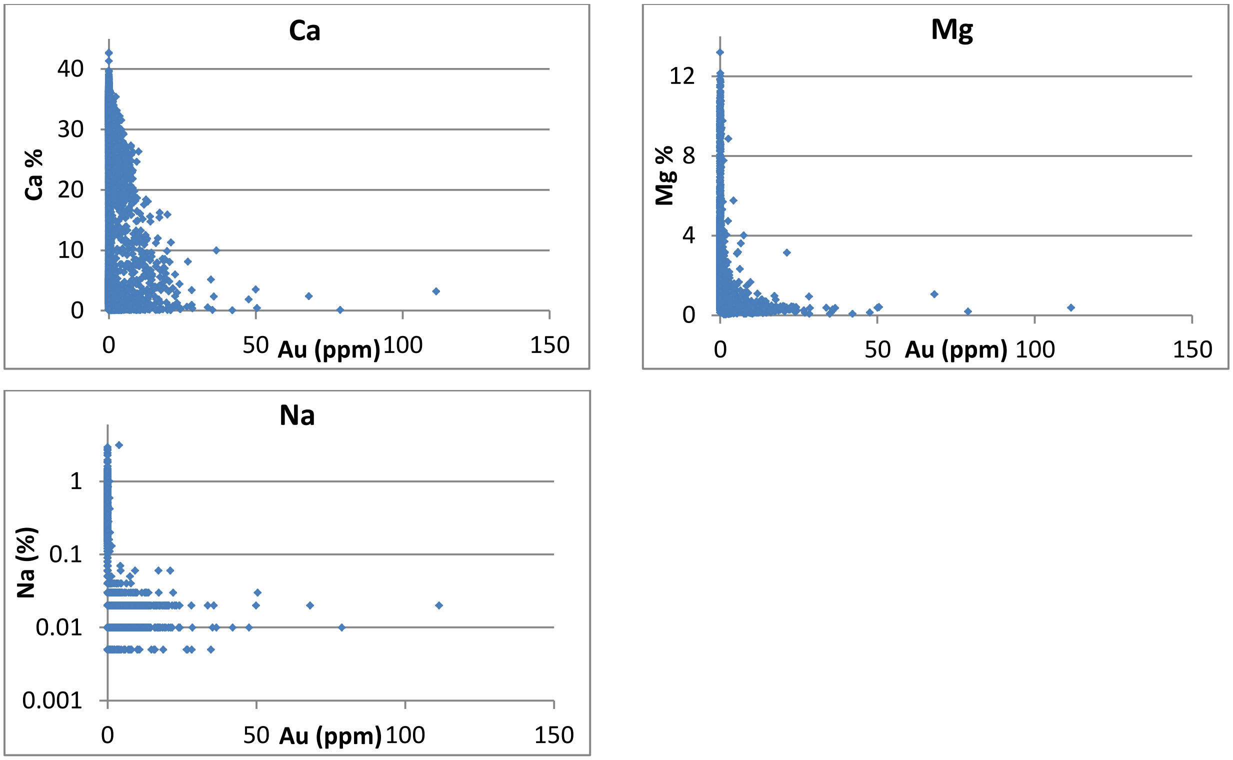

Figure 3.2: Negative element correlation plots. Ca, Mg, and Na are negatively correlated with Au.

3.4 Discussion

Mapped Au content (Fig. 3.1) shows that at deep levels in the Conrad zone (500 – 700 m), Au is generally confined to the southernmost point in the Conrad limestone where geologic contacts indicate a SSW-plunging fold. This fold is interpreted as the steeply SSW-plunging Conrad anticline (Fig. 2.6). This may reflect a structural control on ore fluid, where Au-bearing fluid channeled upwards along the hinge zone of the Conrad anticline and were confined to the limestone by the lower permeability overlying Conrad siliciclastic rocks. Above this, plan view maps (300 – 500 m) show that Au largely occurs along the stratigraphic contact between the Conrad limestone and the Conrad siliciclastic rocks. Where geologic contacts suggest the presence of an ESE-plunging fold (200 – 300 m), Au may outline two distinct limbs of the fold although structural data did not define a fold (Fig. 2.4). The upper map (100 – 200 m) is defined by the most high-grade Au as well as intermediate to low Ca values (Fig. 3.1). Fluid upwelling may have been baffled here by the juxtaposition of the N-dipping Nadaleen Fault zone and the Conrad siliciclastic rocks that effectively formed a ‘trap’ for ore fluid (Fig. 3.6). If true, this trap

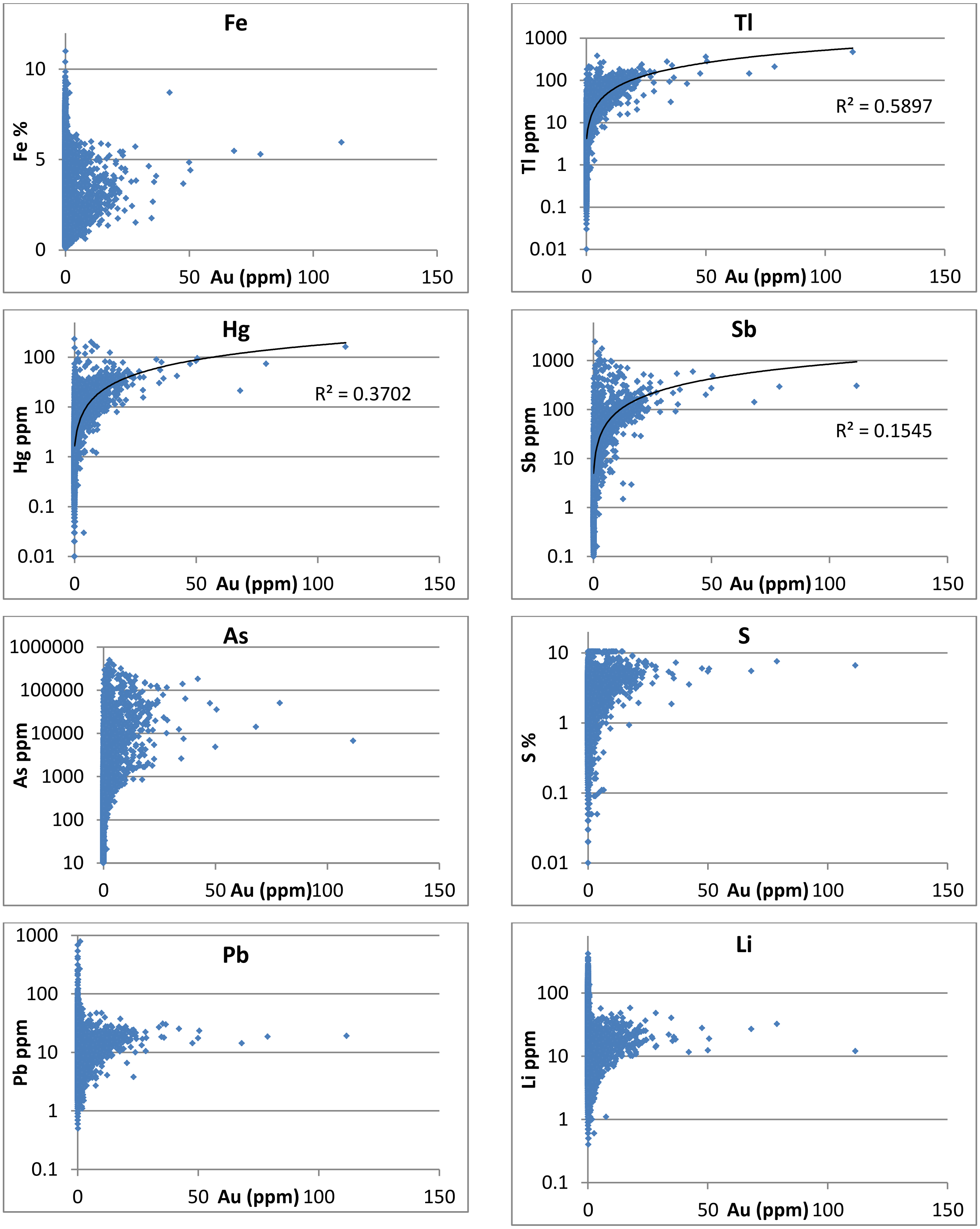

Figure 3.3: Positive element correlation plots. Trend lines were drawn through correlations with an R^2 value greater than 0.1. Plots without trend lines have visibly recognizable trends.

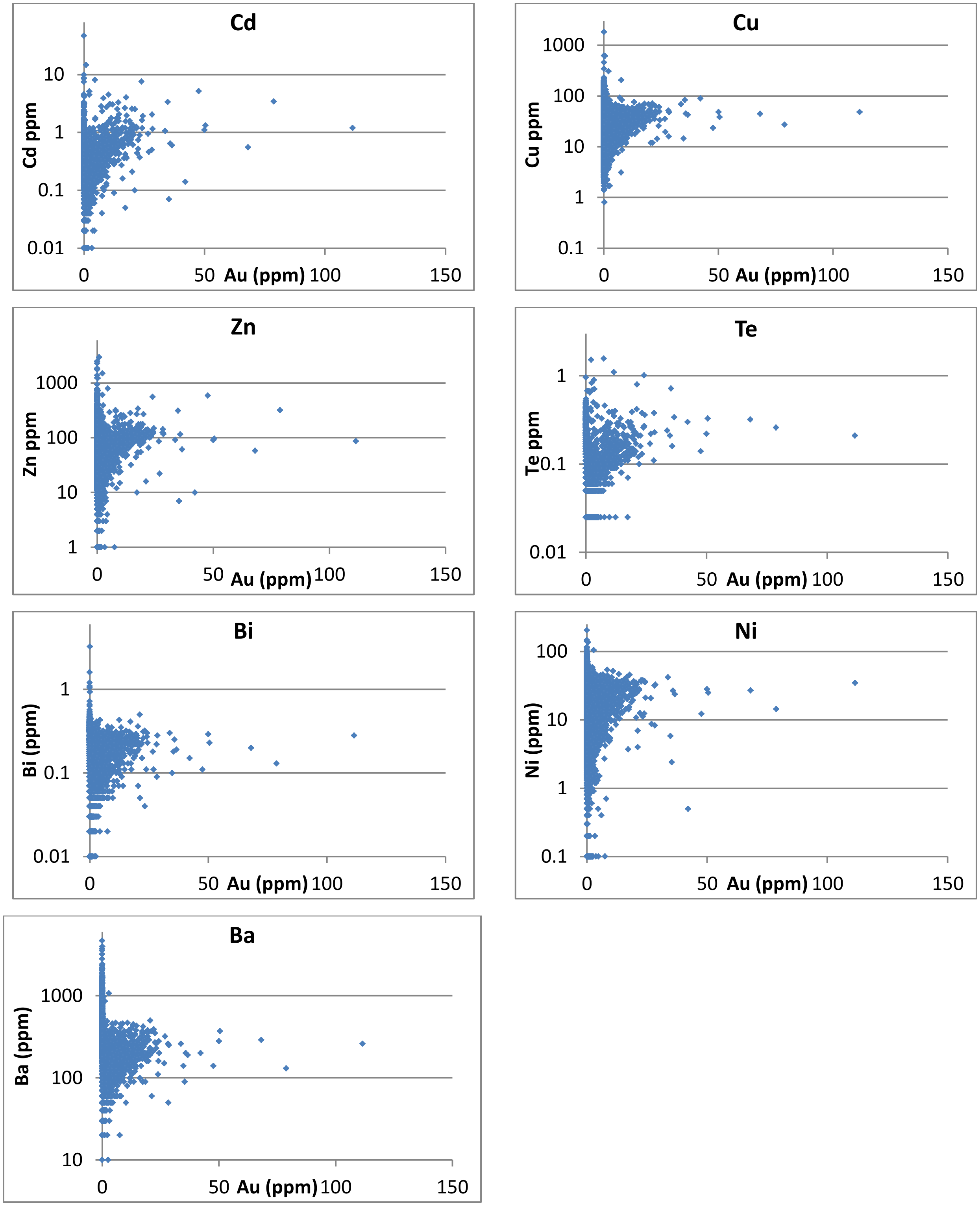

Figure 3.4: Plots showing visibly recognizable element correlations derived from all assay results including those from limestone or siliciclastic rocks that may be altered or mineralized.

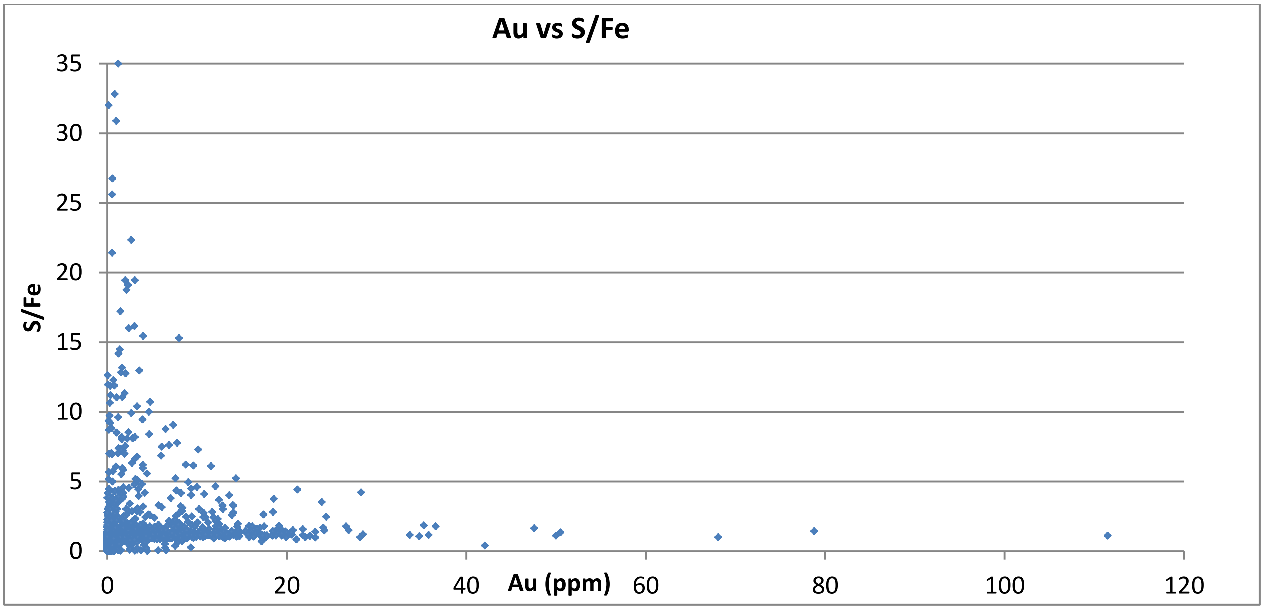

Figure 3.5: Plot showing Au vs S/Fe.

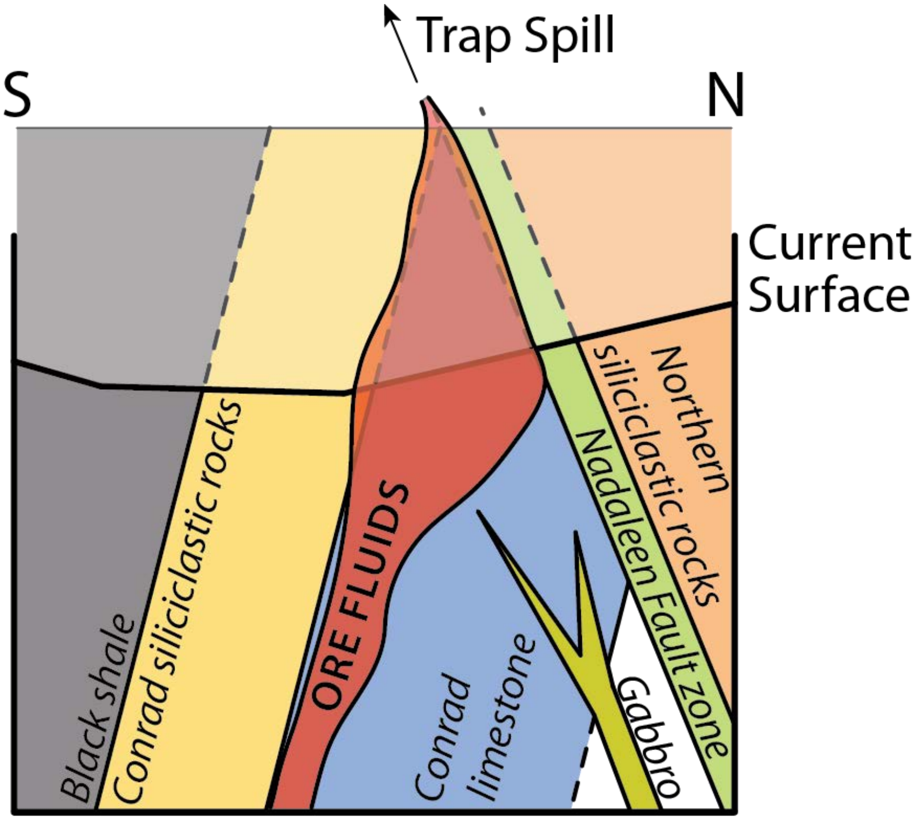

Figure 3.6: N-S oriented cross section across the Conrad zone showing the interpreted fluid migration pathway through the rocks. The juxtaposition of the Nadaleen Fault zone and the Conrad siliciclastic rocks may have formed a structural 'trap' that baffled the ascent of ore fluid. Cross section location interpreted 100 m east of the Conrad Fault.

likely slowed the ascent of ore fluid, resulting in increased interaction between Au-bearing ore fluid and the primary carbonate host rock.

A spatial association between Au, Ca, and Mg concentrations is not clear from the plan view map stacks (Fig. 3.1). However, the method is likely problematic because it involves averaging concentrations of barren, altered, and mineralized rocks over 100 m intervals in a system that is more often defined by discrete mineralized zones rather than large bodies. The element plots (Figs. 3.3, 3.4) do show clear correlations between some elements and Au. For example, Au-bearing samples are typically associated with relatively low Ca and Mg (Fig. 3.2) which suggests an association between decalcification and Au. Au is also typically associated with an increase in Fe (Fig. 3.3), suggesting that either Fe is brought in with the mineralizing fluid or pre-ore Fe present in the host rocks facilitates Au mineralization. The majority of Au-bearing samples have an S/Fe ratio that clusters around 1.15 (Fig. 3.5), suggesting that in the mineralizing system, Au deposition was related to pyrite. Samples that have S/Fe ratios >1.15 probably contain variable amounts of realgar (As_4S_4) or orpiment (As_2S_3), minerals commonly seen in hand sample.

The Conrad zone shows visually recognizable or statistical correlations between Au and all the elements commonly associated with Au in a typical Carlin-type deposit in Nevada (Table 3.1). In addition, correlations can be drawn for many of the less commonly occurring elements in Carlin-type deposits in Nevada, except Mo, Mn, W, Ag, Co, Se, and Cs (Table 3.1). In contrast with Carlin-type deposits in Nevada, Li and Cd are visually correlative with Au in the Conrad zone (Table 3.1).

The spatially plotted element concentration maps and the element correlation plots show that the overall geochemistry of the Conrad zone is similar to the geochemistry of Carlin-type deposits in Nevada. Furthermore, an important relationship exists between the presence of Au and an S/Fe values near 1.15 suggesting a relationship between Au and pyrite. This may suggest that sulfidation of Fe facilitated deposition of Au.

Table 3.1: Enriched and depleted elements common to Carlin-type deposits in Nevada, USA (Cline et al., 2005) and enrichments and depletions in the Conrad zone. A double-dash (--) indicates that enrichment is not typical (Carlin-type deposits) or is not seen (Conrad zone). C and Si were not measured from samples in the Conrad zone.

Carlin-type deposits, Nevada, USA	*Conrad zone, Nadaleen Trend*
Common enrichments	
S	S
Au	Au
As	As
Sb	Sb
Hg	Hg
Tl	Tl
Less common enrichments	
Te	Te
Cu	Cu
Pb	Pb
Mo	--
Zn	Zn
Mn	--
Bi	Bi
Ni	Ni
W	--
Ag	--
Co	--
Se	--
Fe	Fe
Si	N/A
Ba	Ba
Cs	--
--	Li
--	Cd
Depleted elements	
C	N/A
Ca	Ca
Mg	Mg
Sr	--
Mn	--
Na	Na
Sc	--

3.5 Conclusion

The lithogeochemistry of the Conrad zone is generally consistent with Carlin-type deposits in Nevada. Similar elements are both added to and removed from the rock by the mineralizing system.

3.6 References

Cail, T.L. and Cline, J.S., 2001, Alteration associated with gold deposition at the Getchell Carlin-type gold deposit, north-central Nevada: Economic Geology, v. 96, p. 1343-1359.

Cline, J.S., Hofstra, A.H., Muntean, J.L., Tosdal, R.M. and Hickey, K.A., 2005, Carlin-type gold deposits in Nevada: Critical geologic characteristics and viable models: Economic Geology 100th Anniversary Volume, p. 451 – 484.

Emsbo, P., 1999, Origin of the Meikle high grade gold deposit from the superposition of Late Devonian Sedex and mid-Tertiary Carlin-type gold mineralization: Unpublished Ph.D. thesis, Colorado School of Mines, Golden, CO, 394 p.

Emsbo, P., Hofstra, A.H., Lauha, E.A., Griffin, G.L. and Hutchinson, R.W., 2003, Origin of high-grade gold ore, source of ore fluid components, and genesis of the Meikle and neighboring Carlin-type deposits, northern Carlin Trend, Nevada: Economic Geology, v. 98, p. 1069 – 1105.

Heitt, D.G., Dunbar, W.W., Thompson, T.B. and Jackson, R.G., 2003, Geology and geochemistry of the Deep Star gold deposit, Carlin trend, Nevada: Economic Geology, v. 98, p. 1107 – 1135.

Hofstra, A.H., 1994, Geology and genesis of the Carlin-type gold deposits in the Jerritt Canyon district, Nevada: Unpublished Ph.D. thesis, Boulder, CO, University of Colorado, 719 p.

Kesler, S.E., Fortuna, J., Ye, Z., Alt, J.C., Core, Dp.P., Zohar, P., Borhauer, J. and Chryssoulis, S.L., 2003, Evaluation of the role of sulfidation in deposition of gold, Screamer section of the Betze-Post Carlin-type deposit, Nevada: Economic Geology, v. 98, p. 1137-1157.

Stenger, D.P., Kesler, S.E., Peltonen, D.R. and Tapper, C.J., 1998, Deposition of gold in Carlin-type deposits: The role of sulfidation and decarbonation at Twin Creeks, Nevada: Economic Geology, v. 93, p. 201 – 215.

Tucker, M.J., Hart, C.J.R. and Carne, R.C., 2013, Geology, alteration, and mineralization of the Carlin-type Conrad zone, Yukon, In: MacFarlane, K.E., Nordling, M.G. and Sack, P.J. (Eds.), Yukon Exploration and Geology 2012, Yukon Geological Survey, p. 163-178.

Yigit, O., Nelson, E.P., Hitzman, M.W. and Hofstra, A.H., 2003, Structural controls on Carlin-type gold mineralization in the Gold Bar district, Eureka County, Nevada: Economic Geology, v. 98, p. 1173-1188.

CHAPTER 4

CONCLUSION

4.1 Structural geology

Observed structures within a 6 km^2 area at the eastern Nadaleen Trend are complex and have not been recognized elsewhere within northeastern Yukon Territory. Structures include S- to SSW-plunging anticlines, E-, WSW-, and SE-plunging folds, the E-trending dextral strike-slip Osiris Fault, the NNE-dipping Nadaleen Fault zone, and the N-trending dextral strike-slip Conrad Fault. Deformed rocks are interpreted to have resulted from NNE-SSW directed shortening (D_1), NW-SE directed shortening and dextral simple shear (D_2), N-S directed shortening (D_3) and minor N-trending dextral strike-slip (D_4). The outlined deformation sequence may result from regional structures and/or competency contrasts between rock units.

The Nadaleen Trend is situated in an east-trending triangle zone that does not exist to the west or the east. Rocks to the west show multiple NNE-vergent structures in the south and only one fold in the north indicating that strain decreases northwards. Rocks to the east of the triangle zone are consistently NNE-vergent. The unique structural style of rocks at and west of the eastern Nadaleen Trend suggest they were influenced by an obstruction, perhaps a subsurface structure, such as the Rackla Fault. The structure is interpreted to have obstructed fold-thrust transport west of the eastern Nadaleen Trend, and presented a minor obstruction at the eastern Nadaleen Trend that resulted in the formation of a triangle zone. Unobstructed movement occurred in the east. Along the interpreted interface between the unobstructed and obstructed zones, a zone of NE-trending folds and faults exist. Their oblique orientation may result from a generally NNE-trending, sinistral strike-slip zone that formed where unobstructed rocks translated NE-ward against obstructed rocks.

The eastern Nadaleen Trend triangle zone is interpreted to have acted as a regional-scale structural funnel that channeled Au-rich ore fluid into the eastern Nadaleen Trend. Oppositely verging reverse faults that bound the triangle zone may have formed a regional aquitard to ascending ore fluids. Au in the center of the triangle zone is further concentrated in local, steeply

S- to SSW-plunging anticlines, suggesting these may have been effective fluid conduits for upwelling ore fluids.

4.2 Conrad zone geochemistry

The geochemistry of the Conrad zone shows that Au commonly occurs in rocks that are also depleted in Ca and Mg, suggesting an association between Au mineralization and decalcification. Au-bearing samples show similar element enrichments as Carlin-type deposits in Nevada and elemental concentrations suggest an association between Au and pyrite. These findings suggest that the Conrad Au zone is geochemically similar to Carlin-type deposits in Nevada.

APPENDIX A
STRUCTURAL METHODS

A-1 Oriented drill core

ATAC Resources drilled 99 holes totaling 38.7 km of drill core in the Conrad Zone during the 2011 and 2012 field seasons. In 2012, oriented drill core was collected using the Reflex Act II RD Digital Core Orientation Tool. The data was measured from the drill core using 2iC Australia's Ezy-Logger Quick Reference Goniometer. A goniometer is used to measure two angles (Fig. A-1): alpha, the angle between the core axis and the plane of interest, and beta, the angle between the bottom mark and the downhole side of the plane of interest (Holcombe et al., 2009). To convert alpha and beta to actual orientations of planar structures, GeoCalculator (Holcombe et al., 2013) was originally used, followed later by a version of Stanley and Hooper's (2003) "Planes from Oriented and Navigated Drillcore" Excel spreadsheet.

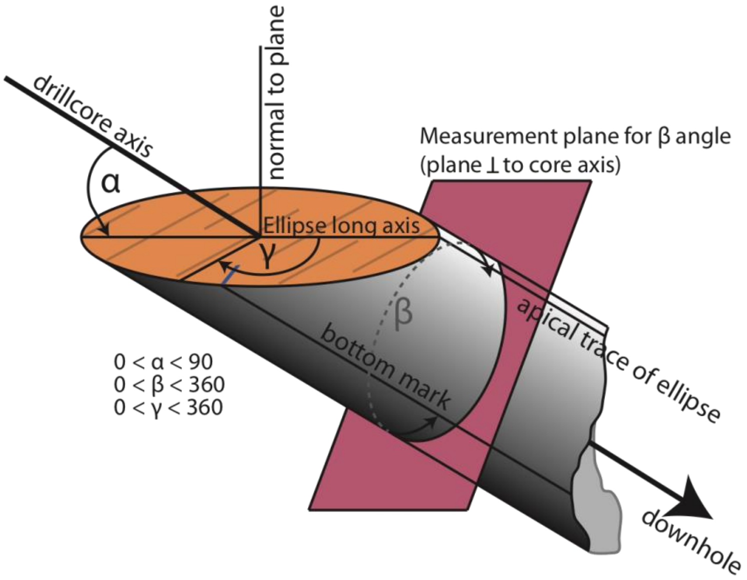

Figure A-1: Schematic diagram defining α, β and γ from drill core (modified from Holcombe Coughlin and Associates, 2008-9).

OSXStereonet was used to calculate averages for bedding and fold axis orientations using the Fisher Vector Distribution (Fisher, 1953) and Cylindrical Best Fit tools (Cardozo and Allmendinger, 2011).

A-2 Surface mapping

Surface mapping of the Conrad Zone was completed at 1:1500 scale using a Brunton compass and a Garmin eTrex Vista HCx handheld GPS. Mapping involved measuring planar and linear structural features as well as spatially defining rock units relative to one another. Planar structures were measured using right-hand-rule and are given as strike/dip (XXX°/YY°). Linear structures are referred to as plunge→trend (YY°→XXX°). Field maps were scanned and digitized using Adobe Illustrator CS 5. Structural data was plotted and analyzed on equal-area lower-hemisphere projections using OSXStereonet. The study area was divided into structural domains based on unique structural geology. Adobe Illustrator CS 5 was used to combine and merge the Conrad zones' rock types, stereographic projections, and structural domains with simplified results of Kuiper's (2012) mapping of the Osiris/Sunrise and Isis East zones.

Structural features measured included bedding, foliation, cleavage, axial planes, and hinge lines. Bedding is defined as a fundamental primary sedimentary structure (Davis et al., 2012) and it represents the most prominent feature in all stratigraphic units. Foliation is defined herein as any macroscopically penetrative parallel alignment of planar fabric elements in a rock resulting from post-lithification stress (Davis et al., 2012). Cleavage is a type of foliation defined as penetrative and closely spaced planar to subplanar surfaces that permit the rock to be broken into plates or slabs and tend to be associated with folds (Davis et al., 2012). Fracture and stylolitic cleavage were most common, with the former being associated with shaly/silty siliciclastic units and the latter with carbonates. The axial plane or surface refers to the imaginary surface that contains all the hinge lines of a fold (Davis et al., 2012). Hinge lines were the only linear features measured. The hinge line is defined as the maximum amplitude of a fold, or where maximum curvature in a fold takes place (Park, 1997).

A-3 Regional quadrangle map analysis

A protractor and a ruler were used to measure the trends of thrust faults and folds on geologic quadrangle maps provided by the Yukon Geological Survey (Colpron et al., 2013; Moynihan et al., 2014). The maps show the traces and axial traces of thrust faults and folds over stratigraphic domains interpreted during field mapping. They do not display dips or plunges, thus they were not a part of the study. The data were plotted and analyzed on stereographic projections using OSXStereonet and the study area was divided into domains based on unique structural geology. Adobe Illustrator CS 5 was used to merge the data projections and structural domains.

APPENDIX B
ROCK DESCRIPTIONS

Rocks of the Nadaleen Trend (Fig. B-1) are composed of three distinct stratigraphic sequences: the Nadaleen North, Conrad, and Osiris sequences (Fig. B-2). The Nadaleen North sequence is composed entirely of siliciclastic rocks and is separated from the more southern Conrad and Osiris sequences by the Nadaleen Fault (Fig. B-2). The boundary between the southward-younging Conrad and Osiris sequences is defined by a color difference between two similar fine-grained siliciclastic units: the grey shale and the overlying maroon-colored Osiris shale. The contact relationship between these two units remains contentious as it is poorly exposed and has not been intersected in drill core. The Conrad sequence is primarily composed of fine-grained siliciclastic rocks and lesser carbonate rocks and conglomerate units. The overlying Osiris package is dominated by carbonate rocks with lesser siliciclastic rocks. Gabbroic dikes (Fig. B-1, B-2) occur typically adjacent to the Nadaleen Fault.

The correlation between Nadaleen Trend units and regional stratigraphic units remains a subject of debate. Turner (2011) interpreted the Conrad stratigraphic sequence as latest Neoproterozoic – earliest Cambrian Hyland Group, the Osiris stratigraphic sequence as late Mesoproterozoic Pinguicula Group, and the Nadaleen North stratigraphic sequence as the early Mesoproterozoic Wernecke Supergroup (Fig. B-3). Bennett (2012) agreed with Turners' interpretations for the Conrad and Osiris stratigraphic sequences, but assigned the Nadaleen North package to the Windermere Supergroup (Fig. B-3). More complete regional mapping completed by YGS led Colpron et al. (2013a, 2013b) to interpret the Nadaleen North rocks as the "Upper Nadaleen" unit and the Conrad and Osiris stratigraphic sequences as the "Stenbraten" unit. These units were newly recognized stratigraphic intervals in the uppermost part of the Neoproterozoic Windermere Supergroup (Fig. B-3) (Colpron et al., 2013a, 2013b). Through further mapping, YGS recognized regionally correlative rock units that confirmed the Neoproterozoic age (Moynihan et al., 2014). The Nadaleen North stratigraphic sequence correlates with the Mesoproterozoic Ice Brook Formation (Figs. 2.2, B-3) and are the oldest rocks at the Nadaleen Trend (Moynihan et al., 2014). The Conrad stratigraphic sequence

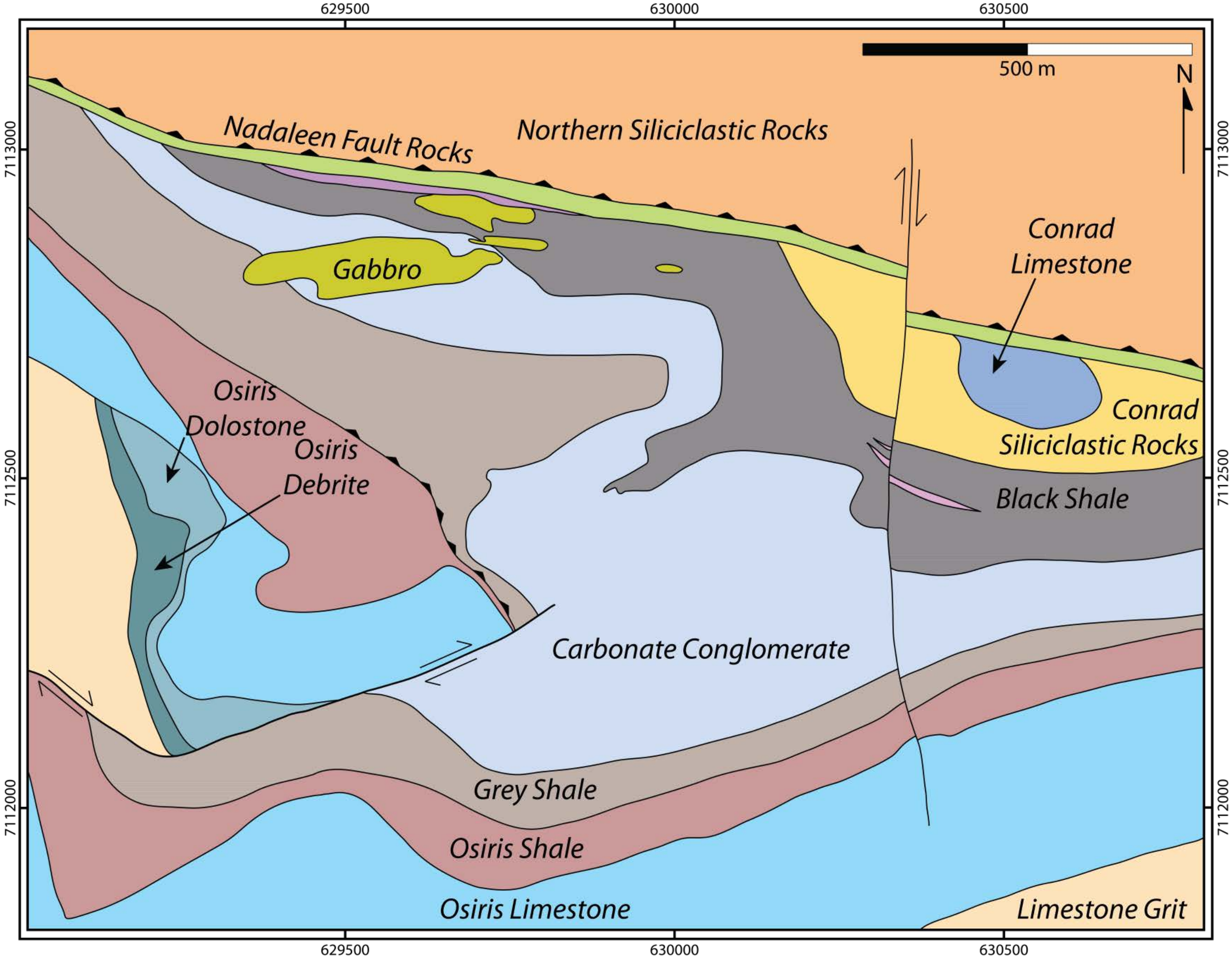

Figure B-1: Geologic map of the eastern Nadaleen Trend; labels define the descriptive names of each stratigraphic unit.

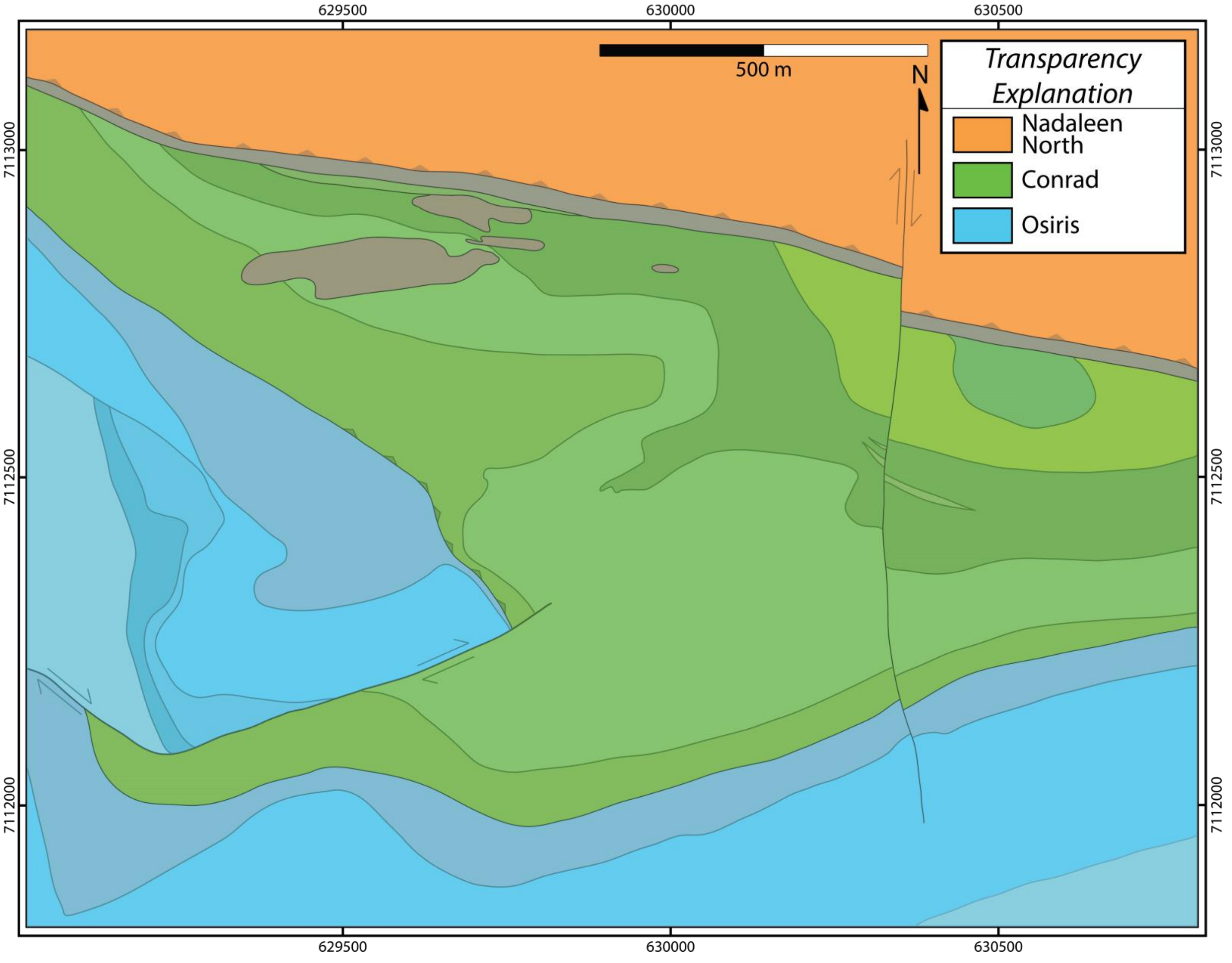

Figure B-2: Summary map depicting the distribution of the Nadaleen North, Conrad, and Osiris stratigraphic sequences in the Nadaleen Trend. Rocks that do not correspond to a stratigraphic sequence include the Nadaleen fault rocks and gabbro and are shown in grey. Underlying map as in Fig. B-1.

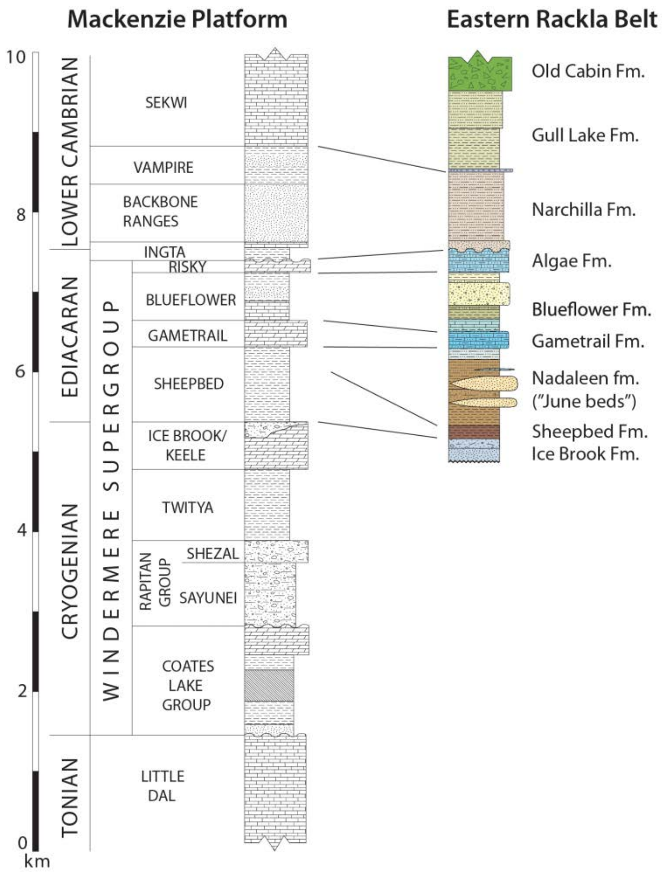

Figure B-3: Stratigraphic correlation between regionally recognized sequences and rocks of the Eastern Rackla Belt (Moynihan et al., 2014).

correlates with the undivided Nadaleen Formation (Figs. 2.2, B-3) of latest Neoproterozoic age. The Osiris stratigraphic package was separated into various rock units including the Stenbraten member of the Nadaleen formation, the Gametrail formation, and the Blueflower formation, all of which correspond to late Neoproterozoic age (Figs. 2.2, B-3) (Moynihan et al., 2014).

The purpose of this appendix is to describe the rocks of the Nadaleen Trend. The Nadaleen North, Conrad, and Osiris stratigraphic sequences will be defined by their spatial extents followed by the rock units that occur within them including photos of outcrops, hand samples, and thin sections where appropriate. If igneous and/or mineralized rocks occur within the sequences, their locations and characteristics will be described. A description of the Nadaleen fault rocks and gabbro is presented last. Stratigraphic units were not studied in thin section because this work has been completed previously (Turner, 2011; Tucker et al., 2012; Cairns, 2013).

B-1 The Nadaleen North stratigraphic sequence

The Nadaleen North stratigraphic sequence (Fig. B-2) is constrained to the south by the Nadaleen Fault and extends beyond to the limits of ATAC's property to the east, north, and west. Mineralized rocks and gabbroic dikes are absent from the package. Structures include folds, minor local faults, and intense cleavages.

B-1-1 Northern siliciclastic rocks

The Nadaleen North stratigraphic package is entirely composed of thick, intensely cleaved, tan to rusty brown weathering (Figs. B-4A, B-5) siliciclastic rocks (Fig. B-4). The lithology consists of thinly bedded mudstone to siltstone with interbedded conglomerate composed of rounded pebbles in a sandy calcareous matrix. Grains are predominantly angular to subrounded quartz. Normally graded bedding is very common. Trace pyrite is disseminated throughout the unit. Locally, maroon layers can contain up to 5% hematite and trace chalcopyrite (Tucker et al., 2013). Fresh samples are typically grey- green (Fig. B-4B) with local maroon horizons. Intense cleavage (Fig. B-4A) causes the unit to weather into chips and spread over the rock units immediately to the south. Quartz veinlets are common. Exposure of this readily weathering unit is limited to a ridge north of the ore zones of the Nadaleen Trend.

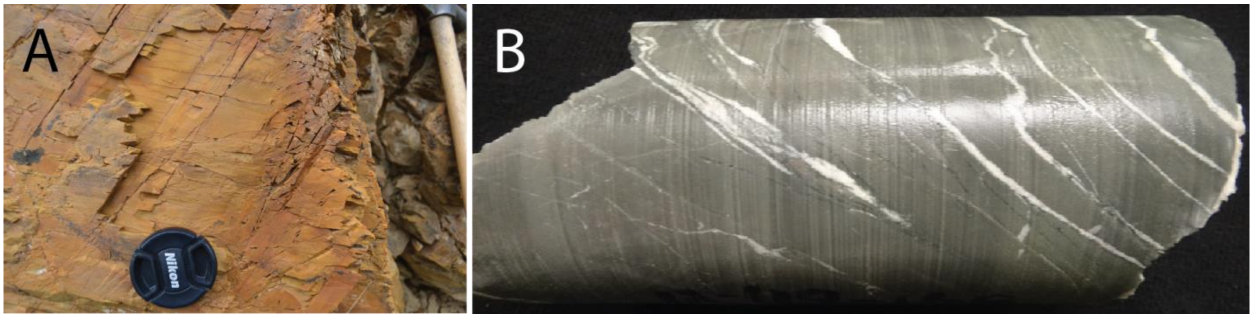

Figure B-4: Northern siliciclastic rocks. A. Outcrop photo showing distinctive cleavage with camera lens cap for scale. B. Drill core (HQ, ~6.4 cm diameter) photo with bedding parallel quartz veins.

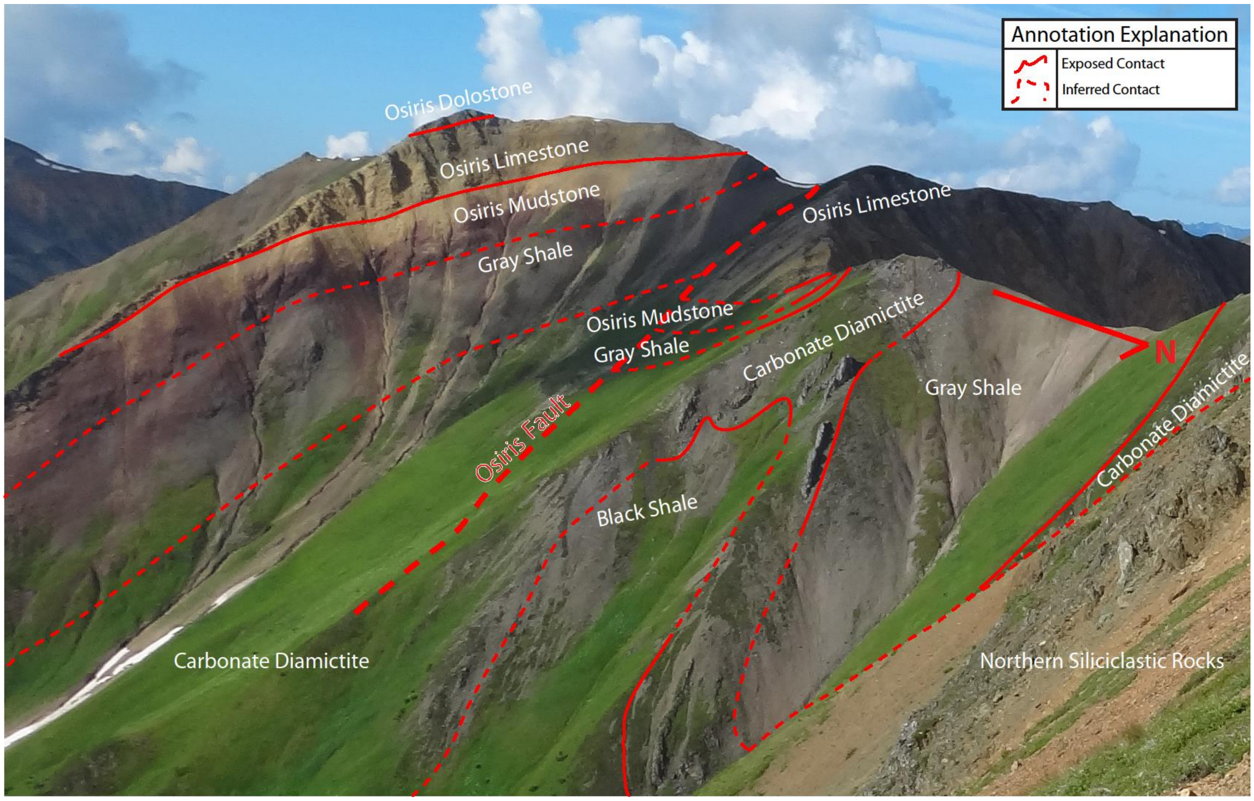

Figure B-5: Photograph of the eastern part of the eastern Nadaleen Trend. Rock units, exposed and inferred contacts, and faults are annotated. Photo taken standing on the Northern siliciclastic rocks looking toward the SW.

B-2 The Conrad stratigraphic sequence

The southward-younging Conrad stratigraphic package (Fig. B-2) is bounded to the north by the Nadaleen Fault, to the south and west by the overlying Osiris package and its eastern contact is not exposed. Au in the Conrad Zone (Fig. 2.1D) is hosted primarily in the Conrad limestone and secondarily in the Conrad siliciclastic rocks. Gabbroic dikes occur in all units proximal to the Nadaleen Fault. Complex structures include chevron folds, faults, and cleavage.

B-2-1 Conrad limestone

The Conrad limestone (Figs. B-1, B-6) consists of monotonous intervals of light- to dark-grey weathering, fine- to medium-grained to massive, weathering resistant limestone (Fig. B-

Figure B-6: Conrad limestone. A. Outcrop photo. Average bed thickness is around 4 cm. B. Drill core (NQ, ~4.8 cm diameter) photo with calcite veins oriented sub-perpendicular to bedding. C. Drill core (NQ) photo with flame structures.

6A). Fresh samples are typically dark grey (Figs. B-6B, C). Bedding is characterized by 2-6 cm thin laminations (Fig. B-6A) that separate massive beds devoid of sedimentary structures. The composition is primarily calcite (60-95%) with minor silt and quartz (5-30%) (Tucker et al., 2013). Characteristic "beef" and "cone-in-cone" calcite occur near the overlying Conrad siliciclastic rocks possibly due to an increase of quartz and silt content (Tucker et al., 2013). Calcite veins occur throughout the unit at all angles and range from moderate to very strong intensity. Stylolites are common and are typically bedding parallel, although they occur at high angles as well and typically contain residual quartz grains and framboidal pyrite (Tucker et al., 2013). Calcite proximal to stylolites is often recrystallized (Tucker et al., 2013).

B-2-2 Conrad siliciclastic rocks

The Conrad siliciclastic rocks (Figs. B-1, B-7) are in gradational conformable contact with the Conrad limestone. They consist primarily of shale to siltstone composed of subrounded

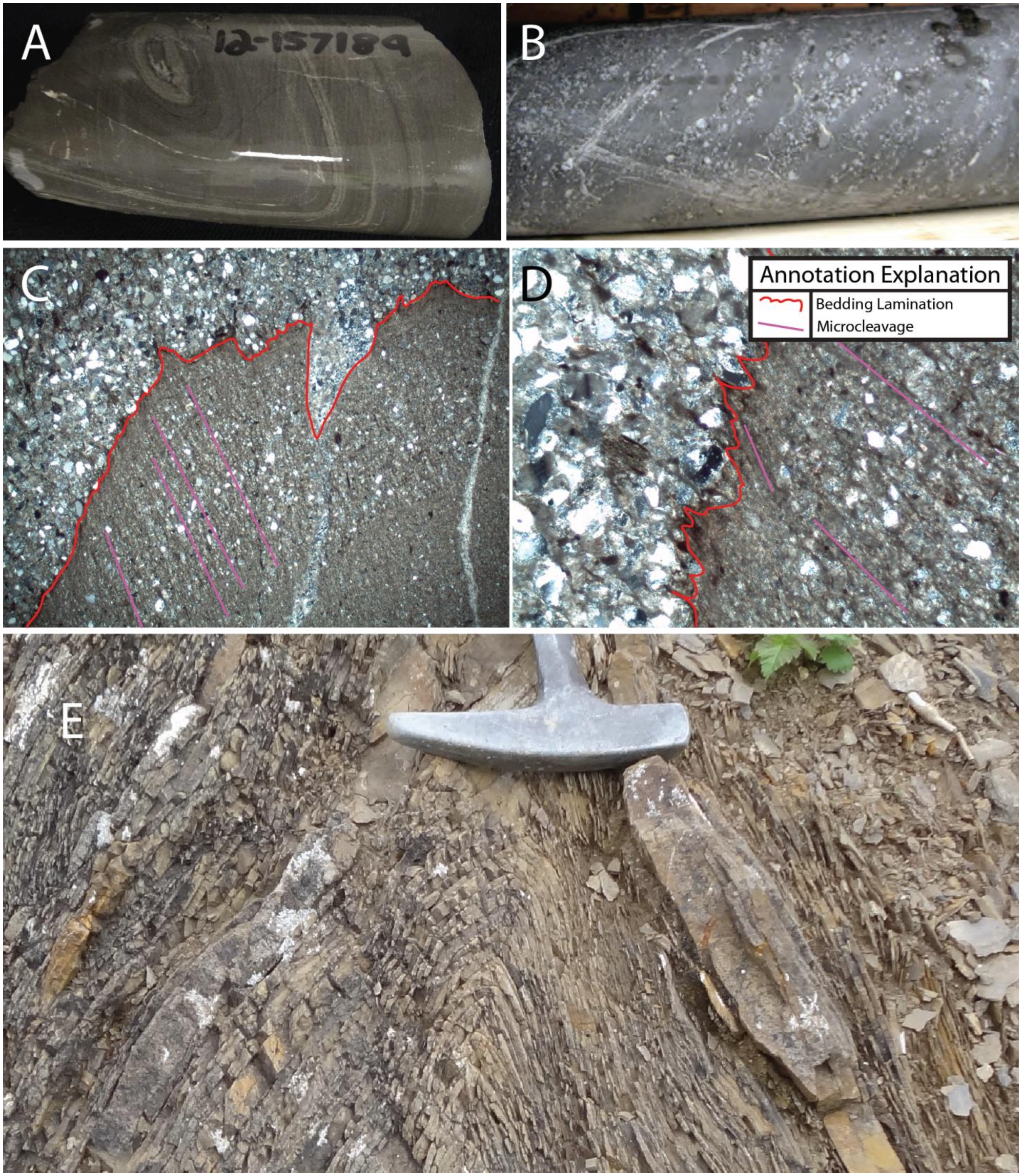

Figure B-7: Conrad siliciclastic rocks A. Drill core (NQ) photo of pyritic siltstone in the Conrad siliciclastic rocks. Lighter layers are dominantly composed of pyrite. B. Drill core (NQ) photo of quartz pebble conglomerate in the Conrad siliciclastic rocks. C. Thin section photo of microscopic axial planar cleavage in a fold hinge. Photo taken at B-5X magnification. D. Thin section photo of microscopic axial planar cleavage. Photo taken at 10X magnification. E. Outcrop photo of closed chevron folds. Hammer head for scale.

quartz grains (80-95%) (Tucker et al., 2013). Well-defined bedding laminations are regularly 0.5-1 cm thick (Figs. B-7A, B). Lenses of matrix-supported quartz-pebble conglomerate are common. Clasts in the conglomerate are typically quartz, chert, carbonate and siltstone and the matrix is primarily silt with trace carbonate. Pyrite is disseminated throughout the unit (2-6%) and also occurs as massive (>60%) layers (Fig. B-7A) (Tucker et al., 2013). Weak axial planar cleavage occurs in fold hinges throughout the unit (Fig. B-7C, D). Dolomite, calcite, and quartz veinlets occur rarely throughout. Unoxidized samples are typically black. Exposure of this recessively weathering unit is very poor and is limited to a rusty-brown (Fig. B-7E), non-vegetated ridge southwest of the Conrad limestone outcrops.

B-2-3 Black shale

The black shale unit (Figs. B-1, B-5, B-8) is in gradational conformable contact with the Conrad siliciclastic rocks and consists of shale to siltstone. Fresh core samples are characterized

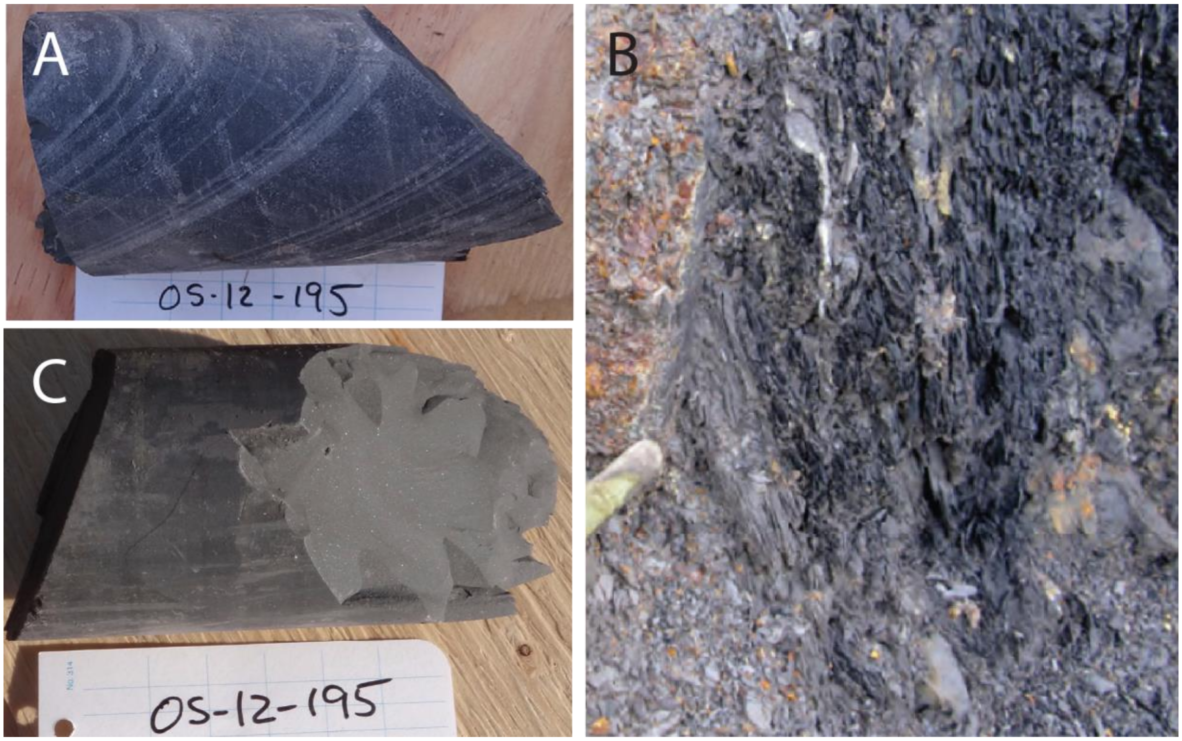

Figure B-8: Black shale. A. Hand sample photo with thin grey laminations. Each column on description sheet is 1 cm wide. B. Outcrop photo. Finger for scale. C. Hand sample photo showing characteristic flecks of mica. Columns on description sheet are 1 cm wide.

by cm- to mm-scale black (75%) and grey (25%) bedding laminations (Fig. B-8A). Exposure of the recessively weathering unit is limited to a few black outcrops (Fig. B-8B). Flecks of mica are typical (Fig. B-8C). Lenticular carbonate pods occur randomly within the unit in two locations: a hydrothermal dolostone (Tucker et al., 2013) SW of the Conrad Zone and a limestone on a N-S oriented ridge west of the Conrad Zone between a large gabbro outcrop and the Nadaleen Fault zone (Fig. B-1). Unoxidized samples of the hydrothermal dolostone are beige-grey and are composed of 80-90% finely crystalline dolomite, 5-10% pyrite, and trace sphalerite (Tucker et al., 2013). Distinctive black crackle breccia occurs throughout the dolostone.

B-2-4 Carbonate conglomerate

The carbonate conglomerate unit (Figs. B-3, B-5, B-9) is in sharp conformable contact with the black shale. Its exposures on steep ridges and vertical fins on slopes act as important markerhorizons (Fig. B-5) throughout the Conrad stratigraphic sequence. The unit consists of megaclastic carbonate conglomerate and is typically irregularly shaped, highly resistant, and tan- to buff- to grey-colored (Fig. B-9A, B). Graded bedding in the primary conglomerate is inconspicuous. Individual beds grade upwards into fining upward sequences of centimeter to millimeter-scale calcarenite composed of angular to rounded carbonate and quartz grains with distinctive ripple and cross-laminations (Fig. B-9C). Clast size varies from mm-scale to over 3 m in diameter and clasts are composed of micrite, dolomudstone, and rarely conglomerate. The matrix varies between 15% and 50% and is composed of micrite, calcareous and non-calcareous quartz siltstone, and calcareous quartz sandstone (Turner, 2011). Bedding-perpendicular, diagenetic “beef” calcite (Fig. B-9D) features are common. Lenses of interbedded shale occur at the base and top of the unit.

B-2-5 Grey shale

The grey shale unit (Figs. B-1, B-5, B-10) lies in interbedded gradational and conformable contact with the carbonate diamictite unit. Thin laminations are present throughout the unit and minor 1-2 mm subrounded quartz grains are seen locally. The grey-weathering unit is light grey to black on fresh surfaces (Fig. B-10) and typically contains visible flecks of mica.

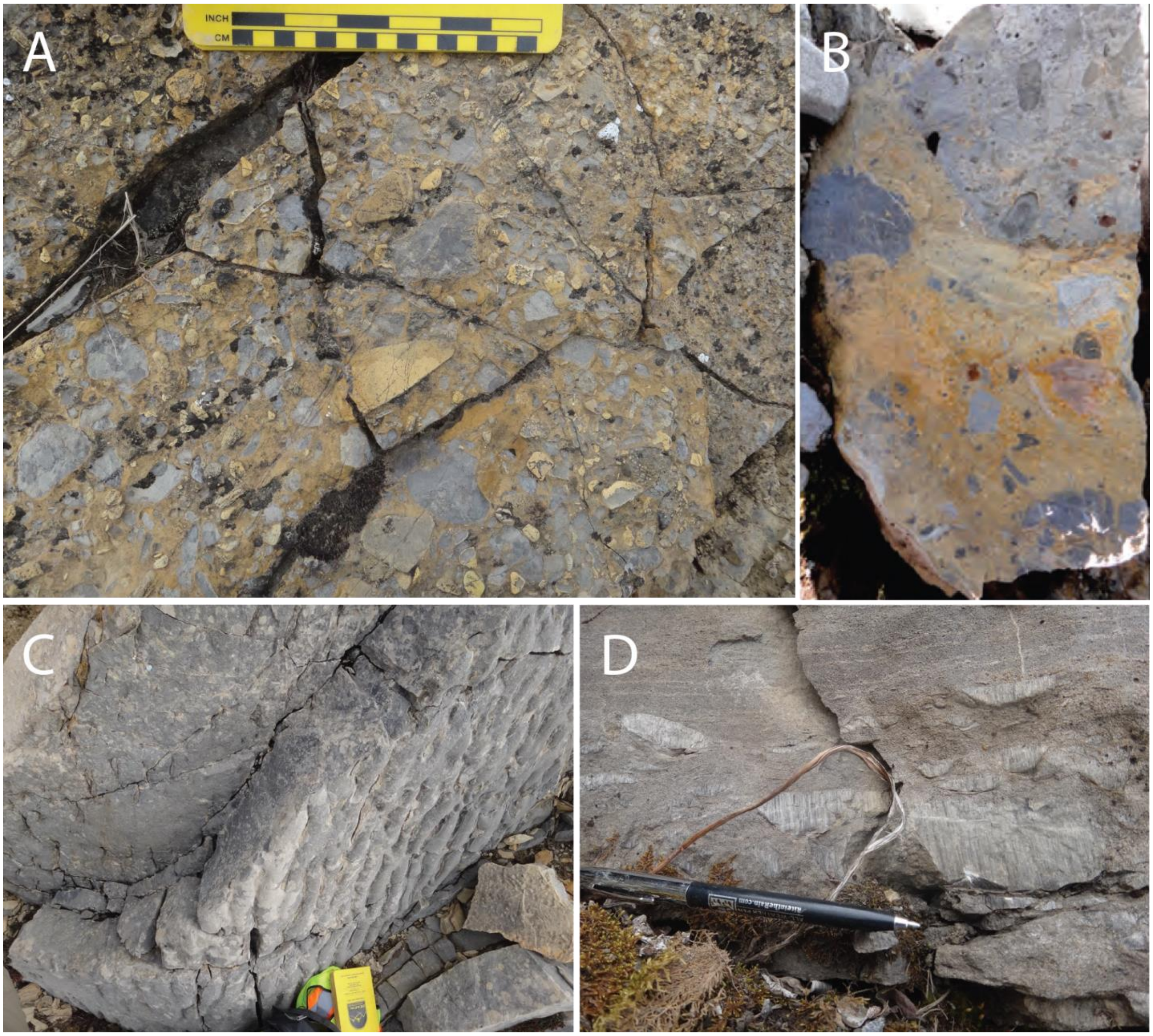

Figure B-9: Carbonate conglomerate. A. Outcrop photo. Note characteristic matrix support and tan- to grey-color. Notebook for scale. B. Hand sample photo with finger for scale. C. Ripples in calcarenite at the top of a large normally graded conglomerate bed. Notebook for scale. D. Outcrop photo of the unit. Note imbricated clasts with post-depositional bedding-perpendicular “beef” calcite features. Pen for scale.

Rust staining is typical and probably related to trace disseminated pyrite throughout the unit. Exposure of this unit is restricted to saddles on ridges and drainages west of the Conrad zone (Fig. B-5).

Figure B-10: Outcrop photo of grey shale with hand for scale.

B-3 The Osiris stratigraphic sequence

The Osiris stratigraphic package (Fig. B-2) is constrained to the north by the Nadaleen North and Conrad packages, and it extends beyond the borders of ATAC's property to the east, south and west. Mineralized rocks of the Osiris and Sunrise, Isis, and Isis East zones (Fig. B-2) occur in the Osiris limestone and dolostone. Gabbroic dikes occur in the northern part of the package proximal to the Nadaleen Fault zone and distal to gold ore zones. Structures within the sequence include faults and large-scale chevron folds that host the Osiris and Isis East ore zones.

B-3-1 Osiris shale

The maroon Osiris shale (Figs. B-1, B-5, B-11) correlates with the Stenbraten member of the Nadaleen Formation (Moynihan et al., 2014). It is distinguished from the grey shale based on color. The unit consists of mud and siltstone with rare sand lenses with 10-20% subangular to subrounded quartz grains, and otherwise fine-grained material (Cairns, 2013). Minor muscovite occurs throughout the unit. Weathered and fresh samples of the mudstone are primarily maroon and locally green in color (Figs. B-11A, B). The contact between maroon and green is typically parallel to bedding (Fig. B-11B), but in some locations it is irregular. Bedding laminations are

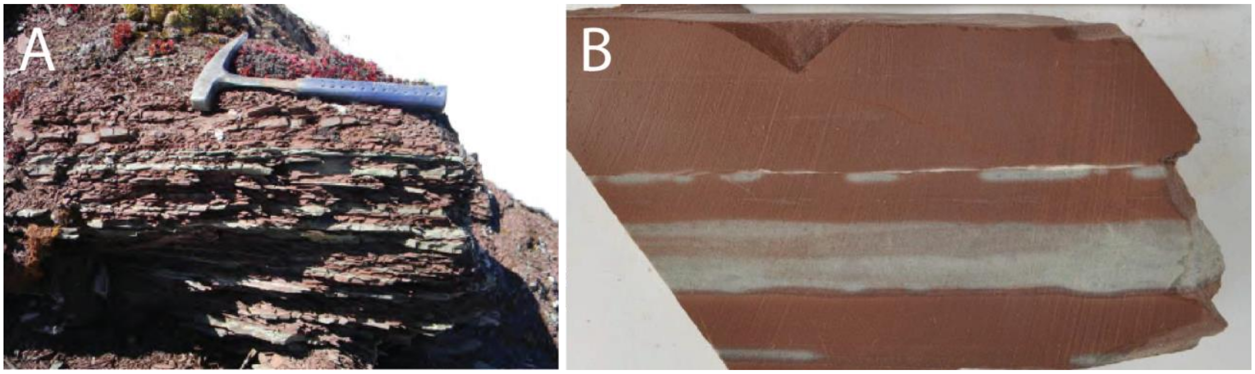

Figure B-11: Osiris shale. A. Outcrop photo. Note maroon color with distinctive green layers. Hammer for scale. B. Drill core (HQ) photo. Grey layers in fresh hand sample are equivalent to green layers in surface outcrop.

typically 1-2 mm thick throughout the unit. Although the unit weathers recessively, its distinctive color makes it a marker horizon throughout the Nadaleen Trend. Maroon outcrops of the unit are common throughout the area under cliffs formed by the highly resistant overlying Osiris limestone (Fig. B-5).

B-3-2 Osiris limestone

The Osiris limestone (Figs. B-1, B-5, B-12) correlates with the Gametrail formation (Fig. B-3) (Moynihan et al., 2014). The unit lies in transitional conformable contact with the Osiris mudstone. It consists of silty limestone (Fig. B-12A) and rudstone (Figs. B-12B, C). The silty limestone contains mm- to cm-scale laminations to 20 cm thick beds. Sedimentary structures include current ripples (Fig. B-12A) and cross, wavy (Fig. B-12D), and planar laminations (Fig. B-12E). The grain size varies from clay-size to very fine sand consisting of subrounded to subangular quartz (50%) and calcite (50%) (Cairns, 2013). Clasts in the rudstone are roughly rectangular, vary from light to dark grey, and are usually imbricated (Fig. B-12B). The matrix between the clasts in the rudstone is typically blocky white calcite (Cairns, 2013). Stylolites are present both at high angles and parallel to bedding. Weathered samples are distinctly pale grey and contain interbedded yellowish-orange intervals (Figs. B-12A, B, and C). Fresh samples are grey to dark grey (Figs. B-12D, E). Exposure of the highly resistant unit occurs on ridges and drainages throughout the Osiris stratigraphic sequence area.

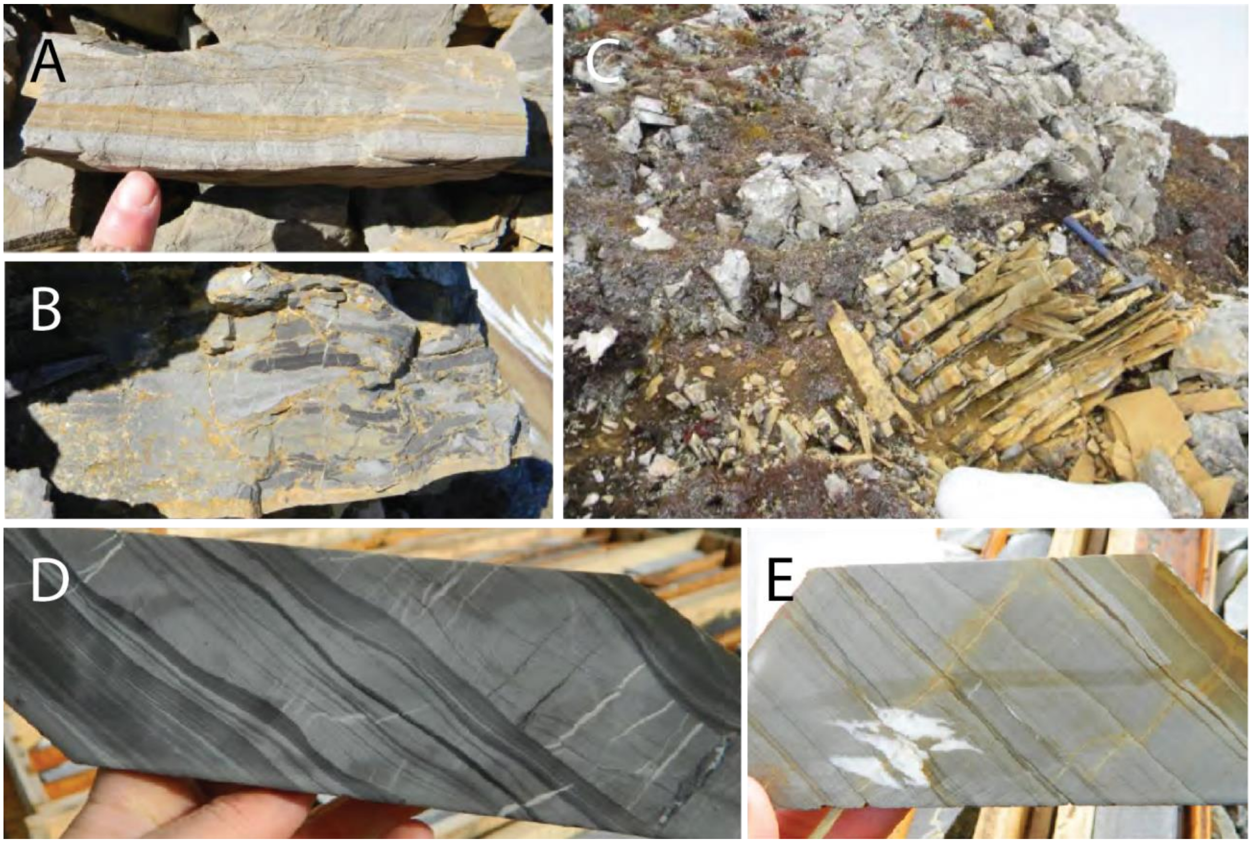

Figure B-12: Osiris limestone. A. Hand sample with finger for scale. Note ripple cross laminations and color variation. B. Hand sample photo of interbedded rudstone. Average clast width is 1cm. C. Outcrop photo with hammer for scale. Note color variation between silty limestone overlain by grey-weathering rudstone. D. Drill core (HQ) photo with ripple cross laminations. E. Drill core (HQ) photo.

B-3-3 Osiris dolostone

The Osiris dolostone (Figs. B-1, B-5, B-13) correlates with the Gametrail formation (Fig. B-3) (Moynihan et al., 2014). It lies in gradational conformable contact with the Osiris limestone. The grey-weathering cliff-forming dolostone (Fig. B-13A) is primarily massive with minor cm-scale laminations. “Zebra” dolomite is a common feature of the unit and is characterized by bedding-parallel bands of coarsely crystalline dolomite that alternate from light to dark grey. A characteristic black crackling is common and may be a result of bedding-parallel and bedding-perpendicular stylolites (Figs. B-13B, C).

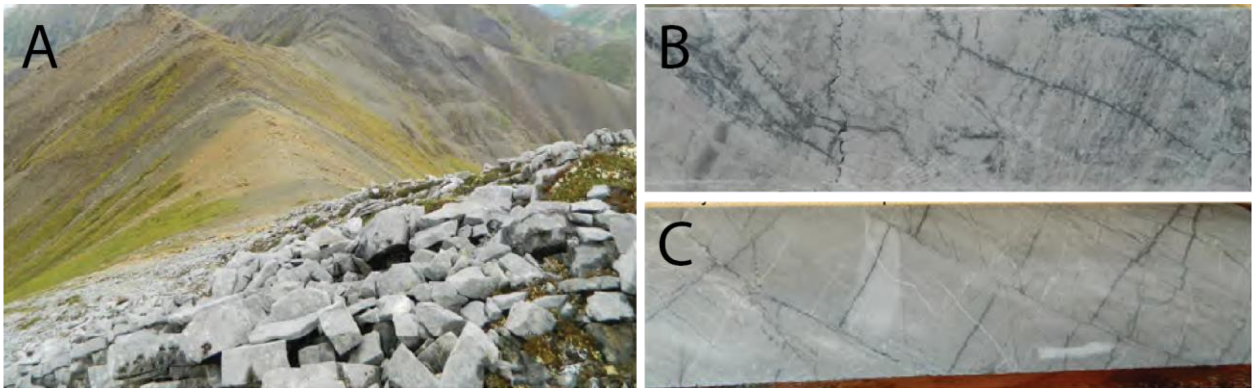

Figure B-13: Osiris dolostone. A. Outcrop photo. B. Drill core (HQ) photo with distinctive black crackle. C. Drill core (HQ) photo with distinctive black crackle.

B-3-4 Intraclast floatstone

The intraclast floatstone unit (Figs. B-1, B-14) is most likely correlative with the debris flow conglomerate member of the Blueflower formation although its presence is not mentioned by Colpron et al. (2013a) or Moynihan et al. (2014). It lies in sharp conformable contact with the Osiris dolostone. The tan- to grey-weathering unit (Fig. B-14A) is polymictic with angular to rounded clasts (Fig. B-14B) composed of pebble- to boulder-sized siltstone, dolostone, and quartzarenite. Carbonate silt and mud form the matrix.

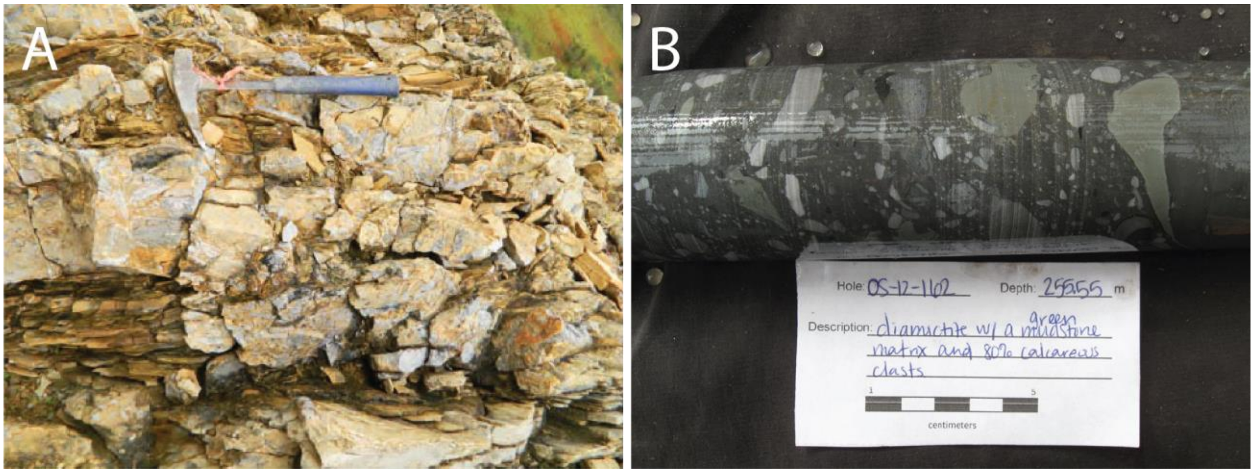

Hole: OS-12-162 Depth: 255.55 m

Description: diamictite w/ a green mudstone matrix and 80% calcareous clasts

Figure B-14: Intraclast floatstone. A. Outcrop photo with hammer for scale. B. Drill core (NQ) photo.

B-3-5 Limestone grit

The limestone grit unit (Figs. B-1, B-15) is regionally correlative with the Blueflower formation (Fig. B-3) (Moynihan et al., 2014). The unit lies in sharp conformable contact with the intraclast floatstone. It is characterized by grey- to brown-weathering gritty limestone with distinctive coarse, angular grains of quartz (Fig. B-15). Minor interbeds of planar and cross-laminated siltstone occur. Sedimentary structures include normally graded bedding and cross and planar laminations.

Figure B-15: Limestone grit. A. Hand sample photo with finger for scale. Note angularity of quartz granules

B-4 Nadaleen Fault rocks

The Nadaleen Fault zone (Figs. B-1, B-16) is a steeply NNE-dipping fault of up to 50 m wide. It rarely crops out because it weathers recessively, but where seen its rocks are rusty brown in color (Fig. B-16A). Fresh samples are dark-grey to black (Figs. B-16B, C). Fault rocks contain variably sized sheared and faulted fragments of all proximal stratigraphic units. A well-developed foliation defined by elongated clasts is typical (Figs. B-16B, C). Fine-grained matrix between the clasts is primarily composed of muscovite in a preferred direction sub-parallel to foliation (Tucker et al., 2013). Pyrite (<5%) that is both disseminated and blebby occurs

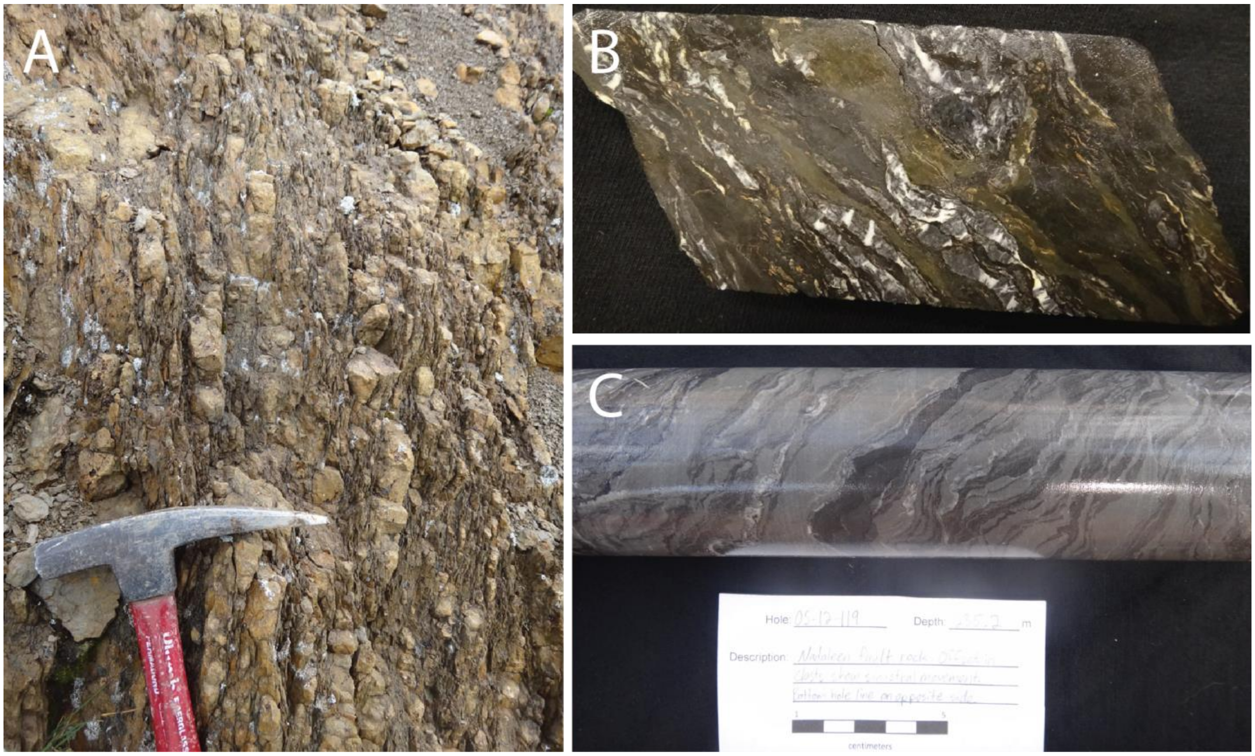

Figure B-16: Nadaleen fault rocks. A. Outcrop photo. Note foliation made up of elongate clasts is sub-parallel to the handle of the hammer used for scale. B. Drill core (NQ) photo. Note brittle elongation of limestone clasts and ductile deformation of black matrix probably sourced from Conrad siliciclastic rocks. Orange iron oxide staining represents oxidation of pyrite disseminated throughout the fault. C. Drill core (NQ) photo with distinct foliation.

throughout the fault (Tucker et al., 2013). Rarely seen kinematic indicators show many different shear sense orientations.

B-5 Gabbro

Gabbroic dikes of 25 cm – 25 m thicknesses (Figs. B-1, B-17) are seen in drill core and in surface exposure, and typically occur proximal and sub-parallel to the Nadaleen Fault zone. The color is variable: oxidized surfaces are greyish green with minor rust staining; fresh surfaces are dark grey to dark green (Figs. B-17A, B); and dikes affected by hydrothermal alteration are most commonly light green or off-white and rarely green. Dikes typically display chilled margins and commonly contain xenoliths of proximal country rocks. The gabbro is composed of amphibole (30-45%), plagioclase (25-40%), and clinopyroxene (10-15%) (Tucker et al., 2013). Pyrite is disseminated throughout the rock. Calcite amygdules are common (Fig. B-17A). Where altered,

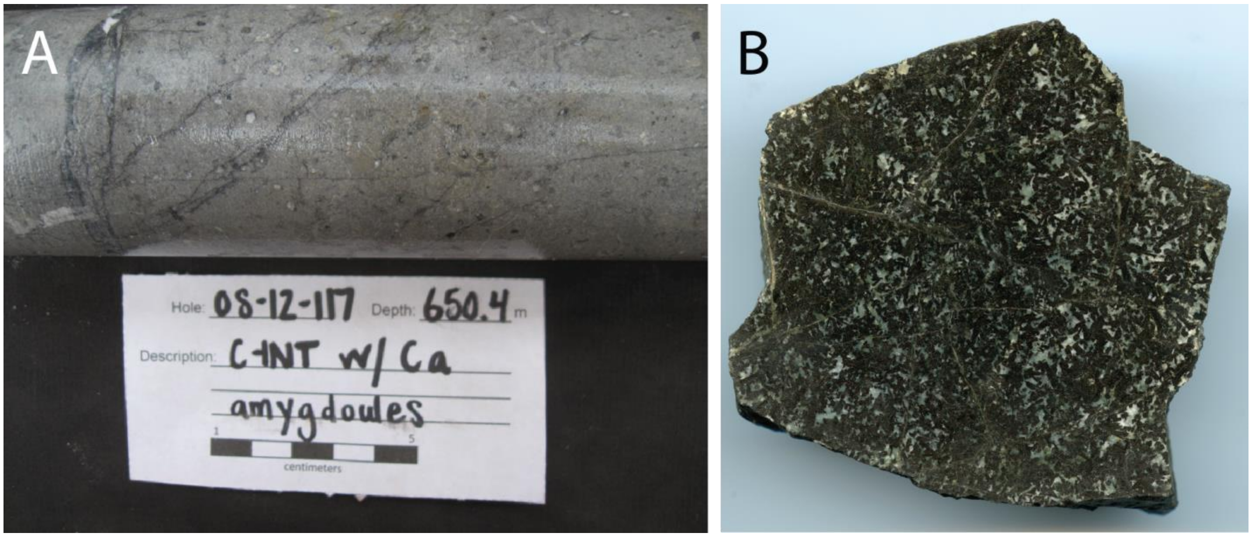

Figure B-17: Gabbro. A. Drill core (NQ) photo. Note white calcite amygdules. B. Hand sample photo. Sample is about 7 cm wide.

amphibole has been replaced by chlorite and plagioclase replaced by sericite (Tucker et al., 2013). Zircon U-Pb mineralization ages of altered gabbro intersected in drill core place maximum ages on Au mineralization at 65.49 ± 0.81 Ma (Bennett, 2013) or 74.4 ± 1.0 Ma (Mike Tucker, personal communication, 2014).

APPENDIX C
STRUCTURAL MEASUREMENTS – ORIENTED DRILL CORE

The structural measurements derived from oriented drill core are presented in the tables below. The appendix is broken up into six parts corresponding to the six horizontal plan view maps presented in the maps in Chapter 3. Each drill core's structural data is presented in a separate table and each table is sorted based on the chronological order of the drill holes. *Depth* signifies the depth where the measurement was taken. This depth may not correspond to the depth interval of the section. This is because of the angle of the drill hole and where the drill hole started with respect to the depth interval chosen for the maps. For example, drill hole OS-12-156, the first data shown in Table B-1, has a drill collar at 1451.43 m. The 100 m – 200 m interval section included data from depths between 1403.2 m and 1303.2 m. Assuming a vertical drill hole, structural data drill hole OS-12-156 could theoretically include anything from 48.23 m (1451.43 – 1403.2) to 148.23 m (1451.43 – 1303.2). In practice, these depths vary depending on the angle of the drill hole. 3D projection of the drill holes in Leapfrog Mining precisely determined the depth intervals of each drill hole. *Type* is the type of structure measured and includes bedding or foliation.

Table C-1: Structural measurements collected at depths corresponding to plan view maps in the Conrad zone.

100 - 200m Section

OS -12-156

Depth	*Type*	*Strike*	*Dip*
93.5	Bedding	143	78
95.4	Bedding	143	74
99.3	Bedding	134	63
101.1	Bedding	147	57
101.9	Bedding	179	74
102.5	Bedding	078	78
104.7	Bedding	106	89
105.5	Bedding	282	87
107.6	Bedding	134	55
114	Bedding	076	64
122.8	Bedding	019	66
126.4	Bedding	087	84
130.9	Bedding	042	74
132.7	Bedding	087	62
134.2	Bedding	095	68
136.3	Bedding	103	73
138.6	Bedding	152	81
139.5	Bedding	126	77

Table C-1: continued.

OS -12-156 (cont.d)

Depth	*Type*	*Strike*	*Dip*	*Depth*	*Type*	*Strike*	*Dip*
109.8	Bedding	123	58	142.8	Bedding	184	56
111.3	Bedding	107	60	159.8	Bedding	303	84
112.4	Bedding	090	58	160.3	Bedding	300	79
113.2	Bedding	103	50				

OS -12-188

Depth	*Type*	*Strike*	*Dip*	*Depth*	*Type*	*Strike*	*Dip*
139	Bedding	226	70	147.5	Bedding	092	64
140	Bedding	119	53	152.2	Bedding	204	56
144	Bedding	108	64	154.6	Bedding	072	79

200 - 300m Section

OS-12-103

Depth	*Type*	*Strike*	*Dip*	*Depth*	*Type*	*Strike*	*Dip*
125.88	Bedding	359	41	165.51	Bedding	187	86
128.93	Bedding	198	21	177.39	Bedding	030	84
135.03	Bedding	054	70	178.61	Bedding	049	85
134.42	Bedding	014	72	183.75	Bedding	215	71
144.02	Bedding	225	88	184	Bedding	068	76
149.35	Bedding	210	70	186	Bedding	069	68
153.01	Bedding	186	38	187	Bedding	259	83
154.53	Bedding	055	81	191.2	Bedding	053	82
155.75	Bedding	060	74	193	Bedding	186	69
157.89	Bedding	079	77	201.6	Bedding	070	77
160.63	Bedding	191	71	203.5	Bedding	060	79
162.15	Bedding	184	89	227	Bedding	075	88
162.76	Bedding	185	68	232.6	Bedding	073	72
162.80	Bedding	158	67	238.6	Bedding	062	77

OS-12-108

Depth	*Type*	*Strike*	*Dip*	*Depth*	*Type*	*Strike*	*Dip*
134.2	Bedding	057	81	197.25	Bedding	052	73
160.75	Bedding	200	74	198.5	Bedding	060	80
163.75	Bedding	188	47	200.75	Bedding	057	73
167.2	Bedding	199	66	215.3	Bedding	285	90
179.2	Bedding	327	13	218.8	Bedding	226	83

Table C-1: continued.

OS-12-108 (cont.d)

Depth	*Type*	*Strike*	*Dip*
184.75	Bedding	235	85
191.3	Bedding	223	84
194.25	Bedding	186	69

Depth	*Type*	*Strike*	*Dip*
228.55	Bedding	205	73
249.05	Bedding	057	81

OS-12-119

Depth	*Type*	*Strike*	*Dip*
180.2	Foliation	265	86
183.15	Foliation	234	86
186.35	Foliation	264	78
193.1	Foliation	269	73
196.3	Foliation	267	77
201.8	Foliation	312	73
219.7	Foliation	258	76
222	Foliation	214	59
223.8	Foliation	255	67
235.1	Foliation	276	71
231.2	Foliation	218	55
247.3	Foliation	163	45

Depth	*Type*	*Strike*	*Dip*
250	Foliation	207	58
255.7	Foliation	048	33
259.3	Foliation	096	11
264.8	Foliation	294	74
266.6	Foliation	275	65
268.8	Foliation	317	55
274.5	Foliation	284	77
277.4	Foliation	277	78
287.3	Foliation	273	85
287.3	Foliation	274	55
288	Foliation	308	69

OS-12-134

Depth	*Type*	*Strike*	*Dip*
165.5	Bedding	056	71
177.5	Bedding	074	74
182.1	Bedding	127	72
196.1	Bedding	082	82
204.6	Bedding	257	51
208.3	Bedding	256	41
213.6	Bedding	358	68

Depth	*Type*	*Strike*	*Dip*
214.3	Bedding	356	70
220.4	Bedding	283	85
225.6	Bedding	143	84
230.4	Bedding	079	82
232	Bedding	272	89
234.6	Bedding	232	85

OS -12-156

Depth	*Type*	*Strike*	*Dip*
166.2	Bedding	278	82
170	Bedding	142	80
172.5	Bedding	131	82

Depth	*Type*	*Strike*	*Dip*
174.1	Bedding	136	83
177.3	Bedding	106	80
178.5	Bedding	133	80

Table C-1: continued.

OS -12-157

Depth	Type	Strike	Dip	Depth	Type	Strike	Dip
145.5	Bedding	094	54	186	Bedding	138	56
152.1	Bedding	320	32	186.2	Bedding	193	71
160	Bedding	150	56	187.2	Bedding	169	85
164.6	Bedding	150	70	187.3	Bedding	124	55
165.7	Bedding	149	73	187.5	Bedding	182	71
168.2	Bedding	148	73	192.1	Bedding	151	42
169.4	Bedding	153	67	194.7	Bedding	178	41
183.3	Bedding	142	51	197.8	Bedding	147	58
184.5	Bedding	149	52	209.5	Bedding	260	30
184.7	Bedding	055	48	212.6	Bedding	122	53

OS -12-168

Depth	Type	Strike	Dip	Depth	Type	Strike	Dip
120.4	Bedding	030	55	133.5	Bedding	105	48

OS -12-188

Depth	Type	Strike	Dip	Depth	Type	Strike	Dip
181.5	Bedding	166	72	253	Bedding	346	57
244	Bedding	359	63	261.5	Bedding	350	59
249	Bedding	347	53	271	Bedding	018	72

S -12-192

Depth	Type	Strike	Dip	Depth	Type	Strike	Dip
284	Foliation	250	88	356.5	Foliation	304	85
293	Foliation	278	77	370	Foliation	263	78
307.5	Foliation	278	76	374	Foliation	281	86
338	Foliation	318	75				

300 - 400m Section

OS-12-108

Depth	Type	Strike	Dip	Depth	Type	Strike	Dip
160.8	Bedding	200	74	197.3	Bedding	052	73
163.8	Bedding	188	47	198.5	Bedding	060	80
167.2	Bedding	199	66	200.8	Bedding	057	73
179.2	Bedding	328	13	215.3	Bedding	285	90

Table C-1: continued.

OS-12-108 (cont.d)

Depth	*Type*	*Strike*	*Dip*	*Depth*	*Type*	*Strike*	*Dip*
182.3	Bedding	211	83	218.8	Bedding	226	83
184.8	Bedding	235	85	222.1	Bedding	046	59
191.3	Bedding	223	84	228.6	Bedding	205	71
194.3	Bedding	186	69	249.1	Bedding	057	82

OS-12-112

Depth	*Type*	*Strike*	*Dip*	*Depth*	*Type*	*Strike*	*Dip*
343.2	Bedding	090	0	394.8	Foliation	302	63
347.6	Bedding	132	90	399	Foliation	273	74
349.6	Bedding	112	88	402.6	Foliation	292	75
386.7	Foliation	283	74	413	Foliation	314	43
352	Bedding	134	78	414	Foliation	257	27
359	Bedding	014	38	414.2	Foliation	275	39
393.25	Foliation	282	56				

OS-12-119

Depth	*Type*	*Strike*	*Dip*	*Depth*	*Type*	*Strike*	*Dip*
333	Bedding	287	77	387.3	Bedding	162	69
349.6	Bedding	327	77	388.7	Bedding	008	65
359.5	Bedding	168	90	393.4	Bedding	177	54
363.2	Bedding	132	81	398.2	Bedding	215	49
368.6	Bedding	332	79	399.5	Bedding	303	37
369.1	Bedding	358	87	402.2	Bedding	167	55
370	Bedding	240	60	405.5	Bedding	301	80
375.4	Bedding	207	77	407.3	Bedding	255	87
378.3	Bedding	177	66	409.3	Bedding	069	84

OS-12-128

Depth	*Type*	*Strike*	*Dip*	*Depth*	*Type*	*Strike*	*Dip*
201.7	Bedding	244	82	224.3	Bedding	233	81
217.3	Bedding	213	59	226	Bedding	265	83
218.3	Bedding	209	64	226	Bedding	086	84
222	Bedding	226	82	231.7	Bedding	207	58
223	Bedding	223	74	236.7	Bedding	028	83
223.4	Bedding	229	88	237.2	Bedding	193	73

Table C-1: continued.

OS-12-134

Depth	*Type*	*Strike*	*Dip*
243.3	Bedding	090	61
244.3	Bedding	083	57
256.3	Bedding	265	89
263.3	Bedding	269	85
269.1	Bedding	071	72
270	Bedding	216	64
270.3	Bedding	246	86
274.1	Bedding	246	55
275.3	Bedding	133	69
284.1	Bedding	085	81
286.6	Bedding	282	85
286.7	Bedding	342	34
290.2	Bedding	125	72
311.6	Bedding	289	88
317.3	Bedding	073	73
319	Bedding	082	76
320.5	Bedding	075	90
329.3	Bedding	275	77
340.2	Bedding	082	89
341	Bedding	074	90
343.8	Bedding	088	89

OS -12-157

Depth	*Type*	*Strike*	*Dip*
262	Bedding	141	43
278.5	Bedding	233	86
292.5	Bedding	289	87
296.4	Bedding	108	87
298.3	Bedding	109	81
300.4	Bedding	125	67
303.4	Bedding	149	44
306.6	Bedding	137	55
308.9	Bedding	128	55
311.4	Bedding	181	42
313.4	Bedding	237	66
319.2	Bedding	243	76
323	Bedding	219	75
330.7	Bedding	005	86
332	Bedding	174	50
342	Bedding	199	67
346.7	Bedding	174	69
348.2	Bedding	128	49
349.2	Bedding	120	41
350.2	Bedding	243	83
350.8	Bedding	234	71
351.7	Bedding	217	69
353.4	Bedding	134	63
354.6	Bedding	145	52

OS -12-168

Depth	*Type*	*Strike*	*Dip*
154.8	Bedding	006	67
155	Bedding	019	60
170.2	Bedding	205	78
173.1	Bedding	321	89
174.5	Bedding	108	88
175.9	Bedding	105	83
191.7	Bedding	240	87
193	Bedding	341	51
198.3	Bedding	110	42
203	Bedding	058	57
206.8	Bedding	127	75
207.8	Bedding	135	83
209.8	Bedding	231	89
216	Bedding	239	82
226.4	Bedding	221	69
233.2	Bedding	058	56

Table C-1: continued.

OS -12-168 (cont.d)

Depth	*Type*	*Strike*	*Dip*	*Depth*	*Type*	*Strike*	*Dip*
193.6	Bedding	236	75	234.2	Bedding	344	36
194	Bedding	209	68				

OS -12-193

Depth	*Type*	*Strike*	*Dip*	*Depth*	*Type*	*Strike*	*Dip*
152.5	Bedding	041	80	168	Bedding	037	71
156	Bedding	047	72				

OS -12-196

Depth	*Type*	*Strike*	*Dip*	*Depth*	*Type*	*Strike*	*Dip*
102.5	Bedding	087	79	120.4	Bedding	075	82
107.5	Bedding	258	84	141.7	Bedding	076	72

400 - 500 m Section

OS-12-108

Depth	*Type*	*Strike*	*Dip*	*Depth*	*Type*	*Strike*	*Dip*
263.8	Bedding	150	26	273	Bedding	279	80
267	Bedding	181	75				

OS-12-119

Depth	*Type*	*Strike*	*Dip*	*Depth*	*Type*	*Strike*	*Dip*
405.5	Bedding	301	80	446	Bedding	225	73
407.3	Bedding	255	87	450.2	Bedding	224	87
409.3	Bedding	069	84	451.3	Bedding	070	90
410.9	Bedding	057	86	452.6	Bedding	247	80
412.5	Bedding	230	88	456.7	Bedding	067	89
416.3	Bedding	246	87	460.2	Bedding	007	58
417.7	Bedding	068	88	466.5	Bedding	252	61
421	Bedding	216	37	482.2	Bedding	349	68
424	Bedding	219	69	483.7	Bedding	185	46
425.4	Bedding	237	85	485.2	Bedding	256	81
427.2	Bedding	072	86	486.4	Bedding	260	80
430.5	Bedding	176	39	487.8	Bedding	251	83
436.9	Bedding	228	74	491.8	Bedding	253	66
438.5	Bedding	245	73	496.3	Bedding	258	64

Table C-1: continued.

OS-12-119 (cont.d)

Depth	*Type*	*Strike*	*Dip*	*Depth*	*Type*	*Strike*	*Dip*
440.5	Bedding	234	78	503.3	Bedding	251	77
442.3	Bedding	251	86	508.5	Bedding	267	87
443.2	Bedding	111	40	509.2	Bedding	078	81
443.7	Bedding	231	74	515.3	Bedding	261	83
444.9	Bedding	239	79	521.3	Bedding	244	69

OS-12-134

Depth	*Type*	*Strike*	*Dip*	*Depth*	*Type*	*Strike*	*Dip*
369.9	Bedding	284	78	439.5	Bedding	294	87
381.1	Bedding	275	75	443	Bedding	273	80
394	Bedding	258	84	444.5	Bedding	271	80
397.1	Bedding	343	49	444.9	Bedding	109	80
398	Bedding	262	39	446.3	Bedding	094	75
421.9	Bedding	265	85	446.9	Bedding	110	84
436.8	Bedding	287	76				

OS -12-148

Depth	*Type*	*Strike*	*Dip*	*Depth*	*Type*	*Strike*	*Dip*
413.1	Bedding	227	67	461.7	Bedding	272	84
417	Bedding	240	75	464.8	Bedding	144	85
419	Bedding	218	59	465.6	Bedding	171	69
421.8	Bedding	210	78	466	Bedding	350	84
433.8	Bedding	203	80	466.2	Bedding	339	71
437.3	Bedding	237	80	466.4	Bedding	335	61
443.4	Bedding	217	64	467	Bedding	346	85
457.4	Bedding	108	55	467.4	Bedding	188	87

OS -12-157

Depth	*Type*	*Strike*	*Dip*	*Depth*	*Type*	*Strike*	*Dip*
358.92	Bedding	144	74	394.5	Bedding	242	81
365	Bedding	254	66	420.2	Bedding	313	85
366.7	Bedding	230	88	422.8	Bedding	145	78
368.4	Bedding	240	85	425.6	Bedding	314	54
374.5	Bedding	242	68	440.9	Bedding	217	55
382.5	Bedding	271	87	444	Bedding	221	53
383.5	Bedding	083	88	466.5	Bedding	281	51

Table C-1: continued.

OS -12-157 (cont.d)

Depth	*Type*	*Strike*	*Dip*	*Depth*	*Type*	*Strike*	*Dip*
384.6	Bedding	090	76	468.5	Bedding	281	50
388.7	Bedding	215	83	473.7	Bedding	276	77
393.6	Bedding	236	79				

OS -12-188

Depth	*Type*	*Strike*	*Dip*	*Depth*	*Type*	*Strike*	*Dip*
397	Bedding	193	34	410	Bedding	356	70
406.3	Bedding	004	68				

OS -12-193

Depth	*Type*	*Strike*	*Dip*	*Depth*	*Type*	*Strike*	*Dip*
198.8	Bedding	041	80	263.4	Bedding	028	83
201	Bedding	017	67	289.5	Bedding	241	84
213.6	Bedding	024	73	301	Bedding	037	77
222.5	Bedding	035	88	305	Bedding	064	86
225	Bedding	229	79	308	Bedding	087	50
234	Bedding	212	88	318	Bedding	085	65
252.5	Bedding	237	86				

OS -12-196

Depth	*Type*	*Strike*	*Dip*	*Depth*	*Type*	*Strike*	*Dip*
220.8	Bedding	055	75	245.2	Bedding	062	78
224	Bedding	254	87	249.5	Bedding	047	82
232.4	Bedding	038	88	259.4	Bedding	038	75
234.5	Bedding	250	88	273	Bedding	066	75
240	Bedding	034	79	279	Bedding	045	52
243	Bedding	048	63				

500 - 600 m Section

OS-12-119

Depth	*Type*	*Strike*	*Dip*	*Depth*	*Type*	*Strike*	*Dip*
521.3	Bedding	244	69	541.3	Bedding	106	73
527.1	Bedding	009	21	544.3	Bedding	104	68
528.9	Bedding	320	61	553.6	Bedding	079	86
529.3	Bedding	337	70	554.4	Bedding	265	85

Table C-1: continued.

OS-12-119 (cont.d)

Depth	Type	Strike	Dip
533.8	Bedding	252	61
534.5	Bedding	175	33
535.3	Bedding	251	82
535.7	Bedding	149	47
536.2	Bedding	081	84
537.1	Bedding	084	76
537.5	Bedding	082	63
539.3	Bedding	102	76
557.1	Bedding	083	85
560.4	Bedding	075	80
561.3	Bedding	262	89
562.8	Bedding	085	77
566.9	Bedding	245	88
569.8	Bedding	261	81
575.2	Bedding	259	89
579	Bedding	257	65

OS-12-134

Depth	Type	Strike	Dip
456.2	Bedding	195	77
458.7	Bedding	167	77
459.5	Bedding	225	62
461.4	Bedding	110	70
462.2	Bedding	274	88
462.9	Bedding	266	76
463.1	Bedding	276	50
463.2	Bedding	264	77
464.3	Bedding	057	67
465.4	Bedding	063	90
467.1	Bedding	098	74
468.5	Bedding	074	69
469.1	Bedding	276	82
473.7	Bedding	078	56
481.6	Bedding	270	78
484.9	Bedding	055	86
492.4	Bedding	269	89
493.3	Bedding	102	84
494.4	Bedding	180	87
498	Bedding	272	90
501.2	Bedding	012	76
501.7	Bedding	309	88
505.5	Bedding	104	75
512.6	Bedding	320	85
512.9	Bedding	284	90
522	Bedding	180	78
530.7	Bedding	294	26
531	Bedding	086	90
533.2	Bedding	059	81
534.8	Bedding	050	73
537.4	Bedding	065	63

OS -12-148

Depth	Type	Strike	Dip
485.8	Bedding	145	53
489.6	Bedding	026	46
489.7	Bedding	034	27
490.7	Bedding	071	38
498.1	Bedding	336	78
498.6	Bedding	041	67
500	Bedding	360	81
539.9	Bedding	141	88
543.2	Bedding	141	62
543.9	Bedding	144	64
545.3	Bedding	071	43
547.3	Bedding	341	76
548.1	Bedding	120	69
550.4	Bedding	186	54

Table C-1: continued.

OS -12-148 (cont.d)

Depth	*Type*	*Strike*	*Dip*
506.5	Bedding	339	50
509.3	Bedding	022	39
511.1	Bedding	029	67
512.4	Bedding	053	55
514.2	Bedding	281	41
519.9	Bedding	023	52
527.1	Bedding	182	69
528	Bedding	146	62
532.3	Bedding	191	71
532.7	Bedding	174	70
533.4	Bedding	004	78
534.1	Bedding	180	86

Depth	*Type*	*Strike*	*Dip*
553.8	Bedding	204	15
555.7	Bedding	136	19
556.3	Bedding	198	37
559	Bedding	351	23
568	Bedding	187	72
573.9	Bedding	195	77
578.7	Bedding	184	77
579.8	Bedding	191	72
580.8	Bedding	333	74
581.2	Bedding	186	64
582.6	Bedding	206	56

OS -12-157

Depth	*Type*	*Strike*	*Dip*
476	Bedding	112	72
478.6	Bedding	136	62
507.7	Bedding	221	83
510.1	Bedding	059	74
512.3	Bedding	231	77
519.2	Bedding	019	84
525.5	Bedding	044	85
529.6	Bedding	044	85
548.5	Bedding	200	90

Depth	*Type*	*Strike*	*Dip*
552.2	Bedding	018	88
554	Bedding	229	78
557.3	Bedding	220	89
558.2	Bedding	220	83
566.1	Bedding	202	86
571	Bedding	145	77
574.6	Bedding	137	74
574.9	Bedding	131	70
578.2	Bedding	117	52

OS -12-193

Depth	*Type*	*Strike*	*Dip*
334.5	Bedding	080	84
348.5	Bedding	233	88
352	Bedding	064	86
359	Bedding	031	66
362.5	Bedding	021	70
362.55	Bedding	021	70
375.5	Bedding	279	86
378	Bedding	250	82
382.5	Bedding	066	81
383.6	Bedding	251	87

Depth	*Type*	*Strike*	*Dip*
391	Bedding	076	69
393.5	Bedding	025	60
396.4	Bedding	066	81
408.5	Bedding	082	65
412	Bedding	106	77
419	Bedding	094	84
422.5	Bedding	048	60
426	Bedding	038	84
430.5	Bedding	031	72
442.5	Bedding	243	89

Table C-1: continued.

OS -12-193 (cont.d)

Depth	*Type*	*Strike*	*Dip*
388	Bedding	047	72

OS -12-196

Depth	*Type*	*Strike*	*Dip*	*Depth*	*Type*	*Strike*	*Dip*
289.5	Bedding	022	68	327.7	Bedding	103	49
297	Bedding	039	82	335	Bedding	045	73
302	Bedding	021	58	349.5	Bedding	038	59
306	Bedding	016	75	355.5	Bedding	038	59
310.8	Bedding	019	72	397	Bedding	024	72
311	Bedding	327	87	399	Bedding	024	72
312.2	Bedding	246	83	401	Bedding	190	65
315	Bedding	057	69	409.8	Bedding	315	75
318	Bedding	121	81	420	Bedding	215	77
322.2	Bedding	057	69	420.5	Bedding	190	65
325.6	Bedding	135	65	420.6	Bedding	218	88

600 - 700 m Section

OS -12-148

Depth	*Type*	*Strike*	*Dip*	*Depth*	*Type*	*Strike*	*Dip*
589.7	Bedding	214	84	646.6	Bedding	214	85
590.1	Bedding	186	69	647	Bedding	215	88
591.2	Bedding	179	75	647.6	Bedding	002	59
594.9	Bedding	186	81	648.2	Bedding	339	59
596.3	Bedding	198	71	648.7	Bedding	018	54
597	Bedding	282	36	649.5	Bedding	233	84
599.1	Bedding	285	34	650.4	Bedding	344	65
601.9	Bedding	195	65	651.6	Bedding	351	80
603	Bedding	195	71	653.7	Bedding	348	78
607.6	Bedding	184	70	656.6	Bedding	166	88
608	Bedding	180	69	657.1	Bedding	176	80
609	Bedding	172	74	663.2	Bedding	205	87
611.4	Bedding	179	80	665.3	Bedding	191	70
614.5	Bedding	183	73	669.2	Bedding	192	67
615.7	Bedding	201	79	670.5	Bedding	201	78
622.5	Bedding	180	73	673.9	Bedding	212	67
633.5	Bedding	201	90	675.6	Bedding	224	66

Table C-1: continued.

OS -12-148

Depth	Type	Strike	Dip	Depth	Type	Strike	Dip
637	Bedding	059	90	676.4	Bedding	203	13
640.3	Bedding	070	75	677.3	Bedding	207	67
642.3	Bedding	202	83	679.5	Bedding	177	75
645	Bedding	027	87	692.3	Bedding	181	86

OS -12-148

Depth	Type	Strike	Dip	Depth	Type	Strike	Dip
596.7	Bedding	179	75	600.8	Bedding	176	64
598.5	Bedding	173	74				

OS -12-193

Depth	Type	Strike	Dip	Depth	Type	Strike	Dip
454	Bedding	229	90	478	Bedding	072	88
458	Bedding	054	82	482	Bedding	072	88
462	Bedding	087	90	497.1	Bedding	243	89
467	Bedding	259	86	512	Bedding	080	79
473	Bedding	050	80	516	Bedding	101	83

OS -12-196

Depth	Type	Strike	Dip	Depth	Type	Strike	Dip
432.5	Bedding	180	90	535	Bedding	068	82
465.5	Bedding	026	87	542	Bedding	059	88
471	Bedding	184	49	551	Bedding	252	89
489.5	Bedding	102	63	556.5	Bedding	252	89
495	Bedding	101	84	562.5	Bedding	253	82
502	Bedding	070	84	568.6	Bedding	140	79
505	Bedding	067	88	595	Bedding	243	89
512	Bedding	330	74	611.5	Bedding	327	80
516	Bedding	028	63	611.6	Bedding	250	84
518	Bedding	258	87	619	Bedding	138	88
525	Bedding	056	73	620	Bedding	344	89
532	Bedding	264	79				

APPENDIX D
STRUCTURAL MEASUREMENTS – NADALEEN TREND

Structural measurements from the Nadaleen Trend including simplified results of Kuiper (2012) and those collected during the summer 2012 field season in the Conrad domain are shown. Kuiper's (2012) work included more detailed mapping in the Osiris and Isis East zones; in this thesis, this work was collected into the more concise *Osiris Anticline*, *Isis East Anticline*, and *Far East Limb* domains in Figure 2.6. The table is broken up into three sections corresponding to the stratigraphic domains that are listed in bold italics: Nadaleen North Domain, Conrad Domain, and Osiris Domain. In each section, the corresponding domains are listed in the order from north to south. Listed under the domains are the structural measurements taken including bedding and cleavage measured using right-hand-rule and hinge lines in five separate columns. Axial planes, veins, and joints were measured in the field but not included.

Table D-1: Structural measurements collected throughout the Nadaleen Trend.

Nadaleen North Domain

North of Nadaleen

Bedding

Strike	*Dip*	*Strike*	*Dip*	*Strike*	*Dip*	*Strike*	*Dip*	*Strike*	*Dip*
072	73	258	72	073	28	107	65	128	63
134	22	258	64	270	58	075	63	145	88
150	60	292	30	298	50	025	38	126	76
157	23	292	51	320	68	056	27	097	49
067	32	209	45	036	47	131	69	114	59
074	32	142	68	195	87	134	70	106	80
068	31	146	56	315	80	233	54	096	50
311	16	152	59	300	78	130	82	091	80
357	10	194	30	276	88	116	78	286	84

Cleavage

Strike	*Dip*	*Strike*	*Dip*	*Strike*	*Dip*	*Strike*	*Dip*	*Strike*	*Dip*
278	62	188	43	321	85	091	80	173	85
323	82	293	72	100	90	258	64	229	45
305	67	275	61	286	84	258	72	305	56
020	74	315	71						

Table D-1: continued.

Conrad Domain

N-limb Zone

Bedding

Strike	*Dip*	*Strike*	*Dip*	*Strike*	*Dip*	*Strike*	*Dip*	*Strike*	*Dip*
069	80	301	68	321	75	323	45	260	84
072	73	326	65	314	75	312	81	281	33

Hinge Line

Trend	*Plunge*	*Trend*	*Plunge*
192	76	138	46

N-Limb on Ridge

Bedding

Strike	*Dip*	*Strike*	*Dip*	*Strike*	*Dip*	*Strike*	*Dip*	*Strike*	*Dip*
087	64	099	56	093	58	093	59	112	64

Hinge Line

Trend	*Plunge*
093	49

N-fold in Carbonate Diamictite

Bedding

Strike	*Dip*	*Strike*	*Dip*	*Strike*	*Dip*	*Strike*	*Dip*	*Strike*	*Dip*
091	80	082	69	230	79	286	55	037	69
248	58	285	55	110	65	059	52	080	83
086	75	162	56	095	78	014	66	046	67
221	84	202	70	293	62	051	74	231	57
032	89	050	60	057	63	082	56	036	72

Hinge Line

Trend	*Plunge*	*Trend*	*Plunge*	*Trend*	*Plunge*	*Trend*	*Plunge*	*Trend*	*Plunge*
242	63	190	59	262	75	254	51	261	58
209	64	234	57	240	52				

Cleavage

Strike	*Dip*
312	71

Fe-Oxide Ridge

Bedding

Strike	*Dip*	*Strike*	*Dip*	*Strike*	*Dip*	*Strike*	*Dip*	*Strike*	*Dip*
122	81	123	69	105	69	138	79	108	67
138	79	108	67	115	36	108	75		

Table D-1: continued.

Fe-Oxide Ridge (cont.d)

Hinge Line

Trend	*Plunge*
276	27

Conrad Anticline

Bedding

Strike	*Dip*	*Strike*	*Dip*	*Strike*	*Dip*	*Strike*	*Dip*	*Strike*	*Dip*
090	74	190	73	356	58	126	68	341	80
150	72	099	72	063	73	087	41	350	83
240	30	101	51	159	78	094	84	218	72
046	79	128	72	065	89	094	52	210	74
150	66	150	86	107	76	212	69	029	85
103	48	023	84	130	77	237	73	033	77
123	73	023	84	116	63	260	77	113	62
117	78	140	75	052	75	314	78	014	71
100	53	169	58	115	83	130	83	143	74
119	83	110	48	115	84	108	65	115	74
131	76	135	68	131	78	133	76	114	61
111	75	133	74	113	86	108	90	124	80
121	82	297	85	128	71	122	87	114	80
310	89	186	66	182	74	198	81	191	77
193	68	000	74	346	43	356	60	000	63
001	59	350	51	169	57	170	62	161	76
163	58	186	42	171	57	046	81	071	86
076	77	068	73	068	72	060	84	043	65
030	44	095	83	169	82	179	66	205	59
215	86	033	85	203	77	031	83	011	82
012	84	008	84	022	81	022	85	013	82
024	78	038	77	034	85	031	90	032	85
016	88	220	87	231	83	248	83	233	81
153	83	155	80	327	89	344	89	149	81
106	67	154	73	346	85	332	85	150	86
152	85	153	86	351	89	171	77	166	81
334	86	148	80	139	84	318	86	140	81
128	80	131	85	137	81	146	87		

Hinge Line

Trend	*Plunge*	*Trend*	*Plunge*	*Trend*	*Plunge*	*Trend*	*Plunge*	*Trend*	*Plunge*
172	5	137	35	205	59	165	60	173	66
319	30	175	65	182	75	155	68	182	63
202	60	179	66	164	68	219	86	194	90

Table D-1: continued.

S-fold in Carbonate Diamictite

Bedding

Strike	*Dip*	*Strike*	*Dip*	*Strike*	*Dip*	*Strike*	*Dip*	*Strike*	*Dip*
353	34	231	57	061	59	018	49	039	27
051	74	036	72	087	84	325	63	055	56
082	56	089	59	228	33	347	28	053	71
037	69	358	35	029	50	341	60	060	82
080	83	037	36	359	57	059	62	233	75
046	67	034	10						

Dolostone Area

Bedding

Strike	*Dip*	*Strike*	*Dip*	*Strike*	*Dip*	*Strike*	*Dip*	*Strike*	*Dip*
098	67	070	62	092	72	065	53	061	67
118	58	280	86	088	78	109	57	088	62
101	62	085	71	097	38	075	69	089	79

Ravine Area

Bedding

Strike	*Dip*	*Strike*	*Dip*	*Strike*	*Dip*	*Strike*	*Dip*	*Strike*	*Dip*
173	61	229	52	163	68	133	75	091	70
187	74	232	82	233	90	140	60	145	75
225	72	297	74	161	55	094	73	128	84
045	71								

Hinge Line

Trend	*Plunge*	*Trend*	*Plunge*	*Trend*	*Plunge*
065	53	110	68	242	45

Osiris Domain

Go Home Creek

Bedding

Strike	*Dip*	*Strike*	*Dip*	*Strike*	*Dip*	*Strike*	*Dip*	*Strike*	*Dip*
347	76	339	85	338	76	325	74	319	47
348	84								

Cleavage

Strike	*Dip*	*Strike*	*Dip*	*Strike*	*Dip*
071	86	066	78	055	27

Isis Siliciclastics

Bedding

Strike	*Dip*	*Strike*	*Dip*	*Strike*	*Dip*	*Strike*	*Dip*	*Strike*	*Dip*
350	88	025	40	032	18	347	71	335	90
356	34	013	30	085	16	327	80	340	83

Table D-1: continued.

Isis Siliciclastics (cont.d)

Bedding

Strike	*Dip*	*Strike*	*Dip*	*Strike*	*Dip*	*Strike*	*Dip*	*Strike*	*Dip*
335	36	069	21	001	40	328	86	138	39
340	60	338	24	344	65	292	64	101	12
355	66	343	27	330	84	138	88	083	31
000	68	315	42	068	37	297	53	340	78
019	47	321	74	102	18	319	64	319	21
117	55	041	32	122	52	336	78	306	37
347	63	293	69	349	49	176	55	147	48
358	41	158	82	008	26	166	67	111	30
180	57	019	53	000	56	351	70	350	88
145	51	353	48						

Cleavage

Strike	*Dip*	*Strike*	*Dip*	*Strike*	*Dip*
027	84	239	76	103	69

Hinge Line

Trend	*Plunge*	*Trend*	*Plunge*	*Trend*	*Plunge*	*Trend*	*Plunge*	*Trend*	*Plunge*
173	26	160	37	164	36	110	57	149	29
122	40	167	44	138	42	116	38	159	57

Osiris Anticline

Bedding

Strike	*Dip*	*Strike*	*Dip*	*Strike*	*Dip*	*Strike*	*Dip*	*Strike*	*Dip*
192	72	200	79	023	81	018	86	130	49
181	72	010	46	055	90	032	66	153	64
087	32	082	36	228	90	199	88	153	62
088	46	088	47	179	74	182	84	145	55
085	57	162	86	030	76	007	80	138	46
187	89	110	59	102	81	160	80	122	32
090	31	101	41	110	41				

Cleavage

Strike	*Dip*	*Strike*	*Dip*
212	57	204	64

Hinge Line

Trend	*Plunge*	*Trend*	*Plunge*	*Trend*	*Plunge*	*Trend*	*Plunge*	*Trend*	*Plunge*
198	67	184	44	198	45	203	63	179	69
173	39	200	50						

Table D-1: continued.

Osiris Shale

Bedding

Strike	*Dip*	*Strike*	*Dip*	*Strike*	*Dip*	*Strike*	*Dip*	*Strike*	*Dip*
161	38	160	27	112	26	212	57	207	52
156	33	125	27						

Cleavage

Strike	*Dip*	*Strike*	*Dip*	*Strike*	*Dip*	*Strike*	*Dip*	*Strike*	*Dip*
188	90	359	83	300	35	314	33	294	75

Isis East Anticline

Bedding

Strike	*Dip*	*Strike*	*Dip*	*Strike*	*Dip*	*Strike*	*Dip*	*Strike*	*Dip*
147	77	169	70	115	70	182	72	131	74
186	66	166	78	118	73	138	74	097	65
172	69	167	66	116	69	181	64	180	76
212	82	180	88	108	70	170	69	165	72
349	71	122	61	077	84	180	65	165	72
128	84	112	60	096	76	163	72	172	36
022	60	119	56	105	76	154	65	202	82
325	75	297	90	150	80	143	73	157	72
313	84	112	56	112	74	159	76	165	79
018	89	207	88	118	80	148	76	163	79
018	90	115	50	118	74	151	80	189	79
196	80	103	52	136	67	156	78	163	79
119	74	100	55	183	59	143	88	003	78
140	72	040	75	102	86	090	76	156	49
135	70	081	57	224	84	066	71	099	70
149	64	109	44	128	85	045	69	088	69
156	83	107	72	115	66	061	76	084	72
150	79	109	49	068	76	064	70	169	89
349	70	114	41	160	82	255	89	045	73
347	76	116	59	124	68	217	84	042	75
120	29	143	52	083	70	015	68	039	48
062	56	050	54	031	71	044	62	047	41
068	56								

Cleavage

Strike	*Dip*	*Strike*	*Dip*	*Strike*	*Dip*	*Strike*	*Dip*	*Strike*	*Dip*
271	76	022	81	228	74	250	76	147	38
182	88	050	81	242	80	074	84	142	54
268	80	259	72						

Hinge Line

Trend	*Plunge*	*Trend*	*Plunge*	*Trend*	*Plunge*	*Trend*	*Plunge*	*Trend*	*Plunge*
236	73	215	68	302	69	145	68	269	70
131	49	132	69	318	56	261	82	254	65
058	82	216	61	165	62	015	57	241	66

Table D-1: continued.

Hinge Line

Trend	*Plunge*	*Trend*	*Plunge*	*Trend*	*Plunge*	*Trend*	*Plunge*	*Trend*	*Plunge*
216	82	132	46	142	59	215	75	239	61
194	50	215	67	130	80	208	48		

Far East Limb

Bedding

Strike	*Dip*	*Strike*	*Dip*	*Strike*	*Dip*	*Strike*	*Dip*	*Strike*	*Dip*
120	29	115	66	255	89	156	49	050	54
081	57	068	76	217	84	099	70	031	71
109	44	160	82	015	68	088	69	044	62
107	72	124	68	215	44	084	72	047	41
109	49	083	70	235	47	169	89	040	75
114	41	090	76	217	62	045	73	102	86
116	59	066	71	044	64	042	75	063	57
143	52	045	69	172	52	039	48	089	36
224	84	061	76	175	29	062	56	068	56
128	85	064	70	077	54				

Cleavage

Strike	*Dip*	*Strike*	*Dip*
147	38	142	54

Hinge Line

Trend	*Plunge*	*Trend*	*Plunge*	*Trend*	*Plunge*	*Trend*	*Plunge*	*Trend*	*Plunge*
208	48	254	65	239	61	215	31	080	30
269	70	241	66	270	62	236	41		

APPENDIX E
STRUCTURAL MEASUREMENTS – REGION

This appendix shows the regional structural measurements collected from work done by Colpron et al. (2013a) and Moynihan et al. (2014). The table below is divided into sections corresponding to the structural domains listed in bold. Under each structural domain, the corresponding trends of measured reverse faults and fold axial traces are listed. Dip and plunge were not available and thus were not included.

Table E-1: Structural measurements collected throughout the region surrounding the eastern Nadaleen Trend.

Upper Plate Dawson Thrust

Reverse Fault

Trend	*Trend*	*Trend*	*Trend*	*Trend*
121	125	120	130	101
088	120	110	105	123
125	127	84		

Fold Axial Trace

Trend	*Trend*	*Trend*
112	112	104

Overlap Assemblage

Reverse Fault

Trend	*Trend*	*Trend*	*Trend*	*Trend*
092	075	105	300	092

Fold Axial Trace

Trend	*Trend*	*Trend*	*Trend*	*Trend*
118	130	132	125	109
100	110	107	104	090
100	107	092	090	082
100				

Table E-1: continued.

Nadaleen Area

Reverse Fault

Trend	*Trend*	*Trend*	*Trend*	*Trend*
274	085	277	124	165
075	310	270		

Fold Axial Trace

Trend	*Trend*	*Trend*	*Trend*	*Trend*
105	075	075	055	110
090	100	100	092	055
050	090	092	074	120
055	092			

North of Nadaleen

Reverse Fault

Trend
272

Fold Axial Trace

Trend	*Trend*	*Trend*	*Trend*	*Trend*
075	068	063	045	038
050	080	043	065	136
075	108	050	098	068
083	105	054		

Northeast Nadaleen

Reverse Fault

Trend	*Trend*	*Trend*	*Trend*	*Trend*
270	294	269	125	320
275	278	050		

Fold Axial Trace

Trend	*Trend*	*Trend*	*Trend*	*Trend*
100	110	122	095	088
111	110	114	100	100
118	099	054	095	099
106	096	122	115	

Eastern Nadaleen

Reverse Fault

Trend	*Trend*	*Trend*
075	115	145

Table E-1: continued.

Eastern Nadaleen (cont.d)

Fold Axial Trace

Trend	*Trend*	*Trend*	*Trend*	*Trend*
120	122	138	135	140
120	140	135	147	140
145	124	134		

APPENDIX F
GEOCHEMICAL VALUES

Average geochemical values for each plan view map within the Conrad zone (Fig. 3.1) are given in the tables below. The table is separated into six sections for each level: 100 – 200 m, 200 – 300 m, 300 – 400 m, 400 – 500 m, 500 – 600 m, and 600 – 700 m. Each table is sorted based on the chronological order of the drill holes. *To* and *From* signify the depth interval corresponding to the plan view map (Figs. 3.1). *Total Au* was summed from the respective depth interval on ATAC Resource's proprietary assay table. Grade thickness (*Au/m*) was derived by dividing the *Total Au* by the Length (*From – To*). Ca and Mg concentrations are given in weight percent and were averaged for only the limestone interval of each drill hole. If limestone was not intersected or if an intersected limestone interval was less than 10 m, the average concentration shows SLC for siliciclastic rocks.

Table F-1: Average geochemical concentrations corresponding to plan view maps in the Conrad Au zone (Fig. 3.1).

100 – 200m Section

Hole Name	*To*	*From*	*Au/m*	*Average Ca*	*Average Mg*
OS -10-008	100.58	109.73	0.003	SLC	SLC
OS -10-010	111.75	245.36	1.219	27.38	0.45
OS -11-011	77.2	166.12	0.141	24.38	1.05
OS -11-013	86.87	196.6	0.002	25.48	1.74
OS -11-014	142.33	176.78	0.023	SLC	SLC
OS -11-016	62.18	193.4	0.831	27.49	0.7
OS -11-017	114.3	173.74	0.020	SLC	SLC
OS -11-019	77.72	207.26	0.274	30.95	0.84
OS -11-021	59.44	158.5	0.019	SLC	SLC
OS -11-022	114.3	134.11	0.010	SLC	SLC
OS -11-025	62.48	173.74	0.006	SLC	SLC
OS -11-027	64.01	178.31	0.002	SLC	SLC
OS -11-030	140.21	271.27	0.777	27.3	0.38
OS -11-036	118.87	229	0.005	SLC	SLC

Table F-1: continued.

100 – 200m Section (cont.d)

Hole Name	*To*	*From*	*Au/m*	*Average Ca*	*Average Mg*
OS -11-042	135.69	268.22	0.427	20.57	1.35
OS -11-045	112.78	222.5	0.162	26.31	0.97
OS -11-050	21.34	137.16	0.587	26.92	0.56
OS -11-051	17.68	128.93	0.003	SLC	SLC
OS -11-054	16.76	123.44	0.125	SLC	SLC
OS -11-058	0	110.64	0.020	SLC	SLC
OS -11-059	0	54	0.013	SLC	SLC
OS -11-060	0	128.02	0.014	SLC	SLC
OS -11-062	0	113.69	0.321	29.04	0.25
OS -11-063	0	120.4	0.003	SLC	SLC
OS -11-066	0	75.28	0.002	SLC	SLC
OS -11-069	21.34	149.35	0.002	SLC	SLC
OS -11-070	56.39	173.74	0.132	SLC	SLC
OS -11-074	21.95	148.44	0.017	SLC	SLC
OS -12-092	161.54	268.22	0.001	SLC	SLC
OS -12-093	71.93	185.35	0.039	SLC	SLC
OS -12-094	87.78	197.51	0.017	SLC	SLC
OS -12-098	35.05	163.07	1.454	20.94	0.76
OS -12-100	119.79	227.99	0.002	SLC	SLC
OS -12-102	62.79	166.42	0.020	SLC	SLC
OS -12-103	0	116.74	2.711	19.75	0.35
OS -12-105	57.91	167.64	0.005	SLC	SLC
OS -12-106	111.21	213.06	0.011	23.4	1.12
OS -12-108	0	118.26	0.754	25.21	0.75
OS -12-109	64.92	174.65	0.003	SLC	SLC
OS -12-112	74.07	209.7	0.125	SLC	SLC
OS -12-113	106.07	141.3	0.002	SLC	SLC
OS -12-114	31.39	129.69	3.438	17.09	0.57
OS -12-116	0	103.02	0.024	SLC	SLC
OS -12-117	110.03	213.66	0.004	SLC	SLC
OS -12-119	65.84	180.14	0.001	SLC	SLC
OS -12-121	0	101.5	0.189	27.85	0.51
OS -12-123	0	86.26	0.031	SLC	SLC
OS -12-128	0	78.64	0.021	SLC	SLC
OS -12-129	68.58	171.91	0.001	SLC	SLC
OS -12-130	0	20.69	0.058	SLC	SLC
OS -12-132	0	110.64	0.004	SLC	SLC
OS -12-134	23.77	135.03	0.006	SLC	SLC
OS -12-137	0	118.26	0.006	SLC	SLC
OS -12-138	0	24.38	0.172	SLC	SLC

Table F-1: continued.

100 – 200m Section (cont.d)

Hole Name	*To*	*From*	*Au/m*	*Average Ca*	*Average Mg*
OS -12-141	0	48.77	1.434	11.64	0.93
OS -12-142	0	30.18	0.177	27.01	0.41
OS -12-144	0	41.15	0.571	25.38	0.59
OS -12-145	0	41.15	0.030	SLC	SLC
OS -12-146	23.77	127.41	0.002	SLC	SLC
OS -12-148	59.44	163.8	0.489	SLC	SLC
OS -12-149	0	110.64	0.002	SLC	SLC
OS -12-155	14.63	130.45	0.012	SLC	SLC
OS -12-156	51.82	161.54	0.166	SLC	SLC
OS -12-157	0	124.36	0.003	SLC	SLC
OS -12-161	49.68	153.03	0.008	SLC	SLC
OS -12-163	0	80.77	1.115	23.46	0.31
OS -12-164	14.63	145.69	0.004	SLC	SLC
OS -12-165	0	99.06	0.992	25.62	0.34
OS -12-168	0	30.48	0.135	SLC	SLC
OS -12-169	0	60.05	2.472	18.52	0.5
OS -12-170	0	118.26	0.002	SLC	SLC
OS -12-174	0	26.51	0.185	SLC	SLC
OS -12-175	0	37.49	0.553	SLC	SLC
OS -12-176	13.11	125.88	0.184	SLC	SLC
OS -12-178	11.58	116.74	1.579	23.71	0.63
OS -12-180	0	29.57	0.293	SLC	SLC
OS -12-182	0	104.55	0.002	SLC	SLC
OS -12-183	55.78	186.84	1.217	25.03	0.61
OS -12-184	0	28.12	0.006	SLC	SLC
OS -12-185	51.21	154.84	0.016	SLC	SLC
OS -12-186	19.2	135.03	0.008	SLC	SLC
OS -12-187	0	35.97	0.004	SLC	SLC
OS -12-188	60.35	173.13	0.002	SLC	SLC
OS -12-190	91.44	222.5	0.016	SLC	SLC
OS -12-191	129.8	231.34	0.001	SLC	SLC
OS -12-192	134.11	265.28	0.001	20.75	1.26
OS -12-194	140.7	249.02	0.001	SLC	SLC
OS -12-195	139.5	249.94	0.096	SLC	SLC
OS -12-197	0	37.49	0.009	SLC	SLC

Table F-1: continued.

200 – 300m Section

Hole Name	*To*	*From*	*Au/m*	*Average Ca*	*Average Mg*
OS -10-009	0	96	0.040	SLC	SLC
OS -10-010	245.36	335.28	0.481	24.5	0.64
OS -11-013	196.6	306.32	0.055	29.69	0.67
OS -11-016	193.4	280.42	0.531	14.92	0.98
OS -11-019	207.26	243.84	0.010	32.27	0.59
OS -11-021	158.5	170.69	0.000	SLC	SLC
OS -11-025	173.74	263.96	0.159	SLC	SLC
OS -11-030	271.27	399.29	0.615	24.09	0.73
OS -11-036	229	339.85	0.028	27.36	0.96
OS -11-042	268.22	393.19	0.172	22.13	1.64
OS -11-045	222.5	329.18	0.130	SLC	SLC
OS -11-050	137.16	257.56	0.006	29.44	0.77
OS -11-051	128.93	241.71	0.013	SLC	SLC
OS -11-054	123.44	228.6	0.543	29.67	0.96
OS -11-058	110.64	227.99	1.667	28.98	0.52
OS -11-059	54	173.74	0.116	SLC	SLC
OS -11-060	128.02	262.12	0.148	30.09	1.14
OS -11-062	113.69	231.04	1.253	23.27	0.6
OS -11-063	120.4	265.18	0.284	25.44	0.73
OS -11-066	75.28	200.25	0.017	SLC	SLC
OS -11-069	149.35	275.84	0.004	SLC	SLC
OS -11-070	173.74	292.61	0.417	20.12	1.38
OS -11-074	148.44	273.9	0.313	12.45	0.33
OS -11-076	0	60.96	0.002	SLC	SLC
OS -12-092	268.22	368.81	0.009	27.28	0.96
OS -12-093	185.35	302.06	0.010	28.7	0.89
OS -12-094	197.51	304.19	0.145	32.84	1.07
OS -12-098	163.07	219.46	0.080	SLC	SLC
OS -12-100	227.99	334.67	0.002	SLC	SLC
OS -12-102	166.42	270.05	0.003	27.58	1.9
OS -12-103	116.74	244.75	0.431	22.03	0.65
OS -12-105	167.64	275.84	0.467	SLC	SLC
OS -12-106	213.06	316.69	0.003	30.44	0.59
OS -12-108	118.26	249.33	0.703	24.5	0.68
OS -12-109	174.65	281.33	0.002	SLC	SLC
OS -12-112	209.7	343.81	0.016	27.62	0.94
OS -12-116	103.02	211.23	0.466	24.95	0.79
OS -12-117	213.66	315.97	0.303	29.05	0.68
OS -12-119	180.14	289.86	0.002	SLC	SLC
OS -12-123	86.26	183.79	0.263	29.84	0.66

Table F-1: continued.

200 – 300m Section (cont.d)

Hole Name	*To*	*From*	*Au/m*	*Average Ca*	*Average Mg*
OS -12-127	0	106.07	0.112	23.58	0.97
OS -12-128	78.64	199.03	0.309	29.14	0.66
OS -12-129	171.91	275.54	0.002	SLC	SLC
OS -12-130	20.69	130.45	0.887	32.47	0.53
OS -12-132	110.64	226.47	0.039	SLC	SLC
OS -12-134	135.03	241.71	0.012	SLC	SLC
OS -12-137	118.26	228	0.002	SLC	SLC
OS -12-138	24.38	128.02	0.163	31.55	0.71
OS -12-141	48.77	121.92	0.770	27.91	0.54
OS -12-142	30.18	75.9	0.356	31.39	0.47
OS -12-144	41.15	103.63	0.005	27.8	0.98
OS -12-145	41.15	143.26	0.232	27.31	0.71
OS -12-146	127.41	226.47	0.008	SLC	SLC
OS -12-148	163.8	272.8	0.011	25.73	1.12
OS -12-149	110.64	212.75	0.024	SLC	SLC
OS -12-152	0	106.98	0.016	SLC	SLC
OS -12-153	0	121.01	0.342	SLC	SLC
OS -12-155	130.45	243.23	0.007	20.42	1.13
OS -12-156	161.54	249.93	0.006	27.45	0.85
OS -12-157	124.36	240.18	0.002	SLC	SLC
OS -12-159	0	111.25	0.325	SLC	SLC
OS -12-161	153.03	258.22	0.059	22.76	1.49
OS -12-163	80.77	182.88	0.006	24.91	0.99
OS -12-164	145.69	267.61	0.224	29.72	0.55
OS -12-165	99.06	222.44	0.010	29.14	1.29
OS -12-168	30.48	142.64	0.778	SLC	SLC
OS -12-169	60.05	174.34	0.006	31.53	0.72
OS -12-170	118.26	227.99	0.021	SLC	SLC
OS -12-174	26.51	131.67	0.193	SLC	SLC
OS -12-175	37.49	92.66	0.376	32.02	0.43
OS -12-176	125.88	229.51	0.005	SLC	SLC
OS -12-180	29.57	131.67	0.050	29.04	1.03
OS -12-182	104.55	209.7	0.022	SLC	SLC
OS -12-183	186.64	202.08	0.002	34.02	0.55
OS -12-184	28.12	128.63	0.128	SLC	SLC
OS -12-185	154.84	261.52	0.015	SLC	SLC
OS -12-186	135.03	244.75	0.007	SLC	SLC
OS -12-187	35.97	136.25	0.013	SLC	SLC
OS -12-188	173.13	285.9	0.005	SLC	SLC
OS -12-190	222.5	362.71	0.188	23.35	0.78

Table F-1: continued.

200 – 300m Section (cont.d)

Hole Name	*To*	*From*	*Au/m*	*Average Ca*	*Average Mg*
OS -12-191	231.34	334.98	0.012	SLC	SLC
OS -12-192	265.28	374.9	0.002	7.85	1.99
OS -12-193	0	56.69	0.008	SLC	SLC
OS -12-194	249.02	346.56	0.025	SLC	SLC
OS -12-195	249.94	353.57	0.078	SLC	SLC
OS -12-196	0	27.43	0.001	SLC	SLC
OS -12-197	37.49	139.6	0.004	SLC	SLC

400m Section

Hole Name	*To*	*From*	*Au/m*	*Average Ca*	*Average Mg*
OS -10-009	96	176.48	0.395	SLC	SLC
OS -11-013	306.32	413	0.003	31.65	0.67
OS -11-030	399.29	406.91	0.003	SLC	SLC
OS -11-036	339.85	449.53	0.002	32.77	0.63
OS -11-045	329.18	353.57	0.003	SLC	SLC
OS -11-050	257.56	376.43	0.002	33.25	0.67
OS -11-051	241.71	351.43	0.571	28.09	0.46
OS -11-054	228.6	332.23	0.010	34.98	0.51
OS -11-058	227.99	340.77	0.020	28.64	0.85
OS -11-059	173.74	289.56	0.131	SLC	SLC
OS -11-060	262.12	393.19	0.008	31.43	1.21
OS -11-062	231.04	343.81	0.002	29.06	0.78
OS -11-063	265.18	411.48	0.005	27.34	0.99
OS -11-066	200.25	325.22	0.032	26.42	0.9
OS -11-069	275.84	409.36	0.049	22.43	0.92
OS -11-070	292.61	414.53	0.011	29.81	0.69
OS -11-074	273.9	400	0.221	30.37	0.51
OS -11-076	60.96	192.02	0.002	16.16	0.96
OS -12-092	368.81	469.39	0.002	29.38	0.7
OS -12-093	302.06	396.54	0.003	33.76	0.57
OS -12-094	304.19	413.92	0.004	34.11	0.43
OS -12-100	334.67	377.62	0.002	SLC	SLC
OS -12-102	270.05	370.64	0.013	31.8	0.79
OS -12-105	275.84	382.52	0.057	21.24	1.45
OS -12-106	316.69	328.88	0.003	34.73	0.51
OS -12-108	249.33	282.85	0.079	SLC	SLC
OS -12-109	281.33	388.01	0.042	33.9	0.57
OS -12-112	343.81	416.97	0.002	24.55	1.32

Table F-1: continued.

400m Section (cont.d)

Hole Name	*To*	*From*	*Au/m*	*Average Ca*	*Average Mg*
OS -12-116	211.23	317.91	1.124	23.98	0.56
OS -12-117	315.97	417.88	0.605	28.77	0.68
OS -12-119	289.86	405.69	0.029	34.39	0.5
OS -12-127	106.07	147.22	0.002	29.81	0.9
OS -12-128	199.03	253.9	0.002	32.98	0.81
OS -12-129	275.54	379.17	0.006	SLC	SLC
OS -12-130	130.45	241.71	0.302	28.78	0.67
OS -12-132	226.47	244.75	0.004	SLC	SLC
OS -12-134	241.71	348.39	0.004	SLC	SLC
OS -12-137	228	337.72	0.024	27.72	0.9
OS -12-145	143.26	245.36	0.002	30.94	0.69
OS -12-146	226.47	327.05	0.038	SLC	SLC
OS -12-148	272.8	376.43	0.006	24.06	1.25
OS -12-149	212.75	316.38	0.434	SLC	SLC
OS -12-153	121.01	236.83	0.183	28.07	0.63
OS -12-155	243.23	352.96	0.145	30.66	0.41
OS -12-157	240.18	356.01	0.031	32.66	0.41
OS -12-159	111.25	216.4	0.224	SLC	SLC
OS -12-161	258.22	359.05	0.258	30.42	0.61
OS -12-164	267.61	377.34	0.002	29.59	0.76
OS -12-168	142.64	258.47	0.154	SLC	SLC
OS -12-169	174.34	285.6	0.261	32.34	0.64
OS -12-170	227.99	337.71	0.133	SLC	SLC
OS -12-174	131.67	235.31	0.271	30.69	0.5
OS -12-176	229.51	333.15	0.025	20.81	0.43
OS -12-180	131.67	232.26	0.029	27.92	0.82
OS -12-182	209.7	313.33	0.414	SLC	SLC
OS -12-184	128.63	229.21	0.960	29.16	0.73
OS -12-185	261.52	362.1	0.007	SLC	SLC
OS -12-186	244.75	296.77	0.107	5.45	0.52
OS -12-187	136.25	236.83	0.515	SLC	SLC
OS -12-188	285.9	395.63	0.019	SLC	SLC
OS -12-190	362.71	408.43	0.042	25.37	1
OS -12-191	334.98	435.56	0.001	20.95	1
OS -12-193	56.69	192.33	0.041	SLC	SLC
OS -12-194	346.56	450.19	0.001	SLC	SLC
OS -12-195	353.57	462.49	0.002	SLC	SLC
OS -12-196	27.43	156.97	0.124	SLC	SLC
OS -12-197	139.6	243.23	0.046	SLC	SLC

Table F-1: continued.

500m Section

Hole Name	*To*	*From*	*Au/m*	*Average Ca*	*Average Mg*
OS -11-036	449.53	562.36	0.020	31.14	0.58
OS -11-050	376.43	501.4	0.554	33.23	0.65
OS -11-051	351.43	461.16	0.236	30.65	0.63
OS -11-054	332.23	435.86	0.626	28.89	0.51
OS -11-058	340.77	459.64	0.209	SLC	SLC
OS -11-059	289.56	411.48	0.014	SLC	SLC
OS -11-060	393.19	530.35	0.051	25.26	1.73
OS -11-062	343.81	427.7	0.011	28.18	1.07
OS -11-063	411.48	576.07	0.013	25.31	3.23
OS -11-066	325.22	450.19	0.631	28.16	0.59
OS -11-069	409.36	546.67	0.242	30.55	0.9
OS -11-070	414.53	545.59	0.016	30.12	1.2
OS -11-074	400	529.44	0.125	31.92	0.8
OS -11-076	192.02	324.61	0.002	16.2	1.75
OS -12-092	469.39	569.98	0.018	28.61	1.24
OS -12-094	413.92	523.65	0.003	32.52	0.62
OS -12-102	370.64	473.74	0.010	32.74	1.46
OS -12-105	382.52	406.91	0.002	25.88	1.01
OS -12-109	388.01	500.79	0.020	32.71	0.67
OS -12-116	317.91	400.2	0.459	23.24	0.82
OS -12-117	417.88	521.51	0.081	25.57	1.15
OS -12-119	405.69	521.51	0.343	31.71	0.56
OS -12-129	379.17	482.8	0.006	18.95	1.46
OS -12-130	241.71	352.96	0.334	29.38	0.56
OS -12-134	348.39	455.7	0.638	12.09	0.34
OS -12-137	337.72	447.45	0.030	30.92	0.57
OS -12-145	245.36	349	0.212	32.72	0.58
OS -12-146	327.05	430.68	0.101	SLC	SLC
OS -12-148	376.43	483.11	0.329	25.06	0.69
OS -12-149	316.38	419.35	0.522	21.1	0.63
OS -12-153	236.83	358.75	0.241	26.01	0.79
OS -12-155	352.96	464.05	0.215	28.27	1.17
OS -12-157	356.01	474.88	0.018	25.75	1
OS -12-159	216.4	323.09	0.005	29.03	0.68
OS -12-168	258.47	267.61	0.002	SLC	SLC
OS -12-169	285.6	401.42	0.412	SLC	SLC
OS -12-170	337.71	444.4	1.189	26.02	0.54
OS -12-174	235.31	261.82	0.199	24.73	0.94
OS -12-176	333.15	439.83	0.278	27.11	0.47
OS -12-180	232.26	332.84	0.007	26.31	0.97

Table F-1: continued.

500m Section (cont.d)

Hole Name	*To*	*From*	*Au/m*	*Average Ca*	*Average Mg*
OS -12-182	313.33	420.01	0.350	SLC	SLC
OS -12-184	229.21	329.79	0.180	24.57	0.86
OS -12-185	362.1	462.69	0.061	SLC	SLC
OS -12-187	236.83	337.41	0.938	28.01	0.76
OS -12-188	395.63	420.01	0.005	SLC	SLC
OS -12-191	435.56	505.66	0.001	21.02	1.31
OS -12-193	192.33	323.39	0.003	SLC	SLC
OS -12-194	450.19	492.86	0.001	SLC	SLC
OS -12-195	462.49	542.54	0.001	24.03	1.27
OS -12-196	156.97	288.04	0.041	SLC	SLC
OS -12-197	243.23	340.77	0.030	24.49	1.26

600m Section

Hole Name	*To*	*From*	*Au/m*	*Average Ca*	*Average Mg*
OS -11-036	562.36	672.08	0.252	28.36	2.06
OS -11-050	501.4	552.3	0.022	SLC	SLC
OS -11-051	461.16	567.84	0.010	29.6	0.8
OS -11-054	435.86	542.54	0.175	27.41	0.66
OS -11-059	411.48	531	0.061	SLC	SLC
OS -11-060	530.35	597.41	0.002	22.13	1.05
OS -11-063	576.07	670.56	0.002	21.7	1.33
OS -11-066	450.19	578.21	0.002	25.85	0.85
OS -11-069	546.67	653.8	0.077	22.04	0.99
OS -11-070	545.59	600.45	0.002	21.91	0.98
OS -11-074	529.44	639.17	0.011	27.55	1.19
OS -11-076	324.61	408.43	0.002	SLC	SLC
OS -12-092	569.98	670.9	0.069	31.46	0.9
OS -12-094	523.65	633.37	0.014	29.61	0.88
OS -12-102	473.74	547.42	0.002	34.73	0.75
OS -12-109	500.79	610.51	0.002	33.36	0.62
OS -12-117	521.51	625	0.051	30.66	0.84
OS -12-119	521.51	600.76	0.006	33	0.63
OS -12-129	482.8	583.39	0.007	18.02	1.22
OS -12-130	352.96	374.29	0.007	34.71	0.47
OS -12-134	455.7	538.49	0.212	26.34	0.91
OS -12-137	447.45	517.55	0.079	34.43	0.74
OS -12-145	349	409.96	0.002	33.18	0.67
OS -12-146	430.68	509.93	0.051	SLC	SLC

Table F-1: continued.

600m Section (cont.d)

Hole Name	*To*	*From*	*Au/m*	*Average Ca*	*Average Mg*
OS -12-148	483.11	589.79	0.055	25.06	1.03
OS -12-149	419.35	520.6	0.950	26.3	0.58
OS -12-153	358.75	486.77	0.003	21.38	0.92
OS -12-155	464.05	575.46	0.030	26.32	1.73
OS -12-157	474.88	593.75	0.069	31.07	1.06
OS -12-159	323.09	429.77	0.103	30.28	0.63
OS -12-169	401.42	438	0.001	SLC	SLC
OS -12-170	444.4	554.13	0.033	28.11	0.97
OS -12-176	439.83	491.64	0.066	27.49	0.69
OS -12-180	332.84	375.51	0.038	31.34	0.78
OS -12-182	420.01	526.69	0.145	32.02	0.53
OS -12-184	329.79	393.8	0.031	26.41	1.03
OS -12-185	462.69	566.32	0.110	22.72	1.13
OS -12-187	337.41	355.7	0.002	SLC	SLC
OS -12-193	323.39	451.41	0.003	31.32	0.67
OS -12-196	288.04	425.2	0.007	33.38	0.44
OS -12-197	340.77	441.35	0.014	31.07	0.7

700m Section

Hole Name	*To*	*From*	*Au/m*	*Average Ca*	*Average Mg*
OS -11-036	672.08	784.86	0.914	28.2	0.68
OS -11-054	542.54	644.9	0.031	30.52	0.77
OS -11-059	531	567.87	0.002	SLC	SLC
OS -11-066	578.21	684.89	0.019	20.122	1.74
OS -12-092	670.9	716.28	0.004	33.16	0.62
OS -12-094	633.37	660.81	0.002	32.37	0.73
OS -12-109	610.51	720.24	0.024	32.42	0.74
OS -12-117	625	728.78	0.005	24.38	1.42
OS -12-129	583.39	687.02	0.115	30.92	0.59
OS -12-148	589.79	693.42	0.172	32.78	0.59
OS -12-149	520.6	624.23	1.022	27.32	1.47
OS -12-153	486.77	517.25	0.004	22.2	1.54
OS -12-155	575.46	596.8	0.010	30.83	2.57
OS -12-157	593.75	602.89	0.002	--	--
OS -12-159	429.77	478.54	0.040	25.18	1.03
OS -12-170	554.13	611.12	0.006	26.33	1.07
OS -12-185	566.32	645.57	0.025	23.62	1.24
OS -12-193	451.41	551.99	0.001	32.31	0.7

Table F-1: continued.

700m Section

Hole Name	*To*	*From*	*Au/m*	*Average Ca*	*Average Mg*
OS -12-196	425.2	571.5	0.002	31.9	0.72
OS -12-197	441.35	541.93	0.002	33.75	0.7